

# sCO<sub>2</sub>-4-NPP: Innovative sCO<sub>2</sub>-Based Heat Removal Technology for an Increased Level of Safety of Nuclear Power Plants

## Deliverable 4.5

### Final conceptual design of the Heat Sink Exchanger

*Work programme topic addressed: NFRP-2018-10: Encouraging innovation in nuclear safety for the benefit of European citizen*

*Type of action: Innovation action*

Grant Agreement number:	847606
Start date of project: 1 September 2019	Duration: 36 months
Lead beneficiary of this deliverable:	USTUTT
Due date of deliverable: 31/08/2022	Actual submission date: 19/08/2022
	Version: R1.2

Type		
R	Document, report excluding the periodic and final reports	X
DEM	Demonstrator, pilot, prototype, plan designs	
DEC	Websites, patents filing, press & media actions, videos, etc.	
OTHER	Software, technical diagram, etc.	
Dissemination level		
PU	PUBLIC, fully open, e.g. web	X
CO	CONFIDENTIAL, restricted under conditions set out in Model Grant Agreement	

## Revision History

Release	Date	Reason for Change	Author	Distribution
R0.1	12/05/2022	First draft, sections 1, 2 and 3	K. Theologou	All partners
R0.2	30/06/2022	Second draft, section 5 (USTUTT)	K. Theologou	All partners
R0.3	08/07/2022	Third draft, section 4 (CVR)	R. Filip	All partners
R0.4	11/07/2022	Review section 4	K. Theologou	All partners
R0.5	12/07/2022	Revision section 4	R. Filip	All partners
R0.6	12/07/2022	Fourth draft, section 6 (FIVES)	S. Tioual-Demange	All partners
R0.7	12/07/2022	Review section 6	K. Theologou	All partners
R0.8	13/07/2022	Revision section 6	S. Tioual-Demange	All partners
R0.9	13/07/2022	Submission for review	K. Theologou	All partners
R1.0	14/07/2022	Internal review	Jörg Starflinger	All partners
R.1.1	14/07/2022	Revision	K. Theologou	All partners
R.1.2	19/08/2022	Final Version	K. Theologou	All partners

## Deliverable Contributors

### Authors

Partner	Name
USTUTT	Konstantinos Theologou

### Contributors

Partner	Name
CVR	Radomír Filip
FIVES	Sarah Tioual-Demange

### Internal Reviewers

Partner	Name
USTUTT	Jörg Starflinger

# Table of contents

---

1	Nomenclature and List of Acronyms.....	7
2	Executive Summary .....	10
3	Introduction .....	11
4	Proposition of the channel design for the air side of the heat sink HX .....	12
4.1	Preliminary design of the DUHS core and the fin geometry on the air side .....	12
4.2	Experimental verification .....	13
4.2.1	Experimental results.....	15
4.2.2	Heat transfer correlation.....	17
4.2.3	Fanning friction factor .....	20
4.3	Model validation.....	23
4.3.1	Model description .....	23
4.3.2	Model results.....	25
4.4	DUHS core thermal-hydraulic review .....	27
4.5	Air side channel optimization.....	28
4.5.1	Air side channel optimization results and findings.....	29
4.5.2	Air side channel optimization – multiple design points .....	32
4.6	Conclusion – Air side channel.....	33
5	Design strategy for channels and flow distribution area for the sCO <sub>2</sub> side of the heat sink HX.....	34
5.1	Expected operating conditions.....	34
5.2	Preliminary design parameter of the fin and header geometry on the sCO <sub>2</sub> site.....	34
5.3	Design strategy for channel geometry of the sCO <sub>2</sub> side.....	35
5.3.1	Evaluation and comparison of the different channels and fin geometries.....	35
5.3.2	Experimental results of the sCO <sub>2</sub> -Flex project.....	37
5.3.3	Main findings and proposition for the different channels and fin geometries.....	41
5.4	Design strategy for the flow distribution of the sCO <sub>2</sub> side .....	42
5.4.1	Literature study on different inlet plenum designs.....	42
5.4.2	Results of CFD simulation .....	44
5.4.3	Main findings and proposition for the plenum design.....	51
6	Final design and model of the heat sink HX.....	52
6.1	Improvements to the preliminary conceptual design & estimated performances.....	52
6.2	On the Air side, simulations based on the best channels design .....	52

6.3	On the sCO <sub>2</sub> side, simulations based on the best channels design and flow distribution area .....	53
6.4	Drawings .....	55
6.5	Cost Estimation .....	57
7	Conclusion .....	58
8	References .....	59

# List of Tables

Table 1: List of used instrumentation.....	13
Table 2: DUHS mockup - geometrical parameters.....	24
Table 3: Comparison of the DUHS core thermal-hydraulic performance. Datasheet vs. presented model. ....	27
Table 4: Intervals of the air channel optimization parameters.....	28
Table 5: Air channel optimization points. ....	29
Table 6: Optimized channel parameters for different flow velocities. ....	33
Table 7: Construction data of the test channels. ....	37
Table 8: Coefficient of the new correlation. ....	38
Table 9: Flow parameters and boundary conditions for the simulations.....	45
Table 10: Fins geometrical characteristics proposed for Air side optimization .....	52
Table 11: Results of the simulations “preliminary case” and “proposed fins on Air side case” .....	53
Table 12: Fins geometrical characteristics proposed for the sCO <sub>2</sub> side optimization .....	53
Table 13: Results of the simulations “preliminary case” and “serrated fins on the sCO <sub>2</sub> side case” .....	53
Table 14: Comparison between simulations of DUHS with 2 and 4 nozzles on the sCO <sub>2</sub> side.....	54
Table 15 DUHS costs details.....	57

# List of Figures

Figure 1: Scheme of DUHS core with cross-flow configuration.....	12
Figure 2.: Air channel parameters, $p = 2.54$ mm, $h = 4$ mm, $t = 0.15$ mm. ....	13
Figure 3: Fabricated DUHS mockup. ....	14
Figure 4: PID of the DUHS experimental setup. ....	14
Figure 5: Connected DUHS mockup in the sCO <sub>2</sub> loop (without thermal insulation). ....	15
Figure 6: DUHS mockup - experimental data: Mass-flow, Temperatures, Transferred heat.....	16
Figure 7: DUHS mockup experimental data - pressure drop.....	16
Figure 8: DUHS mockup experimental data - Reynolds numbers. ....	17
Figure 9: Correlation field between extrapolated and correlated Colburn factors. ....	19
Figure 10: Heat transfer coefficient as a function of Reynolds number.....	19
Figure 11: Entrance and exit friction factors as a function of contraction ratio [11].....	20
Figure 12: Fanning friction factor as a function of Reynolds number for the air side.....	21
Figure 13: Correlation field between extrapolated and correlated fanning friction factors on the air side of HX.....	21
Figure 14: Fanning friction factor as a function of Reynolds number for the CO <sub>2</sub> side. ....	22
Figure 15: Correlation field between extrapolated and correlated fanning friction factors on the CO <sub>2</sub> side of HX. ....	22
Figure 16: Discretization of DUHS mockup used in the $\varepsilon$ -NTU method.....	24
Figure 17: Flow chart of the mathematical model logic. ....	25
Figure 18: Comparison of the air outlet temperatures. Model vs. experimental data. ....	26
Figure 19: Comparison of the pressure difference on the air side. Model vs. experimental data.....	26
Figure 20: Comparison of the pressure difference on the sCO <sub>2</sub> side. Model vs. experimental data. ....	27
Figure 21: Comparison of a fin efficiency for different fin thicknesses. ....	30
Figure 22: Comparison of an effective heat transfer coefficient for different fin thicknesses. ....	30
Figure 23: Pressure drops surface contour. ....	31
Figure 24: Final weight ratio surface contour.....	31
Figure 25: Final weight ratio surface contour - top view. ....	32

<i>Figure 26: Comparison of the ventilator power requirements and necessary total heat transfer area as a function of an average air velocity.....</i>	<i>33</i>
<i>Figure 27: Side view of one core. ....</i>	<i>35</i>
<i>Figure 28: Front view of one core. ....</i>	<i>35</i>
<i>Figure 29: Different fin designs: (a) plane triangular fin; (b) plain rectangular fin or straight fin; (c) wavy fin; (d) offset strip fin or serrated fin; (e) multi louver fin; (f) perforated fin [16]......</i>	<i>36</i>
<i>Figure 30: Dimensions of the test channels [24]. ....</i>	<i>37</i>
<i>Figure 31: Plate and fin heat exchanger prototype [24]. ....</i>	<i>39</i>
<i>Figure 32: Dimensions of the prototype [24]. ....</i>	<i>39</i>
<i>Figure 33: Layer arrangement of the prototypes [24]. ....</i>	<i>39</i>
<i>Figure 34: Straight fins [24]. ....</i>	<i>39</i>
<i>Figure 35: Serrated fins [24]. ....</i>	<i>39</i>
<i>Figure 36: htc as a function of CO<sub>2</sub> mass flow [24]. ....</i>	<i>40</i>
<i>Figure 37: Colburn and Fanning factor for the investigated straight and serrated fin designs and geometries. ....</i>	<i>41</i>
<i>Figure 38: Thermo-hydraulic performance analysis of the investigated straight and serrated fin designs using the area goodness factor. ....</i>	<i>41</i>
<i>Figure 39: Initial 3D design of the manifold.....</i>	<i>44</i>
<i>Figure 40: Simulation results of the manifold – velocity profile in the channel cross-sections for the initial geometry at the design point. ....</i>	<i>46</i>
<i>Figure 41: Simulation results of the manifold – velocity vectors for the initial geometry at the design point. ....</i>	<i>47</i>
<i>Figure 42: Simulation results of the manifold – velocity pathlines for the initial geometry at the design point. ....</i>	<i>47</i>
<i>Figure 43: Mass flow distribution for the initial geometry at the design point. ....</i>	<i>48</i>
<i>Figure 44: Manifold design variation – smaller radius. ....</i>	<i>48</i>
<i>Figure 45: Manifold design variation – four inlet pipes. ....</i>	<i>48</i>
<i>Figure 46: Simulation results of the manifold – velocity pathlines for the smaller radius geometry at the design point... </i>	<i>49</i>
<i>Figure 47: Simulation results of the manifold – velocity pathlines for the four inlet pipes geometry at the design point. </i>	<i>49</i>
<i>Figure 48: Relative deviation of the mass flow rate through a channel for all geometries at the design point. ....</i>	<i>50</i>
<i>Figure 49: Relative deviation of the mass flow rate through a channel for all geometries at the transient point. ....</i>	<i>50</i>
<i>Figure 50: General assembly drawing of 1 core of the DUHS .....</i>	<i>55</i>
<i>Figure 51: Layers sketch of 1 core of the DUHS .....</i>	<i>56</i>

# 1 Nomenclature and List of Acronyms

Nomenclature	Description / meaning
$A$	total heat transfer area [m <sup>2</sup> ]
$A_f$	fins heat transfer area [m <sup>2</sup> ]
$c_p$	isobaric heat capacity [J/(kgK)]
$D_H$	hydraulic diameter [m]
$E$	relative deviation of mass flow rate [%]
$f$	fanning friction coefficient [-]
$G$	mass-flow per flow cross-section [kg/(s m <sup>2</sup> )]
$H$	channel height [m]
$h$	enthalpy [kJ/kg]
$j$	Colburn factor [-]
$k$	thermal conductivity [W/(mK)]
$K_c$	entrance friction factor [-]
$K_e$	exit friction factor [-]
$L$	effective length [m]
$\dot{m}$	mass flow rate [kg/s]
$Nu$	Nusselt number; $Nu = h \cdot D_p / k_f$ [-]
$N$	Number of channels [-]
$Re$	Reynolds number; $Re_p = v \rho D_p / \mu$ [-]
$R$	thermal resistance [W/(m <sup>2</sup> K)]
$p$	pressure [Pa]
$P$	channel pitch [m]
$Pr$	Prandtl number; $Pr = c_{p,f} \mu / k$ [-]
$Q$	transferred heat [W]
$S$	total flow distribution [-]
$T$	Temperature [°C]
$U$	over all heat transfer coefficient [W/(m <sup>2</sup> K)]
$t$	fin thickness [m]
$v$	flow velocity [m/s]
$W$	Flow heat capacity [W/K]

Greek letters	Description / meaning
$\Delta$	difference
$\varepsilon$	heat exchanger effectiveness [-]
$\eta_o$	total surface effectiveness [-]
$\eta_f$	fin efficiency [-]
$\mu$	dynamic viscosity [Pas]
$\rho$	Density [kg/m <sup>3</sup> ]
$\sigma$	contraction/expansion ratio [-]

Subscripts	Description / meaning
b	bulk
i	inlet/rows in array
m	mean value
o	outlet
s	solid
w	wall

Abbreviation / Acronym	Description / meaning
ATHLET	analysis of thermal-hydraulics of leaks and transients
CAD	computer-aided design
CFD	computational fluid dynamics
DUHS	diverse ultimate heat sink
FPM	fins per meter
htc	heat transfer coefficient [W/(m <sup>2</sup> K)]
HX	heat exchanger
LMTD	logarithmic mean temperature difference [°C]
NPP	nuclear power plant
NTU	net transfer unit
ORS	operational readiness state
PCHE	Printed Circuit Heat Exchanger
PID	Piping & Instrumentation diagram



Abbreviation / Acronym	Description / meaning
sCO <sub>2</sub>	supercritical CO <sub>2</sub>

## 2 Executive Summary

---

The goal of the sCO<sub>2</sub>-4-NPP project is to develop a robust heat removal system for a nuclear power plant with technology readiness level (TRL) 5, based on the results of the sCO<sub>2</sub>-HeRo project, in which a down-scaled heat removal system with TRL 3-4 was developed, built and tested. This deliverable (D4.5) relates to work package 4 (WP4) focusing on the conceptual design of the components (turbomachinery and heat exchanger) especially Task 4.4 which concerns the optimization of the diverse ultimate heat sink exchanger (DUHS). Task 4.4 is divided into three parts, each being addressed to one project partner. Based on an initial design of the DUHS, CVR is responsible for the investigation and optimization of the air side and USTUTT for the sCO<sub>2</sub> side. Based on these proposals, FIVES will present a final DUHS design including cost calculation.

An activity of CVR was focused on both experimental and analytical studies of the performance of the DUHS between sCO<sub>2</sub> and ambient air. The analytical studies were focused mainly on the air side, respectively on the optimization of the air channel geometry. For this purpose, an extensive experimental study was carried out through testing of a DUHS mock-up delivered by FIVES in the large-scale sCO<sub>2</sub> loop of CVR. Implementation of the testing mockup in the sCO<sub>2</sub> loop ensures testing at relevant parameters. The experimental data are used for verification of the design of the mockup at relevant conditions and validation of the numerical tools. The validated numerical models might be then used for designing the large-scale DUHS units.

USTUTT has investigated the sCO<sub>2</sub> side from two aspects, the fin geometry and the flow distribution area. First, a literature study was conducted to find out if there are ways to improve the design of the fins. Furthermore, two heat exchanger prototypes from FIVES from the sCO<sub>2</sub>-FLEX project [1] were evaluated in a performance study. In a direct comparison of the heat exchanger prototypes, the serrated fin performs better in terms of heat transfer efficiency and the straight fin performs better in terms of pressure drop. In the overall consideration using the area goodness factor, the straight fin design shows better results. Furthermore, the flow distribution area at the inlet of the heat exchanger was investigated. For this purpose, design optimization of the inlet plenum was carried out, using ANSYS FLUENT. Based on a literature study and the initial design, three different geometries of the inlet plenum were constructed and simulated at the design point mass flow rate and another reduced mass flow rate to consider a transient point. It has been shown that increasing the number of inlet pipes of the plenum from two to four for both mass flow rates leads to a more uniform flow distribution.

The final design of the DUHS was established regarding the results of the optimization work on both the sCO<sub>2</sub> and the air side. A compromise needed to be achieved to take into account not only the thermal and hydraulic optimization part, but also the mechanical resistance of the device according to what is expected by the regulation, the manufacturability and the cost reduction optics. The corresponding drawings and the detailed costs are included.

In conclusion, the deliverable describes the successful optimization process and the final design of the DUHS for Task 4.4 and thus completely fulfils the objective of the project.

### 3 Introduction

---

The overall aim of the sCO<sub>2</sub>-4-NPP project is to bring the technology of a sCO<sub>2</sub>-based heat removal system for Nuclear Power Plants (NPP) closer to the market. The project is based on the findings of the sCO<sub>2</sub>-HeRo project [1] in which a small-scale demonstration unit of the system was built and implemented in a cycle of a boiling water reactor glass model [2]. To successfully achieve the project aim, the project was subdivided into seven objectives. The content of this work is classified under Objective 4, which is the design of components for the sCO<sub>2</sub>-4-NPP loop in the context of licensing requirements (turbomachinery, heat exchanger, auxiliary systems) with the outcome being CAD designs of components that comply with nuclear licensing requirements available and documented key performance data (dimensions, masses, efficiencies, etc.).

The content of this deliverable (D4.5) relates to work package 4 (WP4) focusing on the conceptual design of the components (turbomachinery and heat exchanger) especially Task 4.4 which concerns the optimization of the DUHS. The responsible project partners for Task 4.4 are USTUTT, CVR and FIVES. This task aims to propose an optimized design of the DUHS, based on FIVES's preliminary design in D4.4 [3], to have a significant reduction of the built area and also to increase the overall performance of the sCO<sub>2</sub>-4-NPP cycle. For this, two key points need to be developed. On the one hand, the definition of the best channel design on the air side to achieve high heat transfer rates with low pressure drop at the same time. On the other hand, a design strategy for sCO<sub>2</sub>'s channels and flow distribution area will be developed for a wide range of operating conditions. Finally, an improved design of the DUHS is to be achieved including estimated performances, drawing, cost and model.

In D4.4 [3] FIVES presents the preliminary design of the DUHS based on brazed plates and fins heat exchanger technology. The advantages of this technology are an important heat exchange capability with low pinch and high available flow sections. It also allows meeting the desired thermal duty with low pressure drop leading to a reduction in size and capital cost. By changing the thermodynamic design input parameters (essentially by increasing the mass flow rate), the temperature difference between the air and the sCO<sub>2</sub> side could be reduced to <100 °C. This enables a design solution with 316-grade stainless steel, which is compatible with the regulations for NPP. The design leads to 20 counter-flow heat exchanger cores for each unit (six units for the entire sCO<sub>2</sub>-heat removal system) with the dimensions of 2000 mmx987 mmx570 mm (WxHxL) per core. Each core consists of 196 layers, 64 for the sCO<sub>2</sub> side, 128 for the air side (double-banking, due to the low heat transfer rate of the air side) and 4 dummy layers.

As part of D4.4, multiple one-dimensional simulations of the whole sCO<sub>2</sub> heat removal system in ATHLET were carried out for various conditions [3]. Thereby the design point for the DUHS for the sCO<sub>2</sub> side was defined at a pressure of 12.70 MPa, an inlet temperature of 243.19 °C and a mass flow rate of 29.74 kg/s [3].

Based on the preliminary design of the DUHS and the simulations, this deliverable carries out optimisation studies and finalises the DUHS design.

## 4 Proposition of the channel design for the air side of the heat sink HX

### 4.1 Preliminary design of the DUHS core and the fin geometry on the air side

As part of the D4.4, FIVES developed a preliminary design for the DUHS. It accounts for 6 units, where one unit should reject  $\approx 10$  MW of heat. Each unit is consisting of 20 heat exchanger cores. The DUHS core is a brazed fin&plate type heat exchanger with a cross-flow configuration (schematically shown in Figure 1) with dimensions of 2 m in width, 0.64 m in length and 0.987 m in height and it has a total number of 196 layers per core. Thereby, two air layers are stacked against one CO<sub>2</sub> layer. This stacking pattern is called “double-banking” and results in 64 layers of CO<sub>2</sub> and 128 layers of air [4]. The purpose of the remaining 4 layers is to guarantee the mechanical integrity of the cores. The parting sheets between the layers are 1 mm thick. Each layer contains channels with plain straight fins. The preliminary air channel geometry proposed by FIVES has a fin thickness of 0.15 mm, 393.7 fins per meter and a channel height of 4 mm (shown in Figure 2). This geometry forms the initial geometry for the optimisation process and is used also for experimental verification.

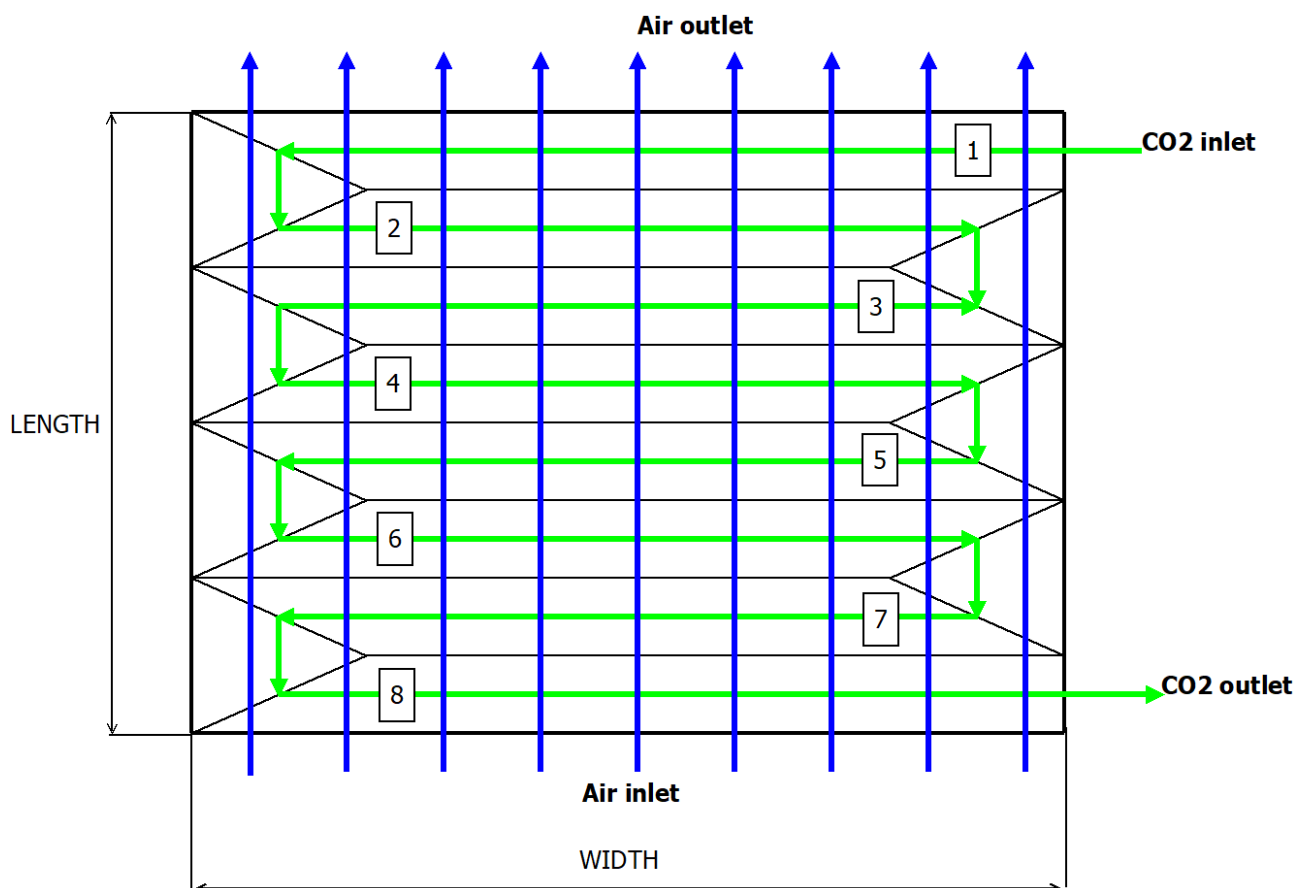


Figure 1: Scheme of DUHS core with cross-flow configuration.

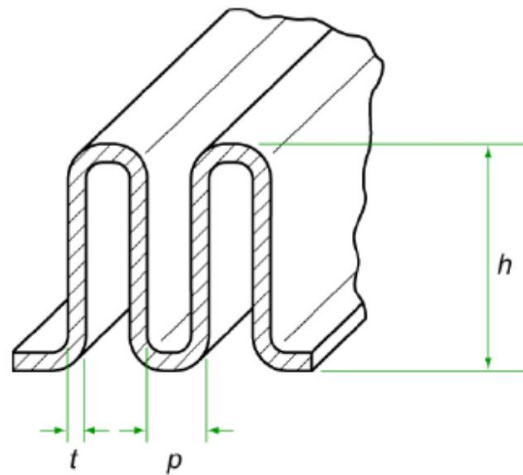


Figure 2: Air channel parameters,  $p=2.54$  mm,  $h=4$  mm,  $t=0.15$  mm.

## 4.2 Experimental verification

In order to verify the thermal-hydraulic design and validate the numerical codes, a small DUHS mockup was fabricated by FIVES. The DUHS mockup (shown in Figure 3) keeps the same channel geometry as mentioned in section 4.1 for the air side and 5.2 for the CO<sub>2</sub> side. It has 305 mm in width, 224 mm in length and 52 mm in height and consists of 3 layers per CO<sub>2</sub> side and 6 layers per air side [5]. The heat exchanger testing took place at Research Centre Rez (CVR) using the sCO<sub>2</sub> experimental loop, which was constructed within SUSEN (Sustainable Energy) project [6]. The sCO<sub>2</sub> loop is a large-scale experimental facility in the form of a simple Brayton cycle with a heating power of 110 kW, sCO<sub>2</sub> temperatures up to 550 °C, pressure 25 MPa and mass-flow rate up to 0.3 kg/s. The facility has been used within various R&D projects focused on the development of sCO<sub>2</sub> cycles and components testing. The DUHS mockup was delivered by FIVES to CVR and was implemented in the low pressure part of the sCO<sub>2</sub> loop which corresponds to an appropriate location in the real sCO<sub>2</sub> cycles.

For the experiments, the DUHS mockup's air side was equipped with flange ducts from both sides, connected to the blower on the inlet side. The sCO<sub>2</sub> side was connected to the low pressure section of the super critical CO<sub>2</sub> experimental loop, which was operated at 8 MPa and temperatures in the range of <100 °C-172 °C> to ensure the CO<sub>2</sub> is above its critical point. The experimental PID layout is schematically shown in Figure 4. The installed instrumentation with its measurement error is listed in Table 1. Figure 5 shows a connection of the DUHS mockup in the sCO<sub>2</sub> loop. The whole setup was wrapped in thermal insulation.

Table 1: List of used instrumentation.

Variable	Description	Range	Units	Measurement error
<b>T1,2,3</b>	K-type Thermocouple class 1	0-300	°C	±1.5 °C
<b>T4,5,6,7,8,9,10,11</b>	Pt100 class A	0-300	°C	±0.35 °C
<b>F1</b>	Thermic flow sensor	0-465	m <sup>3</sup> /h	±5% of measured value
<b>F2</b>	Coriolis flow meter	0-0.7	kg/s	±10% of measured value
<b>PD1</b>	Pressure difference transducer	0-15	mbar	±0.1 mbar
<b>PD2</b>	Pressure difference transducer	0-500	mbar	±0.4 mbar
<b>P</b>	Absolute pressure transducer	0-400	bar	±0.3 bar



Figure 3: Fabricated DUHS mockup.

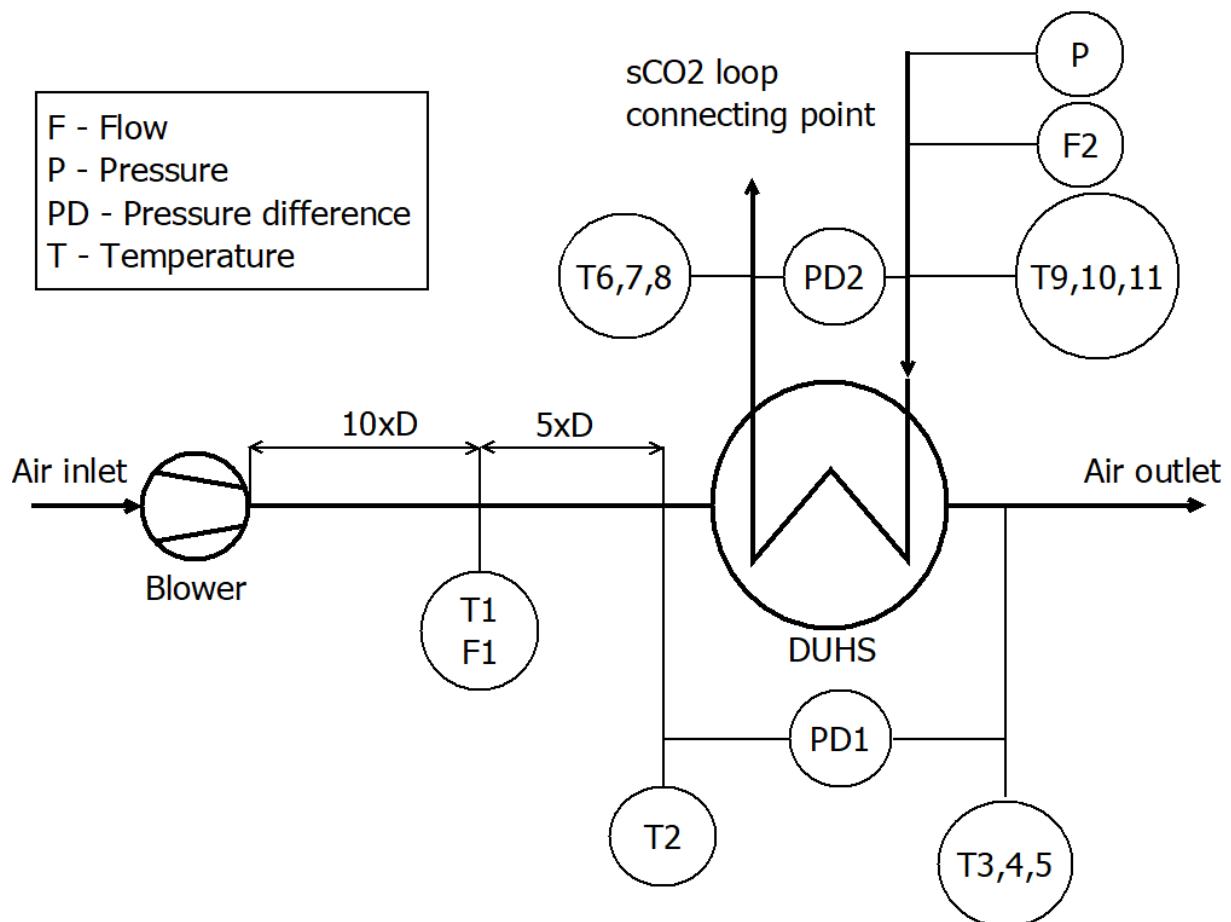


Figure 4: PID of the DUHS experimental setup.





**Figure 5: Connected DUHS mockup in the sCO<sub>2</sub> loop (without thermal insulation).**

#### 4.2.1 Experimental results

During the experimental campaign, the CO<sub>2</sub> mass flow and inlet temperature were kept constant at 6 different levels, while air mass flow varied upon reaching a steady state. Hence in total 30 steady-state data points were measured. Total heat transfer was obtained by averaging values of heat transfer contribution from each medium calculated from the calorimetric equation. The resulting values of measured mass-flow, temperatures and transferred heat for each state are shown in Figure 6, where a maximum heat transfer of 7800 W was reached. The measured pressure drops for each side are shown in Figure 7. Furthermore, Reynolds numbers based on the channel's hydraulic diameter were calculated and are shown in Figure 8. The Reynolds number on the air side is within range <150; 3700> and on the sCO<sub>2</sub> side <11000; 23000>. The operating point of the DUHS core is expected to lie within these ranges of Reynolds numbers, hence the measured data can be used to correlate the coefficients for heat transfer and pressure drop.

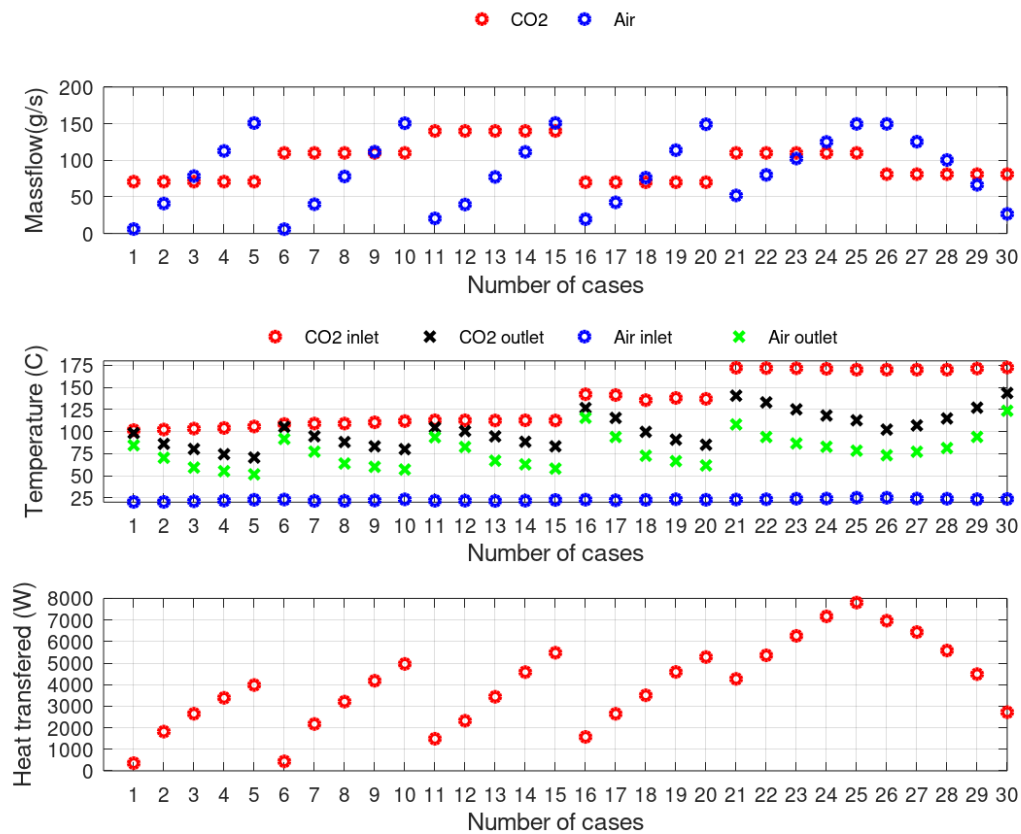


Figure 6: DUHS mockup - experimental data: Mass-flow, Temperatures, Transferred heat.

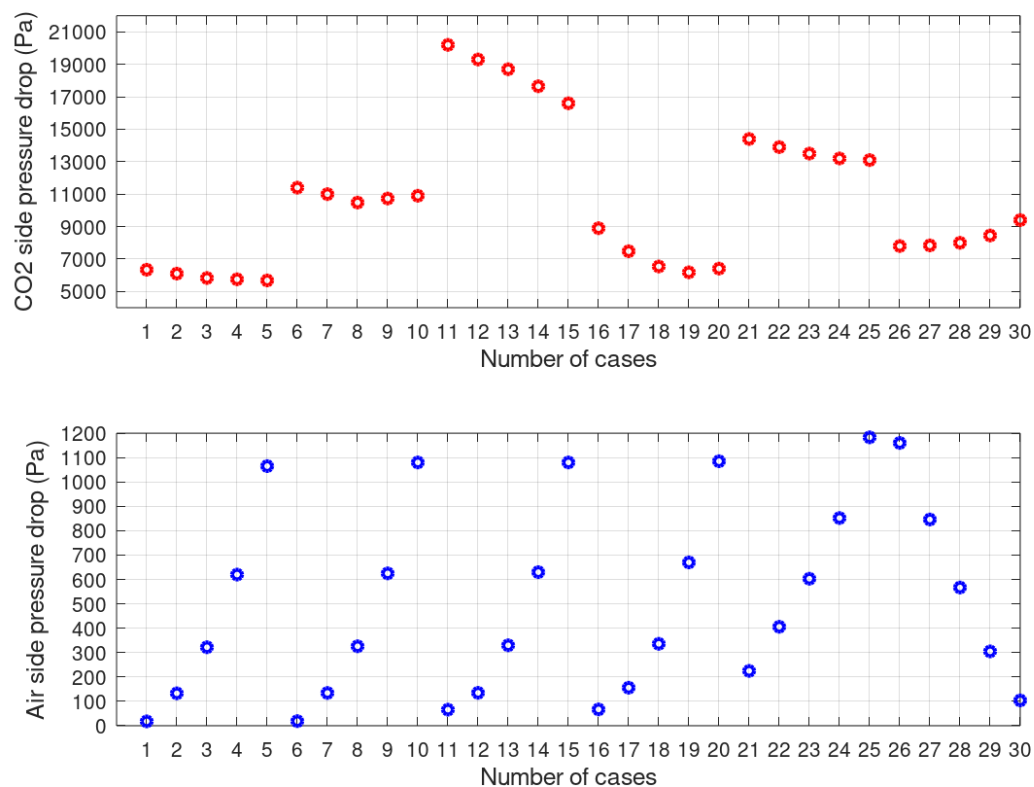


Figure 7: DUHS mockup experimental data - pressure drop.



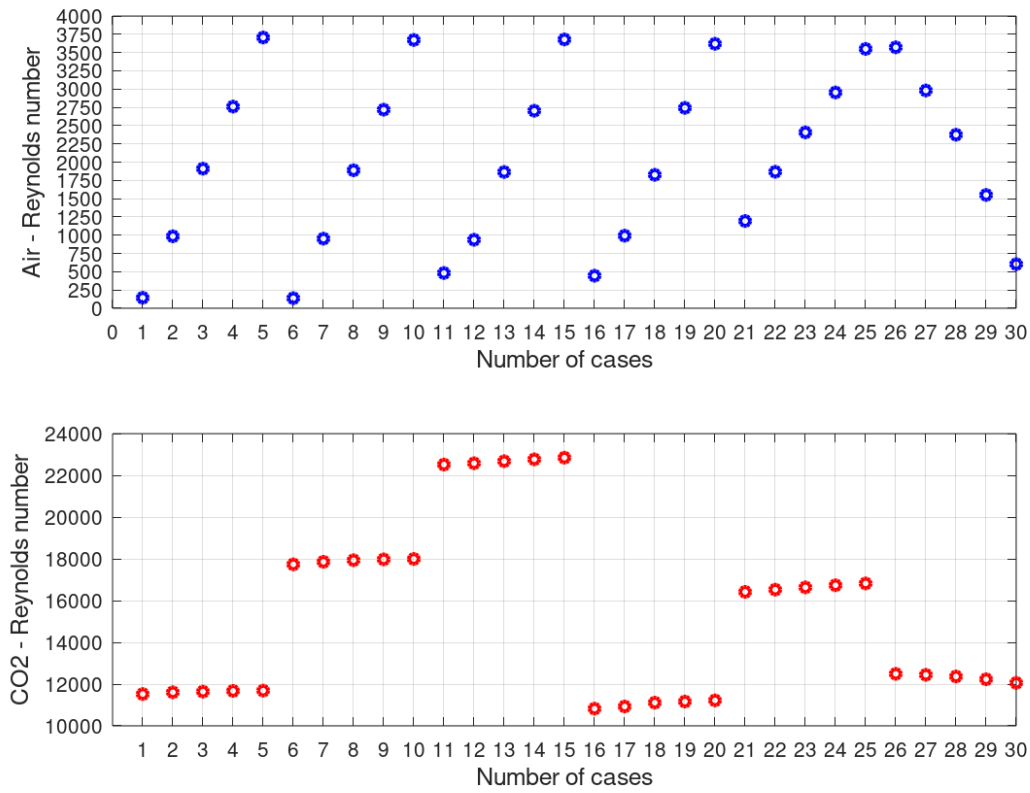


Figure 8: DUHS mockup experimental data - Reynolds numbers.

#### 4.2.2 Heat transfer correlation

To extrapolate the heat transfer coefficient from the experimental data, the Wilson plot method was employed [7]. The overall heat transfer coefficient  $U$  can be expressed as:

$$\frac{1}{UA} = \frac{LMTD}{Q} = \frac{1}{(\eta_0 htc A)_{Air}} + \frac{t}{(kA)_{Wall}} + \frac{1}{(\eta_0 htc A)_{CO2}} = \frac{1}{(\eta_0 htc A)_{Air}} + C_1 \quad (4-1)$$

Where constant  $C_1$  is a sum of thermal resistances given as:

$$C_1 = R_{Wall} + R_{CO2} = \frac{t}{(kA)_{Wall}} + \frac{1}{(\eta_0 htc A)_{CO2}} \quad (4-2)$$

The heat transfer coefficient on the air side can be generally expressed as follows:

$$htc_{air} = C Re^m Pr^{1/3} \left( \frac{k_{air}}{D_h} \right) \quad (4-3)$$

Substituting Eq. ( 4-3 ) into Eq. ( 4-1 ) gives:

$$\frac{1}{UA} = \frac{1}{C Pr^{1/3} \left( \frac{k_{air}}{D_h} \right) A \eta_0} \frac{1}{Re^m} + C_1 = C_2 \frac{1}{Re^m} + C_1 \quad (4-4)$$

Assuming the sum of the thermal resistances  $R_{wall}$  and  $R_{CO2}$  is an order of magnitude smaller than the resulting thermal resistance on the air side of the heat exchanger. The overall heat transfer coefficient will be mainly affected by the heat transfer coefficient on the air side. Therefore, to determine the heat transfer coefficient

on the sCO<sub>2</sub> side, some general htc correlation for forced convection can be used, for this purpose, the Gnielinsky correlation is used validly in the range  $10^4 < Re < 10^6$  [8; 9] it goes as:

$$htc = \frac{(\xi/8)RePr}{1 + 12.7\sqrt{(\xi/8)(Pr^{2/3} - 1)}} \cdot \left[ 1 + \left( \frac{D_h}{L} \right)^{2/3} \right] \left( \frac{k}{D_h} \right) \quad (4-5)$$

Where  $\xi$  goes as:

$$\xi = (1.8 \log_{10} Re - 1.5)^{-2} \quad (4-6)$$

Since the heat exchanger concept contains fins, the total heat transfer rate is evaluated through a concept of total surface effectiveness  $\eta_0$  defined as:

$$\eta_0 = 1 - \left( 1 - \eta_f \right) \frac{A_f}{A} \quad (4-7)$$

Where  $A_f$  is the fin surface area and  $A$  is the total surface area, the  $\eta_f$  is the fin efficiency defined as:

$$\eta_f = \frac{\tanh(h'X)}{h'X} \quad (4-8)$$

Where  $X$  is defined as:

$$X = \sqrt{\frac{2 htc}{k t}} \quad (4-9)$$

The value of  $h'$  term for the “double-banking” pattern will differ for the air and CO<sub>2</sub> channel. In the case of the air channel the  $h' = h - t$ , but in the case of the CO<sub>2</sub> channel, the adiabatic plane is in the middle of the channel, thus  $h' = h/2 - t$ .

The fin surface area  $A_f$  is considered as:

$$A_f = 2(H - t) \cdot L \cdot N \quad (4-10)$$

Where  $N$  is the number of channels and  $L$  is their effective length. The total area is considered as:

$$A = 2(P - t) \cdot L \cdot N + A_f \quad (4-11)$$

Finally, coefficient  $C_1$  in Eq. ( 4-2 ) can be analytically calculated and coefficients  $C_0$  and  $m$  were obtained with the least square linear regression method, each for the constant condition on the CO<sub>2</sub> side. Now the heat transfer coefficient on the air side can be expressed from the following equation:

$$R_{air} = \frac{1}{(\eta_0 htc A)_{Air}} = C_2 \frac{1}{Re^m} \quad (4-12)$$

The obtained heat transfer coefficients on the air side were used to calculate the Colburn factor defined as:

$$j = \frac{htc}{\rho \bar{u} c_p} Pr^{2/3} \quad (4-13)$$

The Colburn factor was correlated as a function of Reynolds number, using the least square linear regression method. The following function was found to match best the extrapolated data:

$$j = 0.026 Re^{-0.31} + \frac{0.2}{Re} \quad (4-14)$$

The Colburn factor correlation from Eq. ( 4-14 ) is valid for straight fins in the range of Reynolds numbers  $<200-4000>$ . The comparison of the correlation and extrapolated data is shown in Figure 9, where is visible that the

correlation matches the extrapolated data with an average absolute deviation of 9.7 % and maximum error of nearly  $\pm 30$  %. The increased error is caused by the fact that the correlation is applicable from laminar over to the fully turbulent region and thus is more robust. Figure 10 is shown the extrapolated and correlated values of heat transfer coefficients as a function of the Reynolds number.

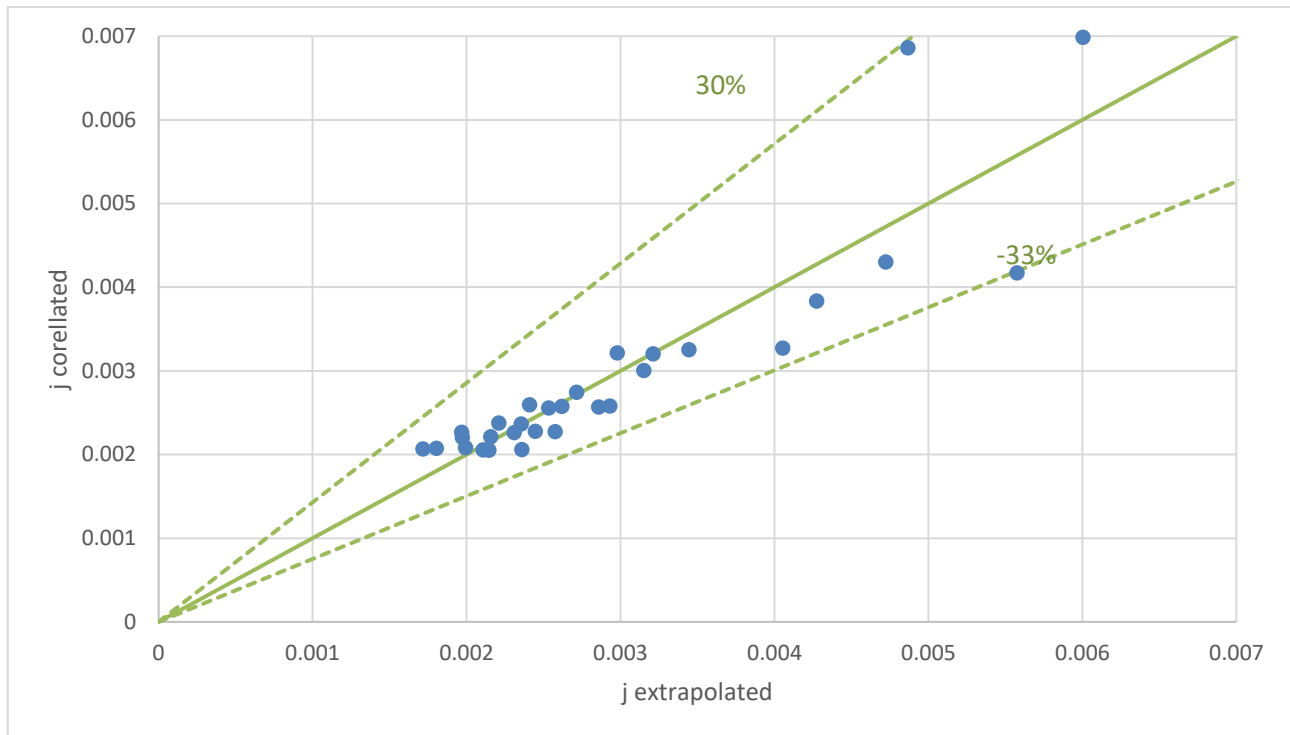


Figure 9: Correlation field between extrapolated and correlated Colburn factors.

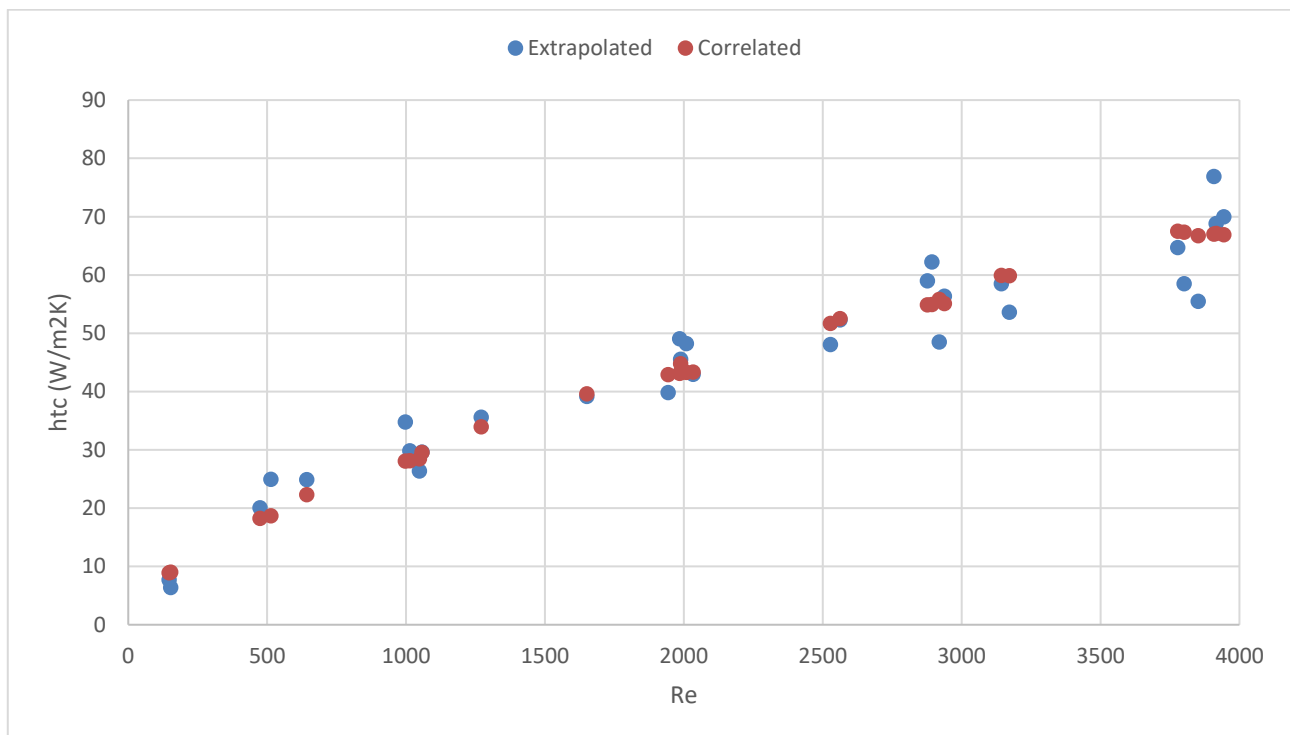


Figure 10: Heat transfer coefficient as a function of Reynolds number.

### 4.2.3 Fanning friction factor

The Fanning friction factor can be determined from the experimental data with the following equation [10].

$$f = \frac{D_h}{2L} \frac{1}{(1/\rho)_m} \left[ \frac{2\Delta p}{G^2} - \frac{1}{\rho_i} (1 - \sigma^2 + K_c) - 2 \left( \frac{1}{\rho_o} - \frac{1}{\rho_i} \right) + \frac{1}{\rho_o} (1 - \sigma^2 + K_e) \right] \quad (4-15)$$

Where  $\sigma$  is the contraction/expansion ratio, which is the ratio of the total front flow area over the total front area at the entrance/exit.  $K_c$  and  $K_e$  are entrance/exit friction factors that were determined from the graph shown in Figure 11 [11]. The Fanning friction factor was calculated according to Eq. ( 4-15 ) and correlated using the least square linear regression method for the air and CO<sub>2</sub> sides. The resulting correlation for the Fanning friction factor on the air side goes as:

For laminar region  $Re < 2000$ :

$$f = \frac{18.3}{Re} \quad (4-16)$$

For turbulent region  $2000 < Re < 4000$ :

$$f = 0.017 Re^{-0.07} \quad (4-17)$$

The comparison between extrapolated and correlated friction factors is shown in Figure 12. The correlation field is shown in Figure 13, where the average absolute deviation between extrapolated and correlated data is 5.3 % and the maximum error is within the range of  $\pm 15$  %.

The resulting correlation for the Fanning friction factor on the sCO<sub>2</sub> side goes as:

$$f = 3.5 Re^{-0.56} \quad (4-18)$$

Valid in range of Reynold number  $<10\,000; 25\,000>$ . The comparison between extrapolated and correlated friction factors is shown in Figure 14. The correlation field is shown in Figure 15, where the average absolute deviation between extrapolated and correlated data is 7.4 % and the maximum error is within the range of nearly  $\pm 20$  %.

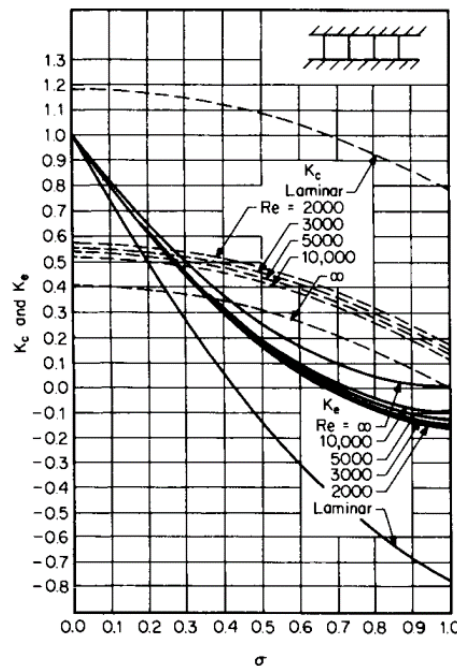


Figure 11: Entrance and exit friction factors as a function of contraction ratio [11].

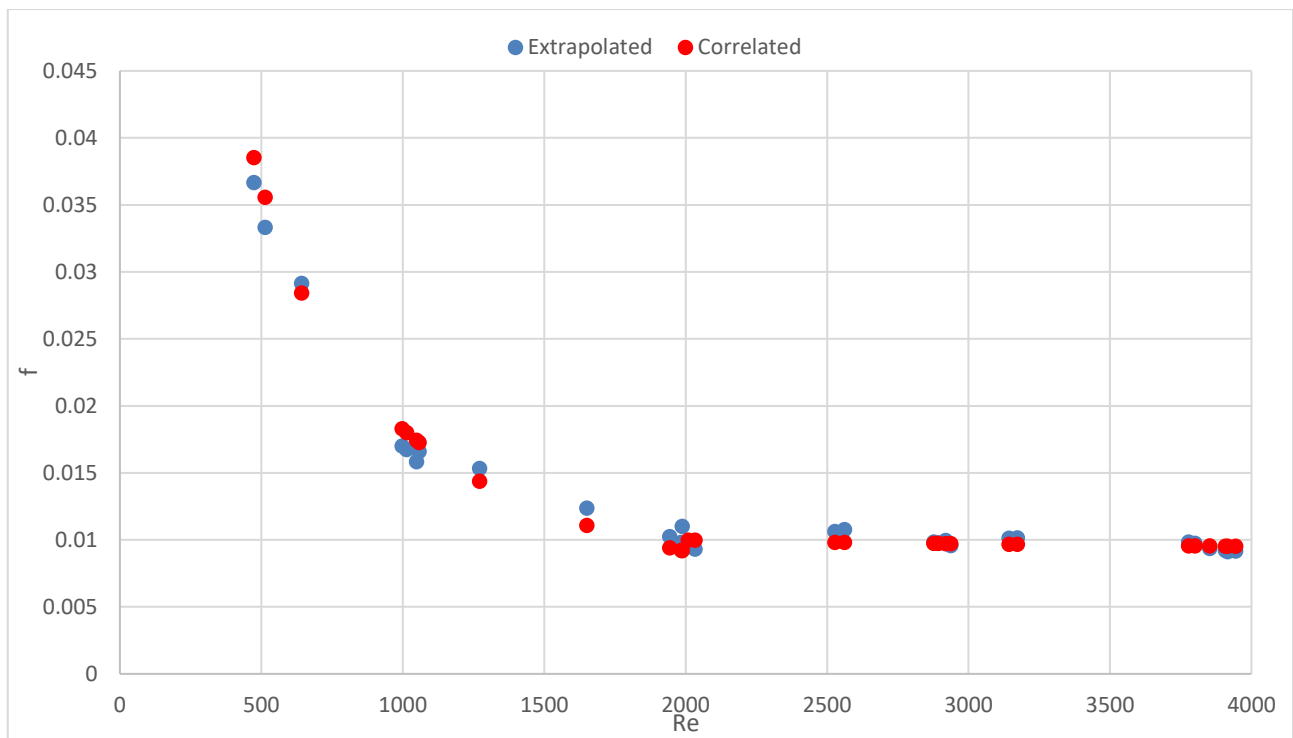


Figure 12: Fanning friction factor as a function of Reynolds number for the air side.

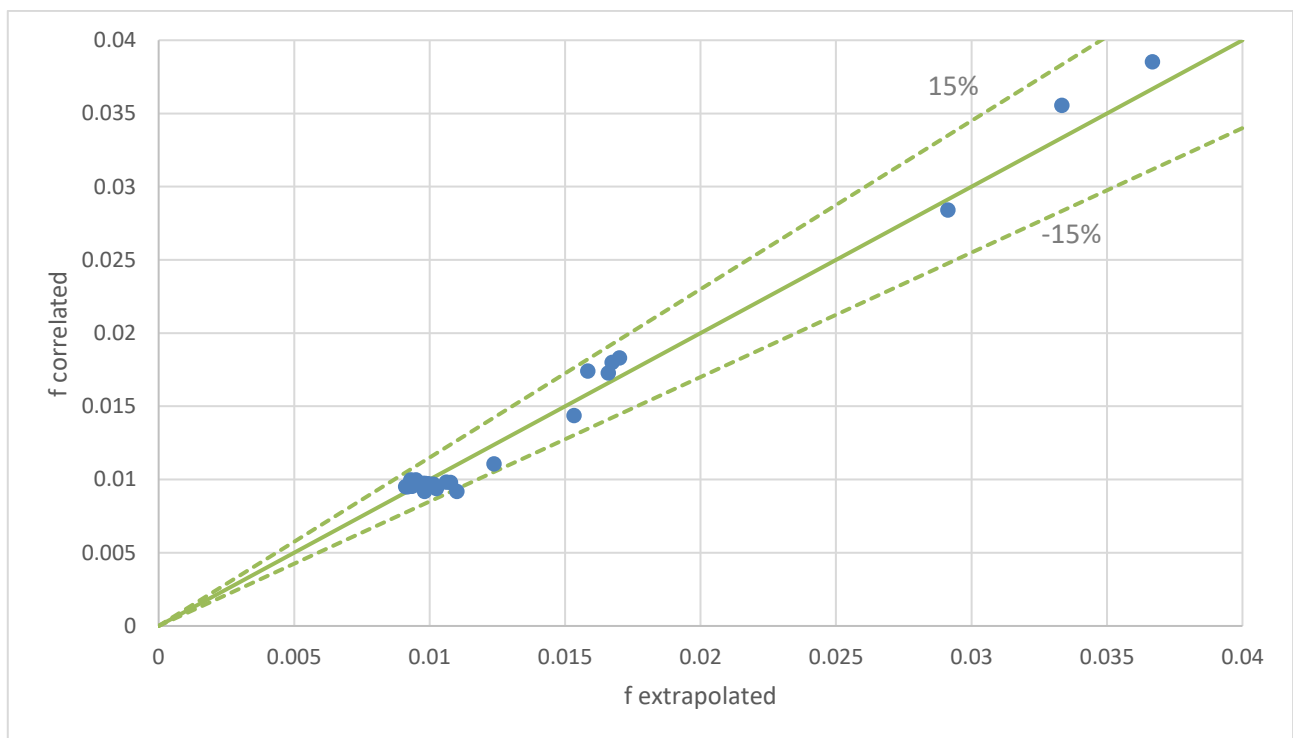


Figure 13: Correlation field between extrapolated and correlated fanning friction factors on the air side of HX.

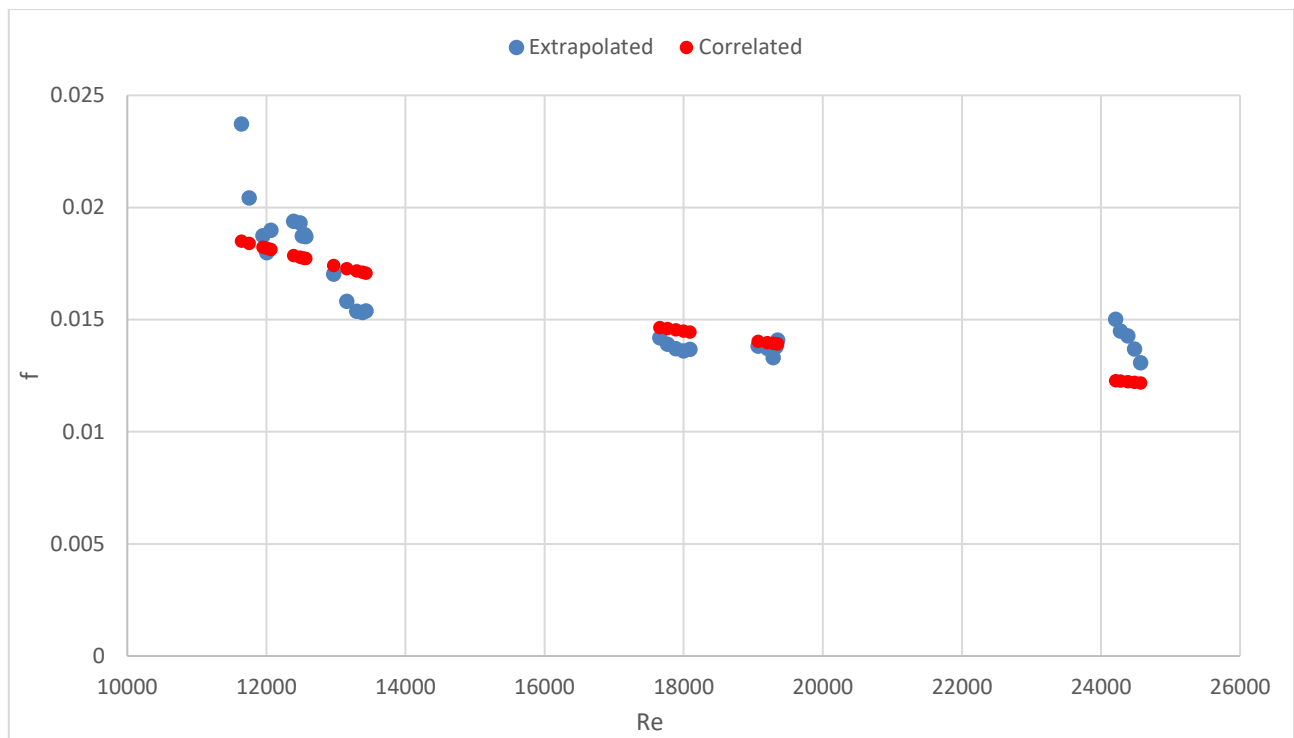


Figure 14: Fanning friction factor as a function of Reynolds number for the CO<sub>2</sub> side.

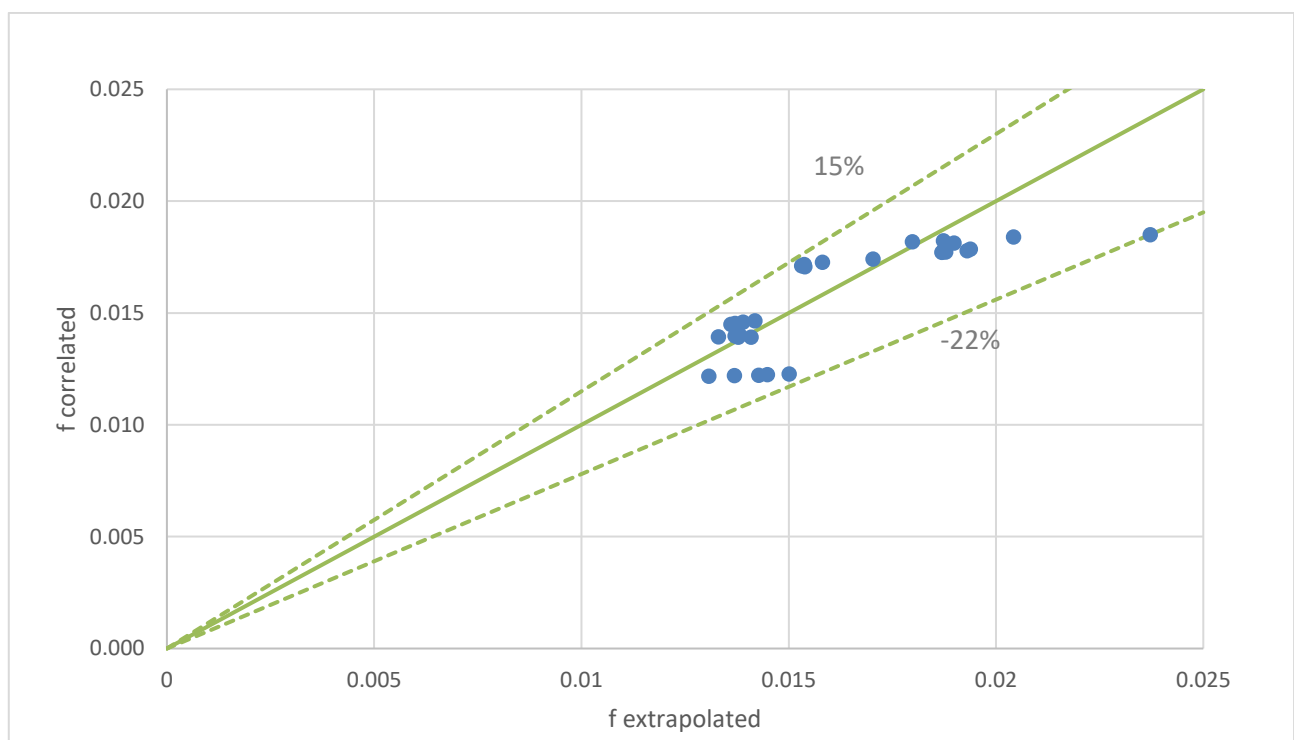


Figure 15: Correlation field between extrapolated and correlated fanning friction factors on the CO<sub>2</sub> side of HX.

## 4.3 Model validation

### 4.3.1 Model description

To test the thermal-hydraulic performance of the preliminary design and potentially design of different channel geometries of the DUHS, a 1D mathematical model was developed and validated with the experimental results. To calculate the heat transfer an  $\varepsilon$ -NTU method was employed [11]. The heat exchanger was discretized into smaller net transfer units, where the number of rows corresponds to index  $i$ , which is equal to the number of sCO<sub>2</sub> passages and then index  $j$  corresponds to the number of columns (shown in Figure 16). In this case, the flow arrangement can be considered as unmixed crossflow, where the heat exchanger effectiveness is given by the expression:

$$\varepsilon = 1 - \exp((\exp(-NTU^{0.78}W^*) - 1)NTU^{0.22}/W^*) \quad (4-19)$$

Where  $NTU$  and  $W^*$  are given as follows:

$$NTU = \frac{UA_{i,j}}{W_{min}} \quad (4-20)$$

$$W^* = \frac{W_{min}}{W_{max}} \quad (4-21)$$

Where  $W$  is a flowing heat capacity rate with units (W/K). With the current arrangement, the minimal flow heat capacity will be always at the air side, thus following expressions for the inlet/outlet NTU temperatures in the first row are valid:

$$T_{air(i+1,j)} = T_{air(i,j)} + \varepsilon_{(i,j)} \cdot (T_{CO2(i,j)} - T_{air(i,j)}) \quad (4-22)$$

$$T_{CO2(i,j+1)} = T_{CO2(i,j)} + W^* \cdot (T_{air(i+1,j)} - T_{air(i,j)}) \quad (4-23)$$

The temperatures are iteratively calculated in this manner until certain accuracy is reached. The 1D mathematical algorithm is presented in the flow chart shown in Figure 17. The thermo-physical properties of each medium are exported from the NIST database [12] and are considered at the average inlet/outlet temperature of each NTU at constant operating pressure.

The mass-flows and flow heat capacities for each medium are calculated with the Enthalpy  $h$  as:

$$\dot{m}_i = \frac{\dot{Q}}{\Delta h_i} \quad (4-24)$$

$$W_i = \frac{\dot{Q}}{\Delta T_i} \quad (4-25)$$

The DUHS geometrical parameters are listed in Table 2 [5], then the channel's *Flow area*, the hydraulic diameter  $D_h$  and a total number of channels  $N$  are calculated as:

$$Flow\ area_i = (P_i - t_i)(H_i - t_i) \quad (4-26)$$

$$D_{hi} = 4 \cdot Flow\ area / (2((P_i - t_i) + (H_i - t_i))) \quad (4-27)$$

$$N_i = (FPM_i \cdot Effective\ width + 1) \cdot number\ of\ layers \quad (4-28)$$

The channel velocities and Reynolds numbers are calculated as:

$$v_i = \frac{\dot{m}_i}{Flow\ area_i \rho_i N_i} \quad (4-29)$$

$$Re_i = \frac{v_i D_{hi} \rho_i}{\mu_i} \quad (4-30)$$

As for the heat transfer coefficients and the overall heat transfer coefficient, it proceeds in the same way as it is mentioned in section 4.2.2, where the new heat transfer correlation was utilized. As for the hydraulic calculation, Eq. ( 4-15 ) can be rewritten into the following form to obtain a formula for the pressure drop:

$$\Delta p = \frac{G^2}{2} \frac{1}{\rho_i} \left[ (1 - \sigma^2 + K_c) + f \frac{2L}{D_h} \rho_i \left( \frac{1}{\rho} \right)_m + 2 \left( \frac{\rho_i}{\rho_o} - 1 \right) - \frac{\rho_i}{\rho_o} (1 - \sigma^2 + K_e) \right] \quad (4-31)$$

During the pressure drop calculations, the correlated fanning friction factors from section 4.2.3 were utilized.

Table 2: DUHS mockup - geometrical parameters.

	Air	sCO <sub>2</sub>
FPM	388.2	787.4
P (mm)	2.576	1.27
H (mm)	4	4
t (mm)	0.2	0.3
number of layers	6	3
Effective width (mm)	281	50
Effective length (mm)	214	1220

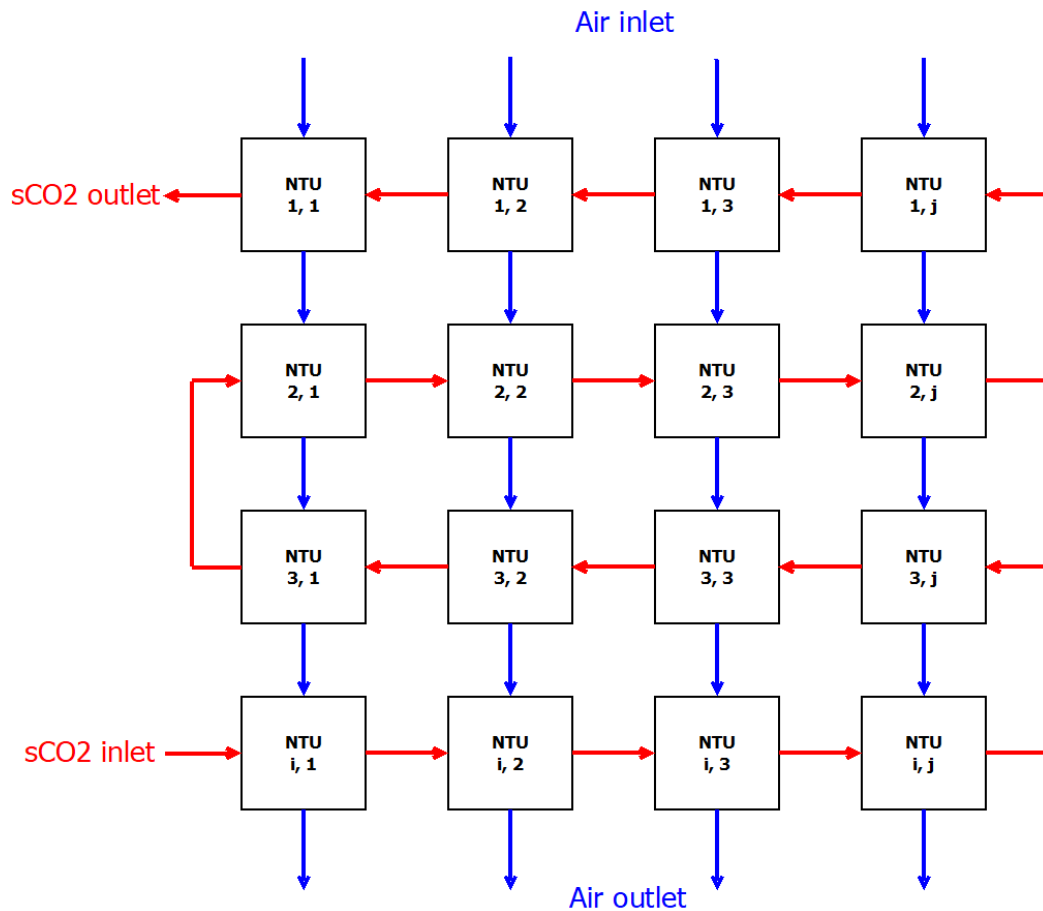


Figure 16: Discretization of DUHS mockup used in the  $\varepsilon$ -NTU method.



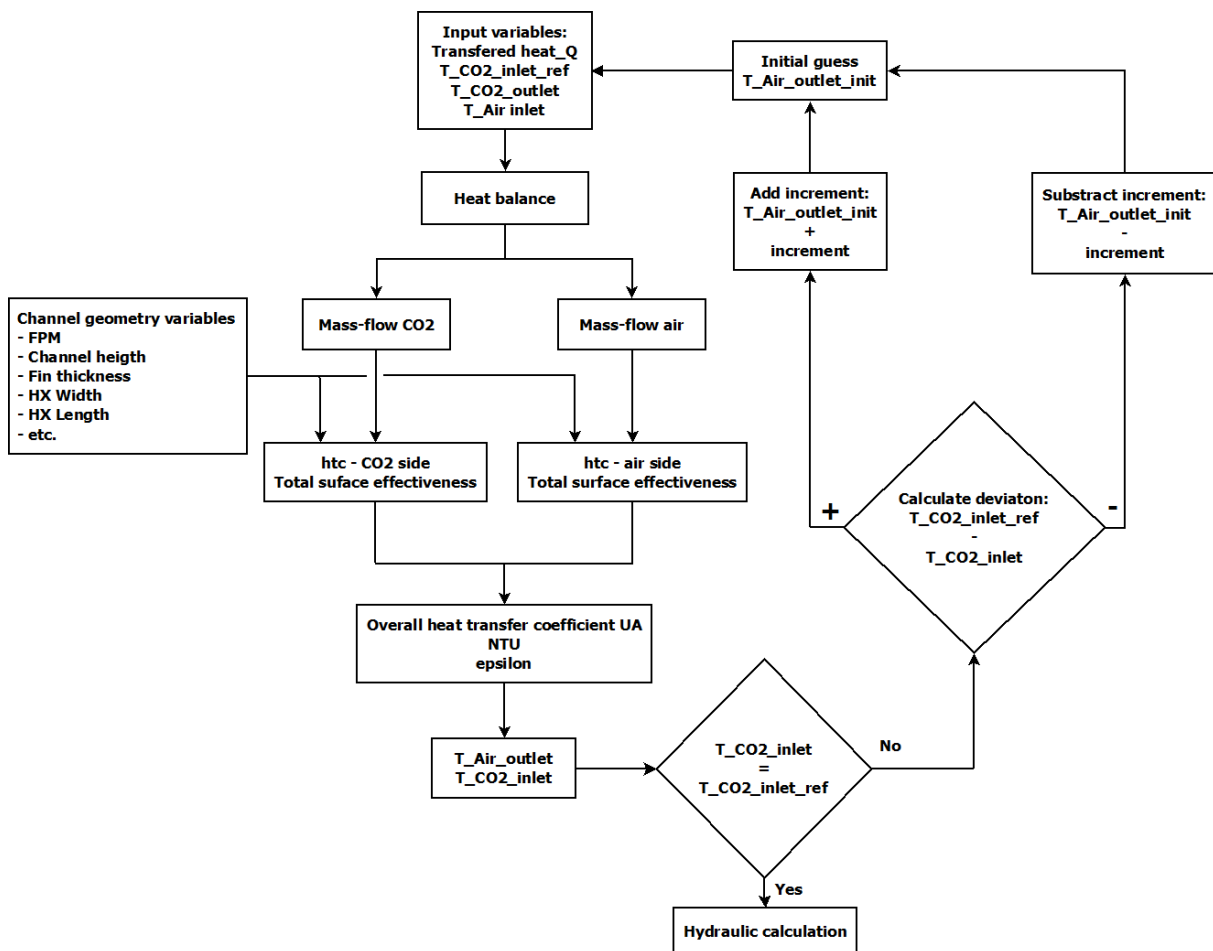


Figure 17: Flow chart of the mathematical model logic.

#### 4.3.2 Model results

To validate the numerical 1D model described in section 4.3.1, the model was fed with data obtained from the experiment, presented in section 4.2.1, namely transferred heat, input/output CO<sub>2</sub> temperatures and input air temperature. For the heat transfer model validation, the air outlet temperatures predicted by the model and measured during the experiment were compared. The outlet temperatures comparison is shown in Figure 18, where the predicted air outlet temperatures are matching the experimental data with reasonably good precision, where the predicted temperatures fit within  $\pm 10\%$  of the measured values and the absolute average deviation is 4.5 %.

Regarding the hydraulic model validation, the pressure differences predicted by the model were compared with the experimental measurement. The comparison of the pressure difference on the air side is shown in Figure 19, where the predicted pressure drops fit within  $\pm 35\%$  of the measured values and the absolute average deviation is 17 %. In the case of pressure drop prediction on the sCO<sub>2</sub> side, the prediction fits reasonably well with measured values. The comparison with measured values is shown in Figure 20, where the predicted pressure drop fits within  $\pm 25\%$  of the measured values and the absolute average deviation is 8.2 %.

A slightly higher deviation at the pressure drop predictions on the air side is mainly caused by the initial uncertainty of the mass-flow measurements and resulted calculation of the average heat transfer, which was the main input in the model. Despite this fact, the numerical model predicts reasonably well the thermal performance as well as the hydraulic and can be considered validated.

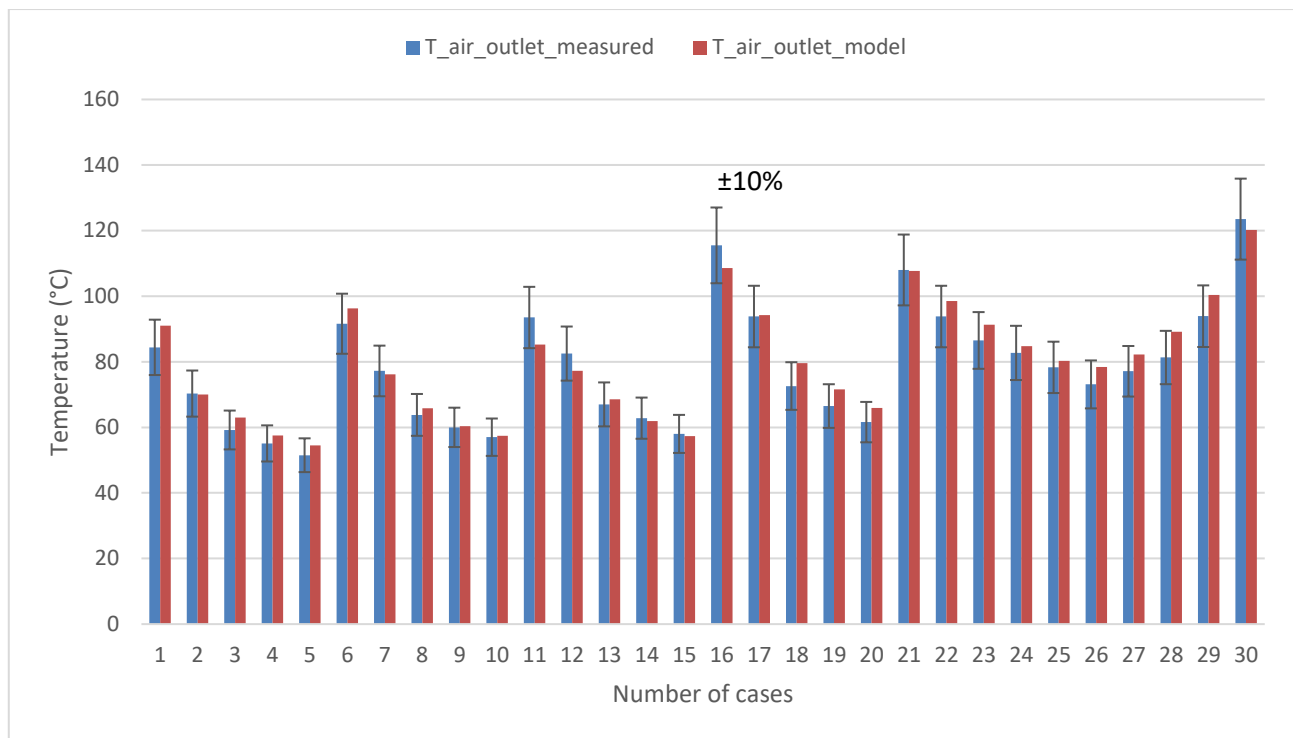


Figure 18: Comparison of the air outlet temperatures. Model vs. experimental data.

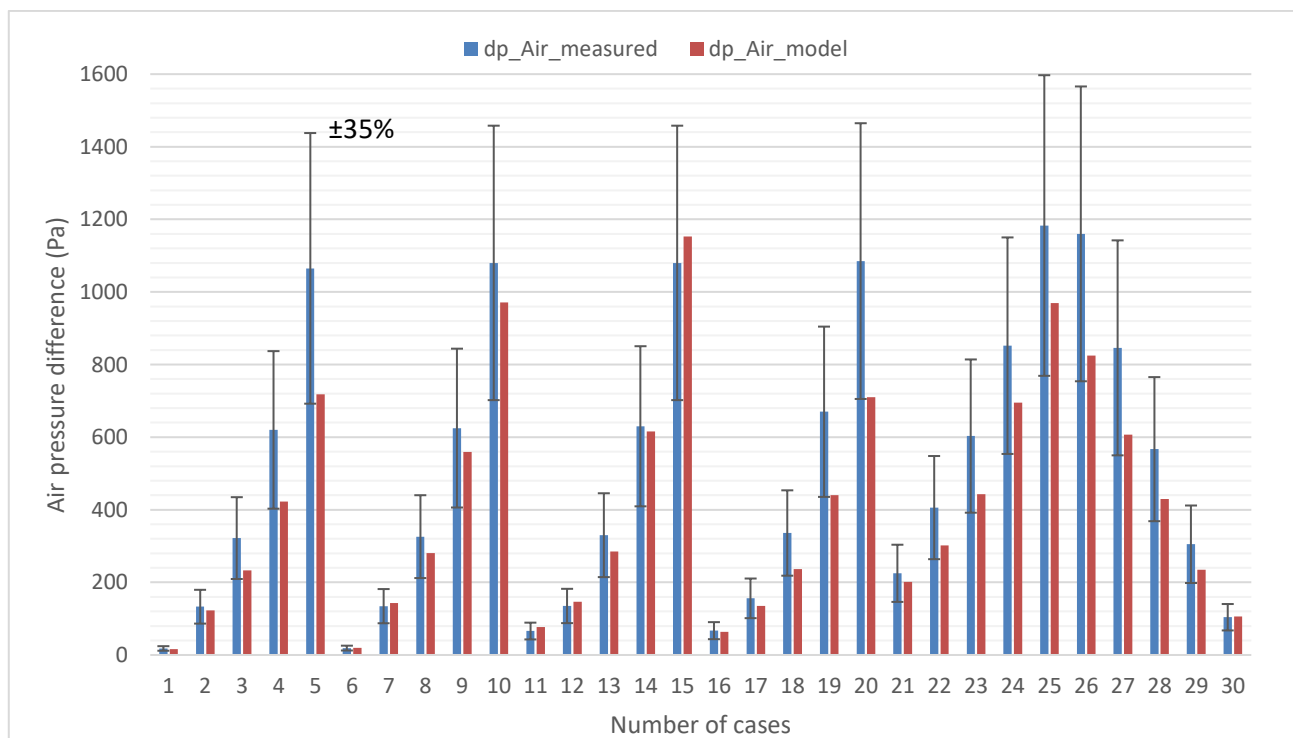


Figure 19: Comparison of the pressure difference on the air side. Model vs. experimental data.

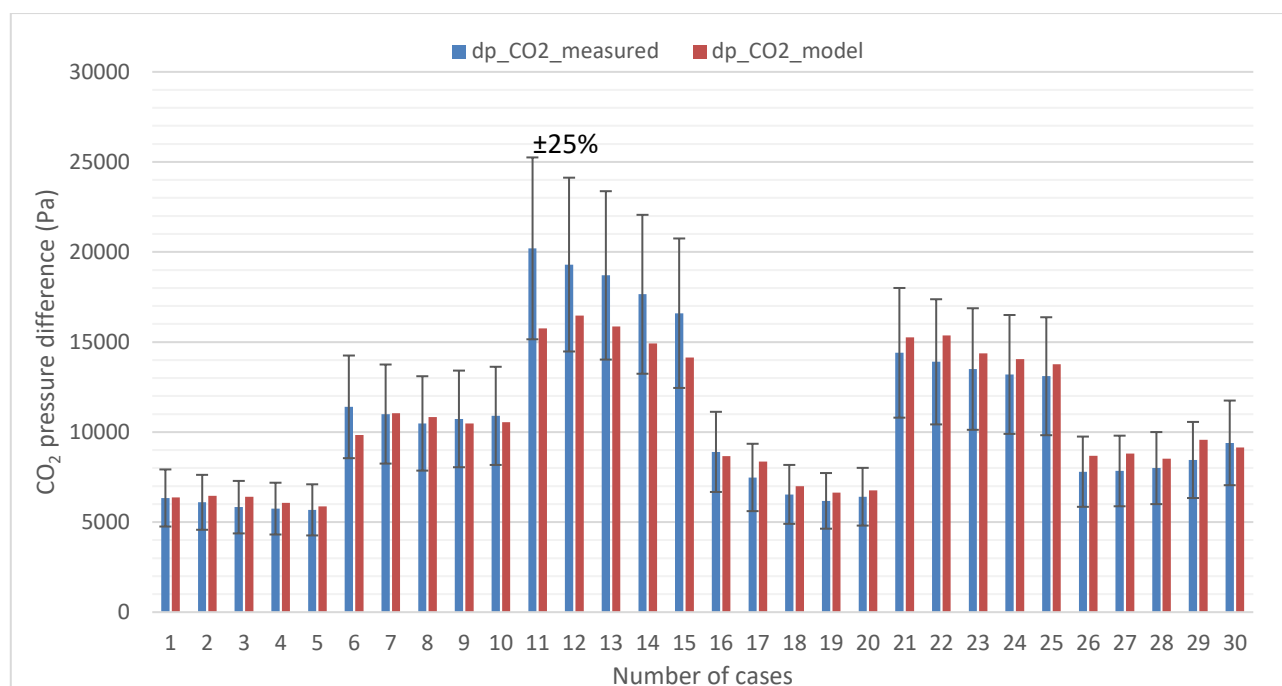


Figure 20: Comparison of the pressure difference on the sCO<sub>2</sub> side. Model vs. experimental data.

#### 4.4 DUHS core thermal-hydraulic review

The validated thermal-hydraulic code was used to review the current design of the DUHS core according to the datasheet [4]. A comparison of the basic HX parameters is present in Table 3. It can be seen from the comparison that the thermal performance of the presented model shows better performance than it was previously considered, mainly due to the corrected heat transfer correlation on the air side, which has a significant effect on the overall heat transfer coefficient. Another effect of the enhancement of the overall htc is that less air mass flow is required to transport the same amount of heat by a given heat transfer area. That results in the reduced channel velocity, which has again an impact on heat transfer coefficient and pressure drop. Therefore, the geometry and number of DUHS channels on the air side can be further optimized to reach the optimum between velocity and pressure drop to obtain a more compact heat exchanger design.

Table 3: Comparison of the DUHS core thermal-hydraulic performance. Datasheet vs. presented model.

		FIVES datasheet[4]		presented model Preliminary design	
Fluid		CO <sub>2</sub>	Air	CO <sub>2</sub>	Air
Total flow rate/core	kg/s	1.5245	6.6245	1.575	4.1
Operating pressure	MPa(a)	11.92	0.1	12	0.1
Temperature in	°C	238.66	45	238.66	45
Temperature out	°C	54.88	115.36	55	154.7
Simulated heat transferred/core	kW	471.85		471.85	
LMDT	°C	44.93		34.76	
U	W/m <sup>2</sup> K	7.9		10.4	
Calculated pressure drop	kPa	13.4	0.3	14.2	0.27
Total heat transfer area/core	m <sup>2</sup>	534.7	793.9	545.2	764.6

## 4.5 Air side channel optimization

An optimization task was made to find a straight fin channel geometry that maintains a high heat transfer coefficient with low pressure drop. A new heat transfer and friction factor correlations obtained from the experimental results will be used for this purpose. The optimization parameters are the channel's pitch, height and fin thickness. Possible limits for these parameters were discussed with the HX manufacturer FIVES Cryo and are presented in Table 4. For the optimization task a single channel is considered with the following constraints:

- channel length 1 m
- constant flow velocity 8 m/s
- maximum allowable pressure 600 Pa/m
- constant air thermo-physical properties at mean temperature  $T_m = 70^\circ\text{C}$
- contraction/expansion ratio  $\sigma = 0.5$

The velocity value of 8 m/s was chosen as decent trade between heat transfer and pressure drop and the pressure drop limit of 600 Pa/m was chosen so that the overall pressure drop of actual DUHS, which has a length of 0.64 m, won't cross a value of 400 Pa, which is often the limit value of most of the commercial axial fans, hence requirements for the low pressure drop are high.

A channel's hydraulic diameter for each possible combination of  $P(i)$ ,  $H(j)$ , and  $t(k)$  was calculated as:

$$D_{h,i,j} = \frac{2 \cdot (P_i - t_k) (H_j - t_k)}{(P_i - t_k) + (H_j - t_k)} \quad (4-32)$$

An array of Reynolds numbers was obtained using Eq. ( 4-30 ), and then the heat transfer coefficient was calculated as a function of Reynolds number as follows:

$$htc_{i,j} = \frac{Re_{i,j} \mu c_p j}{D_{h,i,j} Pr^{2/3}} \quad (4-33)$$

Where Eq. ( 4-14 ) was used to obtain Colburn factor  $j$ . Total surface effectiveness  $\eta_o$  according to Eq. ( 4-7 ) was also considered. The pressure drops were calculated according to Eq. ( 4-31 ) with considered fanning friction factor from Eq. ( 4-16 ) and Eq. ( 4-17 ).

**Table 4: Intervals of the air channel optimization parameters.**

Channel parameter	Interval [mm]
Pitch – P	<1; 5>
Height – H	<2; 8>
Fin thickness - t	<0.1; 0.3>

To find an optimum between high heat transfer coefficient and low pressure drops, a weight ratio system was utilized. The pressure drops were linearly scaled between values in <0; 1>, where the zero value was assigned to an array with >600 Pa/m, which is considered maximum allowable pressure and a value of 1 was assigned to the minimum calculated pressure drop. The same was carried out with heat transfer coefficient where 1 was considered the maximum calculated  $htc$  and zero was considered the minimum  $htc$  in the array. The final weight was obtained by multiplying each weight.

### 4.5.1 Air side channel optimization results and findings

According to the results, the increase in given dimensions of fin thickness has a positive effect on the fin efficiency (Figure 21), which is projected into a slight increase in the effective heat transfer coefficient presented in Figure 22. Hence, a fin thickness of 0.3 mm can be proposed for the channel design. Combining the smallest given pitch  $P$  and height  $H$  values, a maximum effective heat transfer coefficient up to  $htc = 41.7 \text{ W/m}^2\text{K}$  for given boundary conditions can be reached. However, this combination also contains the point with the highest calculated pressure drop with a value of  $\Delta p = 3110 \text{ Pa}$ , which five times exceeds the given allowable limit (Figure 23). When utilizing the weight ratio system, where the maximum allowable pressure drop is  $600 \text{ Pa/m}$ , a surface contour is obtained presented in Figure 24. The presented surface has a visible hyperbolic ridge, where the final weight reaches its maximum, which represents an area with an optimum trade-off between the heat transfer coefficient and sufficiently low pressure drop. The preliminary design point was marked on this surface alongside with other 5 points lying near the region with a local maximum shown in Figure 25. The values of the effective heat transfer coefficient and the pressure drops for each point as well as the preliminary design point are presented in Table 5. It can be noted that the preliminary design point has the highest value of the effective  $htc$  from the given points namely 8.2 % more than the average of 5 points. However, the pressure drop is also the highest with 55.5 % than the average of 5 points. The differences in the followed values between the considered points are negligible, therefore the final design is chosen according to the matching aspect ratio  $H/P$  as the same geometry of the DUHS mockup, where the experimental results were obtained and thus the results should match more closely. Hence, according to the data, the geometry at point 4 can be recommended for the final design.

Table 5: Air channel optimization points.

	$P$ [mm]	$H$ [mm]	$H/P$	$htc.n_0$ [ $\text{W/m}^2\text{K}$ ]	$\Delta p$ [Pa/m]
<b>Preliminary design</b>	2.54	4	1.57	29.9	422
<b>1</b>	4	3.8	0.95	27.9	263
<b>2</b>	3.6	4	1.11	28.1	283
<b>3</b>	3.4	4.5	1.32	27.7	267
<b>4</b>	3.2	5	1.56	27.4	269
<b>5</b>	3	5.5	1.83	27.1	275

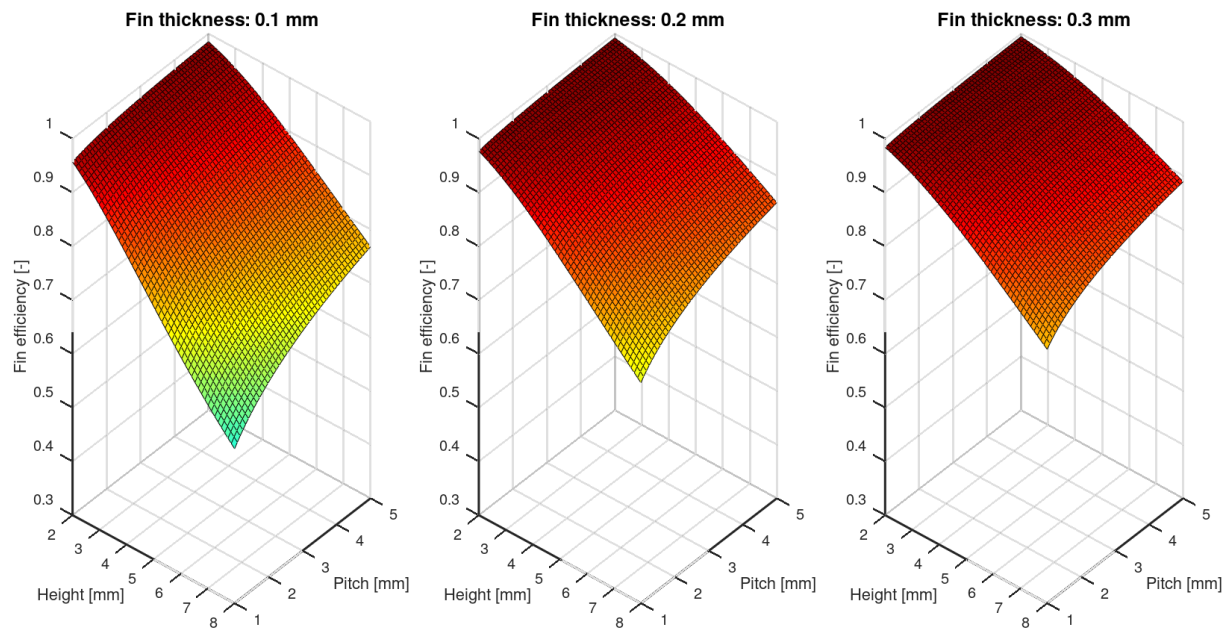


Figure 21: Comparison of a fin efficiency for different fin thicknesses.

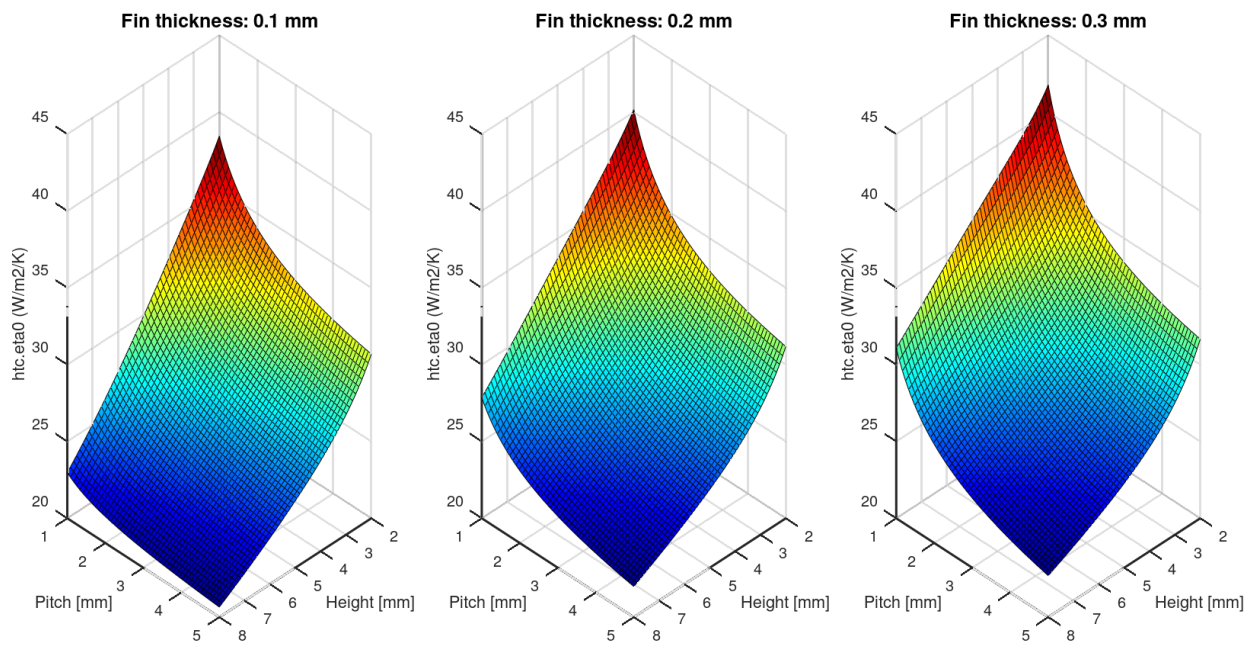


Figure 22: Comparison of an effective heat transfer coefficient for different fin thicknesses.



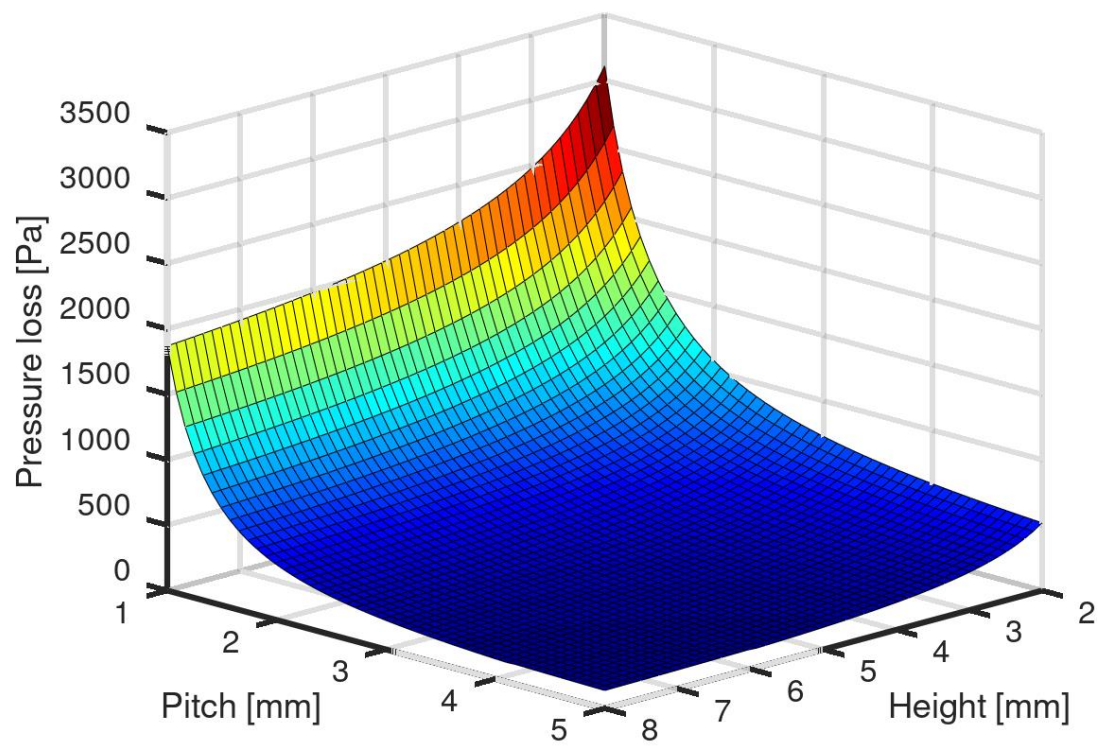


Figure 23: Pressure drops surface contour.

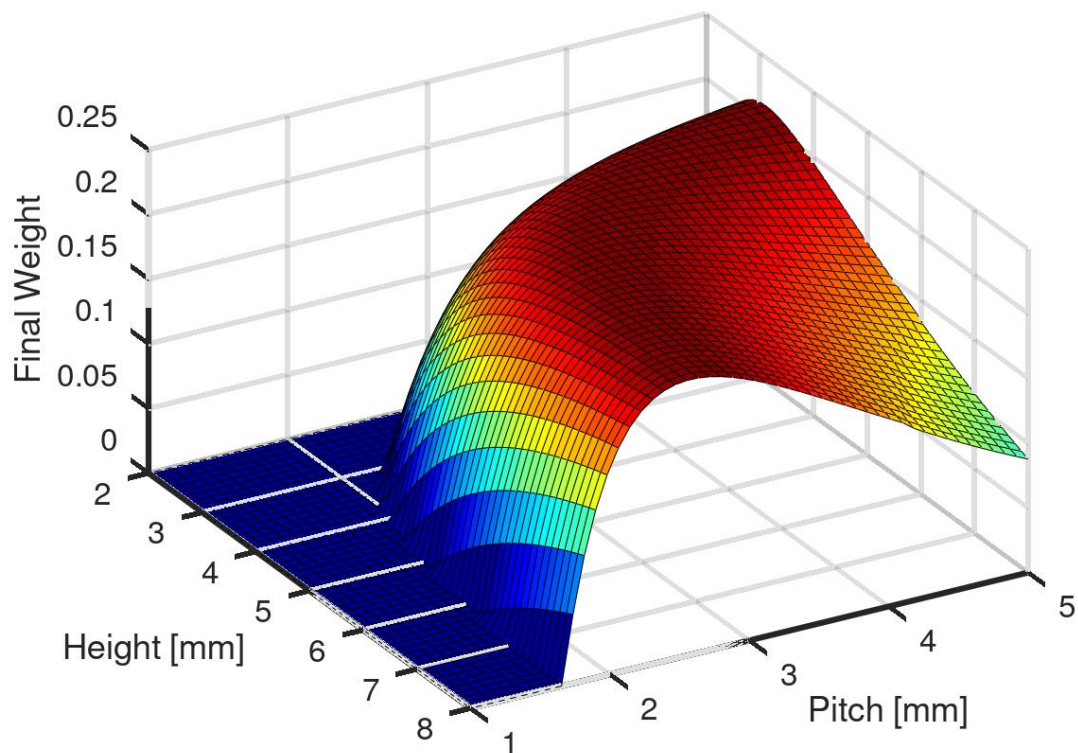


Figure 24: Final weight ratio surface contour.

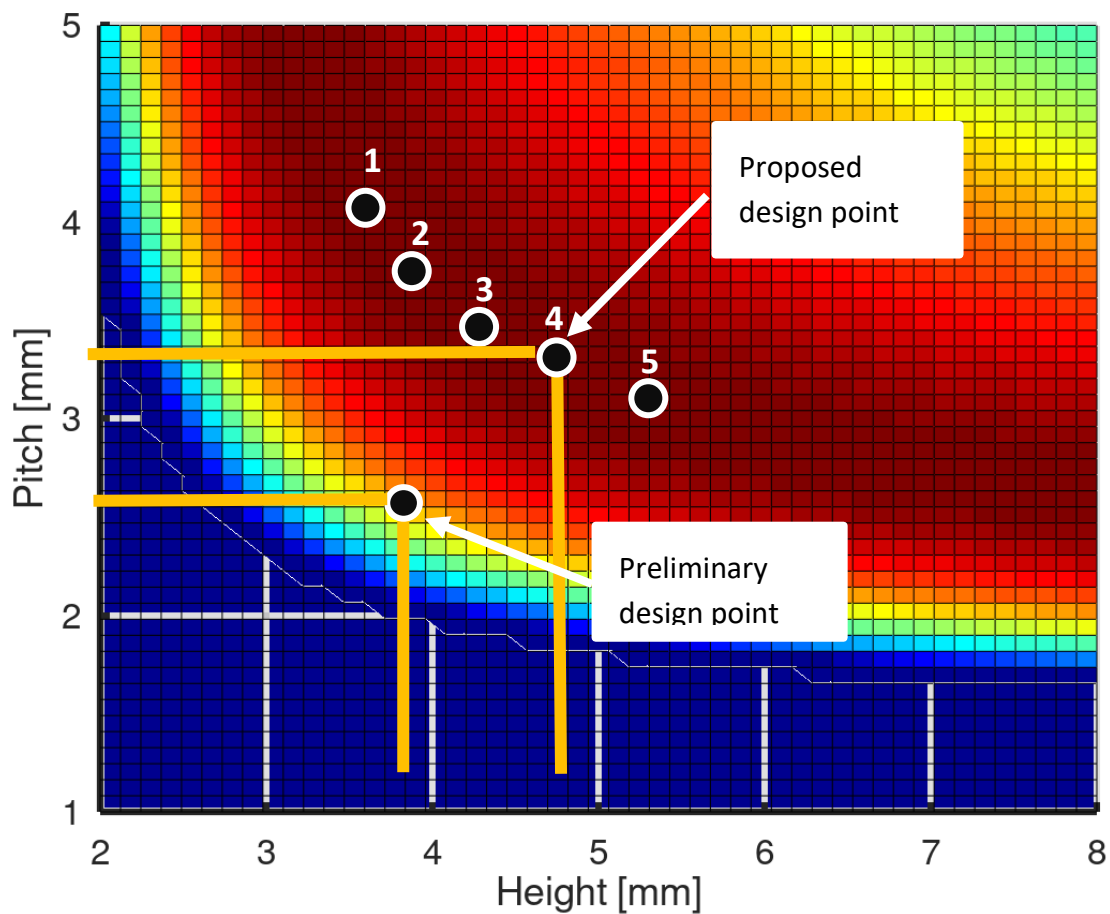


Figure 25: Final weight ratio surface contour - top view.

#### 4.5.2 Air side channel optimization – multiple design points

The same process as described in section 4.5.1 was repeated for multiple channel velocities and the following parameters with constant  $H/P = 1.5$  were proposed and are presented in Table 6. These parameters were fed into the validated code with the same boundary conditions per core as described in section 4.4, where the variables were the air channel fin pitch, height and total HX width that was modified in a way to obtain the average flow velocity listed for each point in Table 6. From the results, a function of total heat transfer area per core to transfer 471.85 kW of heat and average air velocity was made, which was compared with the necessary power requirements for the ventilator. The ventilator power was calculated as:

$$P_{Vent} = \frac{\dot{m}_{air} \Delta p}{\rho_i \eta_{vent}} \quad (4-34)$$

Where the ventilator efficiency  $\eta_{vent}$  was considered to be 70 %. The comparison of the ventilator power requirements and the total heat transfer area as a function of an average air velocity is shown in Figure 26. It can be seen that with the velocity increase, the requirements for total heat transfer area significantly decrease same as the ventilator power requirements increase. These data can be interesting for the final energy and material costs assessment. The final channel geometry proposition for the channel flow velocity of 8 m/s as it is mentioned in section 4.5 is still valid since it still maintains a good balance between the total heat transfer area and ventilator power requirements.



Table 6: Optimized channel parameters for different flow velocities.

v (m/s)	P (mm)	H (mm)
2	1.8	2.7
5	2.8	4.2
8	3.2	5
10	3.5	5.25
12	4.8	7.2

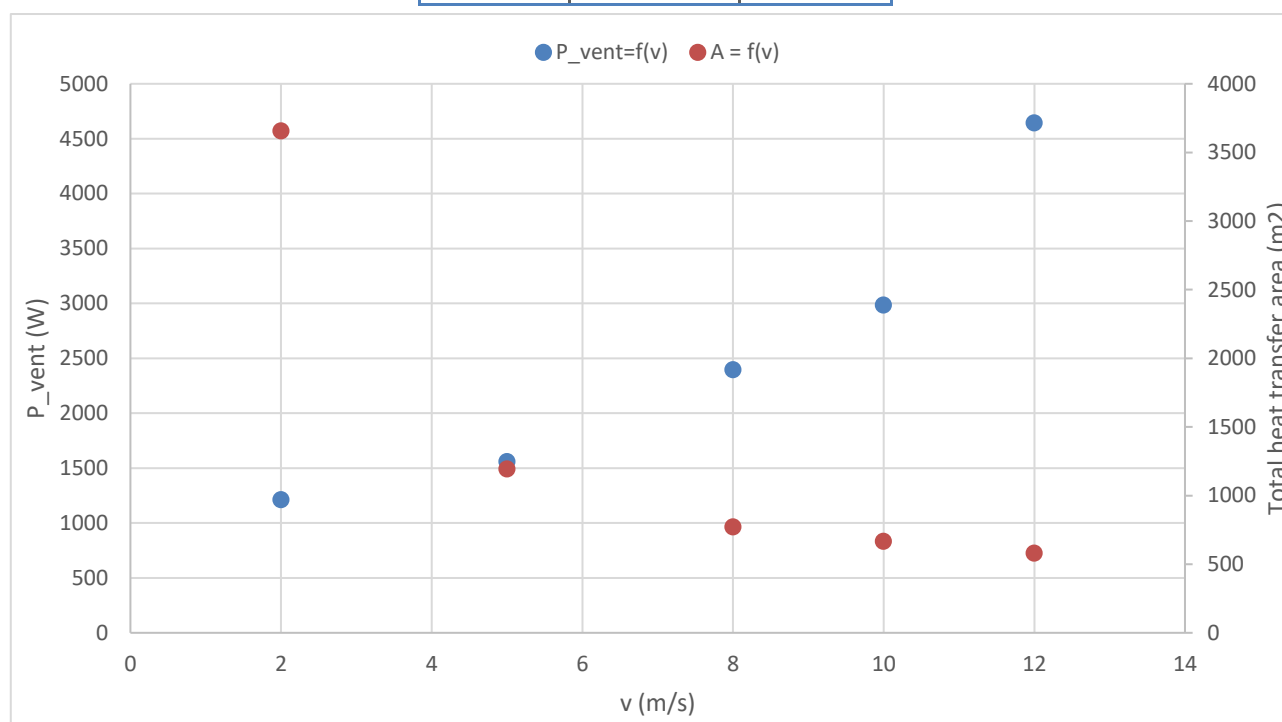


Figure 26: Comparison of the ventilator power requirements and necessary total heat transfer area as a function of an average air velocity.

## 4.6 Conclusion – Air side channel

To test and verify the DUHS design, a small mockup unit was experimentally tested. The experimental data revealed the thermal-hydraulic characteristics, which were used to extrapolate the heat transfer coefficients on the air side and the Fanning friction factors of both mediums. A numerical code was developed and validated using the extrapolated correlations. The results show that the thermal performance of the heat exchanger was far better than it was previously anticipated in the preliminary design, mainly due to the corrected heat transfer coefficient on the air side, which significantly affects the overall heat transfer coefficient and thus the requirements for the heat transfer area.

Furthermore, an air channel optimization study was done, using the validated data, to find the geometry with optimal heat transfer with sufficiently low pressure drop. The results of this study show that increasing the fin thickness has a positive effect on increasing the heat transfer coefficient and that the optimum field exists for the given boundary conditions. The optimization study was made for multiple air channel velocities, where the function relation of the air flow velocity on the ventilator power and the total heat transfer area requirements was presented. According to the results a final air channel geometry was proposed (**P= 3.2 mm; H= 5 mm; t= 0.3 mm**).

## 5 Design strategy for channels and flow distribution area for the sCO<sub>2</sub> side of the heat sink HX

---

### 5.1 Expected operating conditions

As part of D4.4, multiple one-dimensional simulations of the whole sCO<sub>2</sub> heat removal system in ATHLET were carried out for various conditions [3]. Thereby the design point for the DUHS was defined at a pressure of 12.70 MPa, an inlet temperature of 243.19 °C and a mass flow rate of 29.74 kg/s [3]. The information from FIVES' current datasheet agrees reasonably well with these data [13]. The inlet pressure is set to 11.92 MPa, the inlet temperature to 238.66 °C and the mass flow rate to 30.49 kg/s.

There are multiple ways to start the sCO<sub>2</sub> heat removal system, mainly the push-up start and the operational readiness state start. The operational readiness state (ORS) keeps the CO<sub>2</sub> in "hot" starting conditions during the normal operation of the NPP [3]. These starting conditions are close to the design point and therefore the CO<sub>2</sub> is already in a supercritical state [14]. In D5.4 [15], a push-up start was simulated considering an ambient air temperature of 45 °C. At this ambient air temperature, the CO<sub>2</sub> maintains gaseous throughout the entire push-start. It is assumed that the CO<sub>2</sub> will be in the two-phase region when the ambient air temperature decreases to -45 °C. However, no results of simulations for the decreased ambient air temperature are currently available. Thus, the simulations in this deliverable are carried out with single-phase CO<sub>2</sub>.

After the start-up of the sCO<sub>2</sub> heat removal system in case of an accident, the six units of the system will be shut down successively with the decreasing decay heat over time. USTUTT carry out ATHLET simulations to investigate the influence of shutting down the units on the absolute pressure and found that the influence on absolute pressure is negligible. Thus, the chosen pressure at the inlet of the flow distribution area for the simulations in this deliverable is 12.7 MPa, which represents the design pressure of the DUHS. Since the excess power of the circuit is mainly dependent on the isentropic enthalpy difference over the turbine resp. the turbine inlet temperature, the shaft speed control system ensures a constant turbine inlet temperature by varying the rotation speed of the turbine. The constant turbine inlet temperature of the sCO<sub>2</sub> results in an approximately constant DUHS inlet temperature of 240 °C [15]. Since this value is similar to the design temperature, the inlet sCO<sub>2</sub> temperature at the DUHS is set to 243.19 °C. As mentioned above, the shaft speed control system regulates the speed rotation of the turbine and thereby the mass flow rate. For this reason, the mass flow rate is the only parameter with transient behaviour. Therefore, the steady-state simulations are first carried out at the design point with 29.74 kg/s and then at the mean value of the mass flow rate from the simulation at an ambient air temperature of 45 °C [15] with 13.55 kg/s to consider a transient point.

### 5.2 Preliminary design parameter of the fin and header geometry on the sCO<sub>2</sub> site

The design of the DUHS core can be found in Chapter 4.1. The preliminary straight fin geometry for the sCO<sub>2</sub> side proposed by FIVES is displayed in Figure 2, where the fin thickness  $t$  is 0.3 mm the fin width  $p$  is 1.27 mm and the fin height, which is also the height of one layer, is 4 mm. This results in 787.4 fins per meter. To gain space, each layer is constituted of six passages and thus the CO<sub>2</sub> is redirected by 90° multiple times, which is displayed Figure 1 [3].

For the flow distribution into the channels, FIVES uses a header geometry, which is shown in Figure 27 and Figure 28. In the following, the semi-circular shaped geometry and the two inlet pipes are referred to as the manifold. The outer diameter of the semi-circle is 223 mm and the wall thickness is 17.5 mm. The inlet pipes are placed symmetrically at a distance of 329 mm from the edges and the inner diameter is 38.14 mm [3].

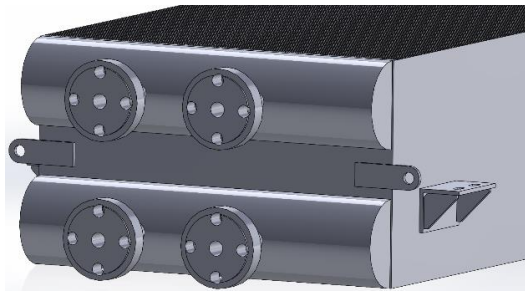


Figure 27: Side view of one core.

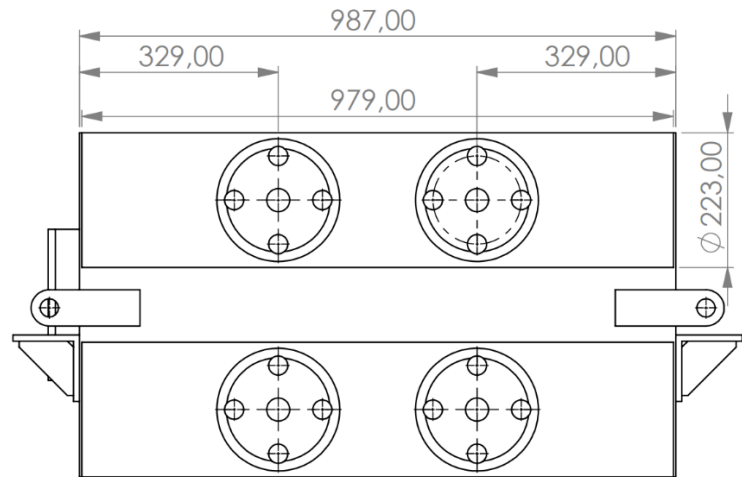


Figure 28: Front view of one core.

### 5.3 Design strategy for channel geometry of the sCO<sub>2</sub> side

In this chapter, the focus is on different channel geometries and designs. To get an overview, a literature study is carried out in the first part of the chapter (chapter 5.3.1) to present the state of research and to use interesting findings for the evaluation of different channel designs for this deliverable. In the second part (chapter 5.3.2), the main results from the sCO<sub>2</sub>-Flex project are presented. First the results from the experimental investigations on tiny channels close to the critical point and then the results from the investigations of the two heat exchangers manufactured by FIVES in a large and different range of operating conditions. Starting with these results from the sCO<sub>2</sub>-Flex project, a performance comparison of the two heat exchangers with different fin designs is carried out. Finally, using the results of the literature study and the sCO<sub>2</sub>-Flex project, the best channel design will be proposed.

#### 5.3.1 Evaluation and comparison of the different channels and fin geometries

Since the overall DUHS design with a plate and fin heat exchanger was already chosen, the literature study is limited to the most important studies on the fin geometries and designs. Furthermore, it should be noted that the fins have to fulfil several tasks in this type of DUHS: The improvement of the heat transfer, the flow guidance, the flow re-direction and the increase of the structural integrity. At this point, only the improvement of heat transfer and the reduction of pressure drop through the different fin designs will be discussed. An overview of the different fin designs is given in Figure 29. The most commonly used are straight fins (b), serrated fins (d) and perforated fins (f).

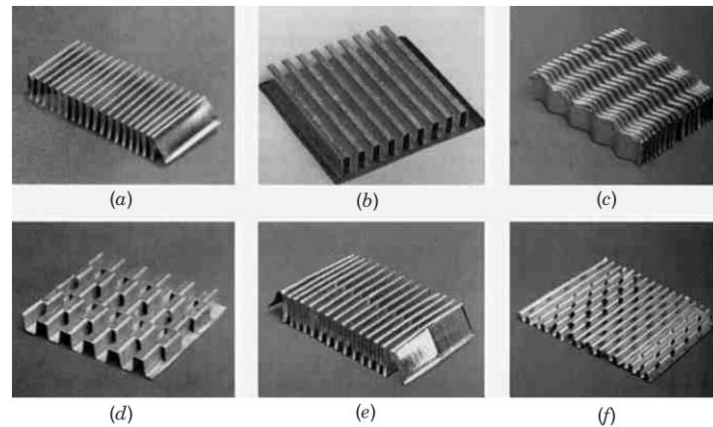


**Figure 29: Different fin designs: (a) plane triangular fin; (b) plain rectangular fin or straight fin; (c) wavy fin; (d) offset strip fin or serrated fin; (e) multi louver fin; (f) perforated fin [16].**

Before presenting the literature results, the basic equations that are usually used for determining the performance of the plate and fin heat exchanger should be explained first. The Colburn factor  $j$  Eq.( 5-1 ) is a parameter for the heat transfer and the Fanning factor  $f$  Eq.( 5-2 ) is a parameter for the pressure drop. The heat transfer coefficient is  $htc$ ,  $Pr$  the Prandtl number,  $\rho$  the density,  $v$  the velocity of the fluid,  $c_p$  the isobaric heat capacity of the fluid and  $\Delta p$  is the pressure drop along the fin length  $l$ .

$$j = \frac{htc Pr^{2/3}}{\rho v c_p} = \frac{htc A Pr^{2/3}}{\dot{m} c_p} \quad (5-1)$$

$$f = \frac{\Delta p}{l} \frac{d_h}{2 \rho v^2} = \frac{\Delta p d_h A^2 \rho}{l 2 \dot{m}^2} \quad (5-2)$$

Manglik and Bergles [17] reanalyzed the existing Fanning and Colburn data and showed the asymptotic behaviour of the data in the laminar and fully turbulent flow regimes. They developed a thermal-hydraulic design tool for serrated fins. To understand the performance of different heat exchanger surfaces relative to their geometrical attributes, the flow area goodness factor  $j/f$  was used. The area goodness factor represents a direct comparison of the ratio  $j/f$  as a function of Reynolds to determine which heat exchanger requires the minimum frontal area, which results from the cross-sectional area of the fins, for a fixed pressure drop.

An extensive experimental study on the channel shape performance of various fin designs including plain, perforated, offset strip, louvered, wavy, vortex-generator, and pin, was conducted by Khoshvaght-Aliabadi [18]. Water was the working fluid at a Reynolds number of 480 to 3770. The three most commonly used energy-based performance evaluation criteria were used to evaluate the performance, including the area goodness factor. In the overall comparison of all channel shapes, the vortex generator fin showed a significant improvement in heat transfer and a proper reduction of the heat exchanger surface. Also when considering the area goodness factor, the results showed that the vortex generator fin has the best ratio between heat transfer and pressure drop.

An innovative form of offset strip fin arrays was investigated by Peng et al. [19]. Numerical and experimental studies were carried out with air at a Reynolds number of 500 to 5000 to determine the influence of different geometric parameters on thermal-hydraulic performance. It was shown that the Colburn factor decreases and the Fanning factor increases as the fin pinch decrease. The Colburn factor and the Fanning factor increase as the fin length decreases.

Chen et al. [20] conducted numerical studies to investigate straight and serrated fin heat exchangers for use in high-temperature gas-cooled reactors. They showed that the best thermal-hydraulic performance was achieved by the serrated fins with a length of 3.5 mm.

Ganzarolli and Altemani [21] optimize the thermal design of a counterflow heat exchanger with air as a working fluid. They varied the fin thickness and the fin spacing and found that the fin spacing had a higher influence on the thermal design. Thus, they suggest that the optimal fin spacing should be carefully selected for an appropriate thermal design.

Li and Wang [22] carried out experiments with air flowing in brazed aluminium heat exchangers with multi-region louvre fins and flat tubes. Their investigations include seven different multi-region louvre fin geometries at a Reynolds number between 400 and 1600. They found that the thermal-hydraulic performances of the 4-region louvre fin and the 6-region louvre fin are better than the traditional fin geometry.

Najafi et al. [23] investigated plate and fin heat exchangers with serrated fins and air as working fluid and carried out heat transfer optimisations and cost optimisations. Various geometrical parameters were varied for optimisation, such as the total length of the heat exchanger, the fin height and fin frequency, the width of the fins and the number of fin layers. They found that each improvement in heat transfer increased annual costs. For this reason, they used a multi-objective genetic algorithm to generate a range of optimal solutions for the end-user, depending on the requirements.

### 5.3.2 Experimental results of the sCO<sub>2</sub>-Flex project

#### 5.3.2.1 sCO<sub>2</sub>-cooling in tiny channels near the critical Point

To investigate the fundamental heat transfer characteristics of cooled sCO<sub>2</sub>-flows in small channels, experimental investigations were carried out at the USTUTT using tubes with inner diameters of 2 mm and 3 mm. The tubes with the sCO<sub>2</sub>-flows were cooled by water flowing in annular channels. The dimensions and construction data of the pipes can be seen in Figure 30 and Table 7.

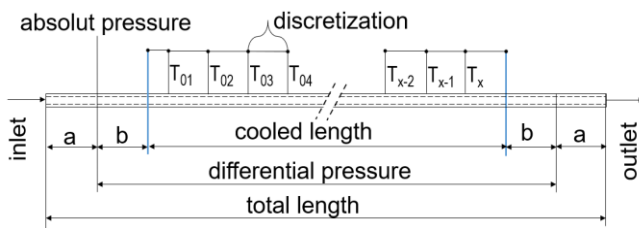


Figure 30: Dimensions of the test channels [24].

Table 7: Construction data of the test channels.

	2 mm	3 mm
<b>cooled length [mm]</b>	1200	500
<b>number of tc's [-]</b>	29	12
<b>discretization [mm]</b>	40	40
<b>positioning of tc's</b>	Alternating	One-sided
<b>total length [mm]</b>	1500	1000
<b>diff. pressure [mm]</b>	1386	700
<b>a [mm]</b>	57	150
<b>b [mm]</b>	93	100

Starting with the tube with a 2 mm inner diameter, experiments were carried out in a sCO<sub>2</sub>-parameter range with pressures of  $77 \leq p_{in} \leq 85 \text{ bar}$ , mass fluxes of  $400 \leq G \leq 1300 \text{ kg}/(\text{m}^2\text{s})$  and inlet temperatures of  $10 \leq T_{\text{CO}_2, \text{in}} \leq 85 \text{ }^\circ\text{C}$ . The cooling media temperatures were  $10 \leq T_{\text{cool, in}} \leq 40 \text{ }^\circ\text{C}$  with a water volume flow of  $\dot{V}_{\text{cool}} = 100 \text{ ml/s}$ . The water temperature difference between the inlet and outlet of the annulus was on average  $1.13 \text{ }^\circ\text{C}$ . First, a parameter study was carried out. The results show that the heat transfer coefficient (*htc*) increases with an increase in mass flux and that the heat flux is overall higher with an increase in mass flux. The variation of the absolute pressure showed that with increasing absolute pressure, the peak values of the *htc* decrease and that in the liquid-like region the values for all pressures decrease to an approximately

similar level. Increasing the coolant inlet temperature from 10 °C to 20 °C leads to a slightly lower  $htc$  in the gas-like region of sCO<sub>2</sub>, while the peak value is significantly higher. In the liquid-like region, the tendency is reversed: a higher coolant temperature leads to a higher  $htc$  value. Furthermore, to verify the reliability, the inlet temperature of sCO<sub>2</sub> was varied with the result that the first three and the last four temperature values were not taken into account in further considerations. The experimental results of the 2 mm inner diameter tube were compared with heat transfer correlations from Liao and Zhao [25] and Dang and Hihara [26]. The comparison showed that the correlation of Dang and Hihara has strong deviations of more than 40 % from the experimental data and the correlation of Liao and Zhao can reproduce most of the experimental results within an error of  $\pm 40$  %. For this reason, a new correlation was proposed (see Eq.( 5-3 )) that can reproduce the experimental results with a mean deviation of 7.7 %. The coefficients for the equation can be taken from Table 8 [27; 28].

$$Nu_w = a_0 * Re_w^{a_1} * Pr_w^{a_2} * \left(\frac{\rho_b}{\rho_w}\right)^{a_3} * \left(\frac{cp}{cp_b}\right)^{a_4} * \left(\frac{k_b}{k_w}\right)^{a_5} * \left(\frac{\mu_b}{\mu_w}\right)^{a_6} \quad (5-3)$$

Table 8: Coefficient of the new correlation.

a0	a1	a2	a3	a4	a5	a6	
0.0495	0.771	0.455	1.450	-0.026	1.604	-2.623	for $T_w \geq T_{pc}$
0.0052	0.971	0.388	1.279	0.450	2.158	-2.923	for $T_w < T_{pc}$

The experimental investigations with the 3 mm inner diameter tube focused on the influence of the flow direction (horizontal, upward, downward) and on heat transfer deterioration and enhancement phenomena. The experiments were carried out in a sCO<sub>2</sub>-parameter range with pressures of  $p_{CO_2,in} = 80$  bar mass fluxes of  $141 \leq G \leq 354$  kg/(m<sup>2</sup>s), inlet temperatures of  $20 \leq T_{CO_2,in} \leq 51$  °C, a heat flux of  $\dot{q} = 12$  kW/m<sup>2</sup> and a water volume flow of  $\dot{V}_{cool} = 60$  ml/s. The investigations with horizontal flows showed that at lower mass fluxes, temperature stratification occurs in the liquid-like region with a maximum temperature difference of 2.5 °C between the tube bottom and the tube top. At higher mass fluxes and in the gas-like region of all mass fluxes, no temperature stratification could be recognised. In the vertical flow orientations, the experimental results of upward and downward flow could be well reproduced by the Dang and Hihara [26] correlation for forced convection when the influence of buoyancy effects was small. As the buoyancy effects increased, the results between upward and downward flow deviated, where heat transfer was enhanced in upward flow and deteriorated in a downward flow [29; 30].

### 5.3.2.2 Testing of plate and fin heat exchanger prototypes

The second focus of USTUTT in the sCO<sub>2</sub>-Flex project was on the experimental investigation of heat exchanger prototypes manufactured by FIVES. These results are of particular interest for this report, as two identical heat exchangers with different fin designs were investigated. The study aimed to test the two heat exchangers in a large and different range of operating conditions, to investigate the influence of the different parameters on the heat transfer and pressure drop and check whether the prediction methods for the pressure drop and the heat transfer of FIVES can reproduce the experimental results with sufficient accuracy. The 3D drawing and the dimensions can be seen in Figure 31 and Figure 32. The heat exchangers consist of two fluid layers, one for sCO<sub>2</sub> and one for water as cooling media. The heat exchange area of both layers is symmetrically and consists of five subsections with a length of 50 mm each. The 4 mm gap between the subsections enables the installation of measurement devices. The total heat exchanger volume is (950x45x75) mm<sup>3</sup> (LxHxW) [24].

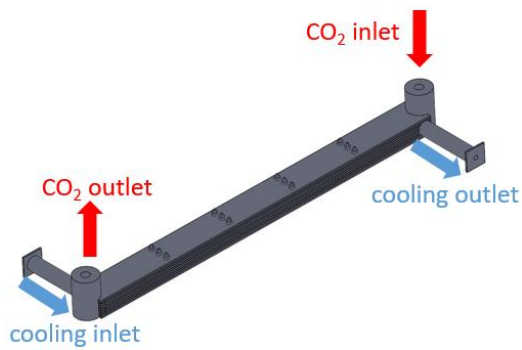


Figure 31: Plate and fin heat exchanger prototype [24].

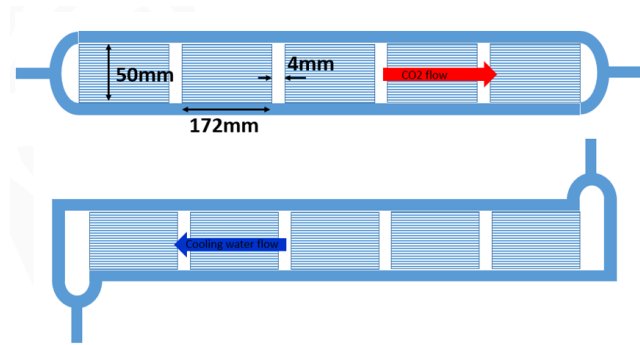


Figure 32: Dimensions of the prototype [24].

The cross-section of the heat exchanger prototypes consists of eight layers (Figure 33), of which six are dummy layers to ensure the pressure stability of the heat exchanger. Straight fins were installed in one heat exchanger (Figure 34) and serrated fins in the other one (Figure 35). The hydraulic diameter of the straight fin geometry is 2.95 mm and of the serrated fins 2.26 mm. The dimensions of the fins differ slightly from the initial heat exchanger design of FIVES. The height of the fins remains constant at 4 mm and the thickness of the material is 0.15 mm instead of 0.3 mm. The width of the straight fins is 2.39 mm and the width of the serrated fins is 1.59 mm. This results in a fin frequency of 629.9 fins per meter for the straight and 393.7 fins per meter for the serrated fins. As a reminder, the width of the fins from the initial DUHS design is 1.27 mm, resulting in a frequency of 787.4 fins per meter. Nevertheless, the different fin designs and geometries can be directly compared due to the same structure of the heat exchanger prototypes [24].

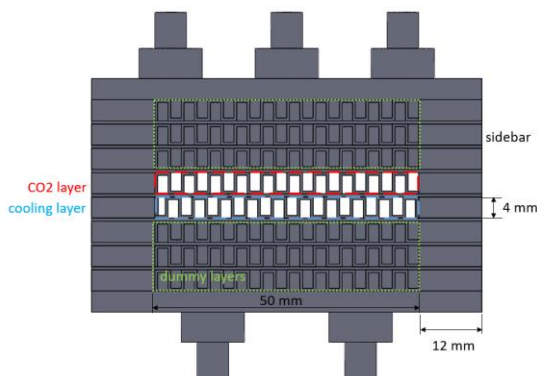


Figure 33: Layer arrangement of the prototypes [24].

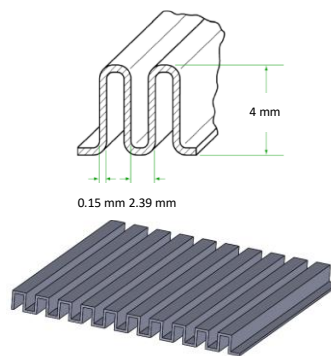


Figure 34: Straight fins [24].

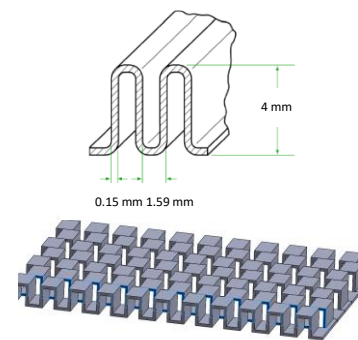


Figure 35: Serrated fins [24].

Starting with the experimental results of the serrated fin heat exchanger prototype, five measurement campaigns (three isothermal and two cooled) were carried out at  $p_{CO_2,in} = 80 \text{ bar}$  to determine the pressure drop and to verify the theoretical prediction methods. The results have shown that the prediction methods and the calculation of the fanning factor according to FIVES are sufficiently accurate and can predict the experimental results within an error band of  $\pm 20 \%$ . Next, the influence of the flow directions was investigated. For this purpose, the flow directions (horizontal, upward and downward), the sCO<sub>2</sub> mass flux and inlet temperature and the cooling media volume flow and inlet temperature were varied. Again, the results show that for the pressure drop the experimentally determined fanning factor can be described within an error band of  $\pm 20 \%$  with the theoretical prediction method. The results of the heat transfer showed that the influence of the flow direction on the  $htc$  is not significant. In a final step, the heat transfer performance of the heat exchanger for  $80 \leq p_{CO_2,in} \leq 85 \text{ bar}$  was investigated in three measurement campaigns. According to the results, the FIVES prediction data can also reflect the  $htc$  results well within an error band of  $\pm 20 \%$  [24].



The investigation with the straight fin heat exchanger prototype was carried out at a pressure of  $p_{\text{CO}_2,\text{in}} = 80 \text{ bar}$ . In three measurement campaigns, the mass flow rate and the inlet temperature were varied on the sCO<sub>2</sub> side and the volume flow rate and the inlet temperature were varied on the waterside. The flow orientation was varied between downward flow and horizontal flow. An influence of the flow direction was found so that the heat transfer tends to be stronger for the downward flow. The differences in the transferred heat decrease for higher cooling media temperature and higher sCO<sub>2</sub> mass flux [24].

In a further investigation, the condensation through and into the two-phase region was examined with both heat exchanger prototypes. The experiments have been carried out at  $p_{\text{CO}_2,\text{in}} = 70 \text{ bar}, 72 \text{ bar}$ ,  $20 \leq \dot{m}_{\text{CO}_2} \leq 40 \text{ g/s}$ ,  $T_{\text{CO}_2,\text{in}} \approx 30 \text{ }^\circ\text{C}$ ,  $\dot{V}_{\text{cool}} = 60 \text{ ml/s}$  and  $T_{\text{cool}} \approx 5 \text{ }^\circ\text{C}$ . The heat transfer results are shown in Figure 36. It can be seen that for both heat exchangers and both pressures the  $h_{\text{tc}}$  increases with increasing mass flow. Furthermore, the  $h_{\text{tc}}$  is higher at a pressure of 72 bar, i.e. closer to the critical pressure. In direct comparison, the heat exchanger with the serrated fins has about twice the heat transfer as the heat exchanger with the straight fins. Only at a mass flow of  $\dot{m}_{\text{CO}_2} = 20 \text{ g/s}$  the CO<sub>2</sub> is completely condensed. Also, for the two-phase area, the prediction methods for the heat transfer were found to give good results for both heat exchanger prototypes [24].

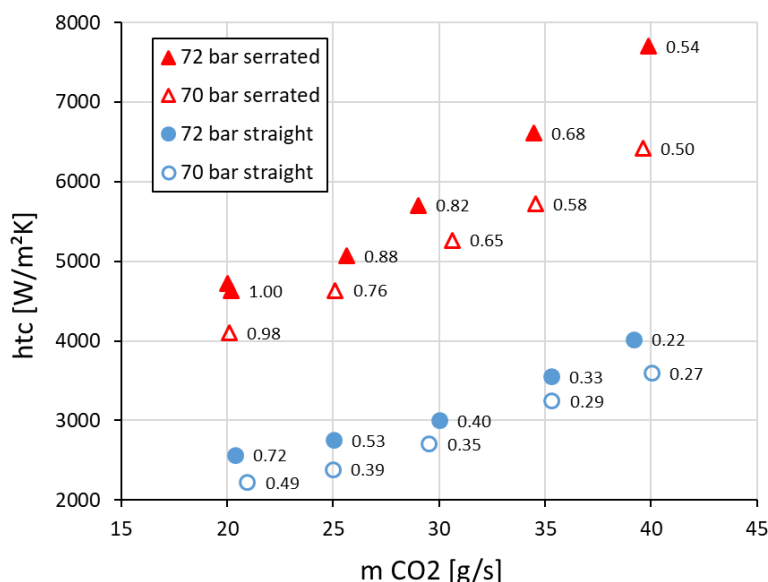


Figure 36:  $h_{\text{tc}}$  as a function of CO<sub>2</sub> mass flow [24].

### 5.3.2.3 Significance of the sCO<sub>2</sub>-Flex results for sCO<sub>2</sub>-4-NPP

The experimental results of the investigations on cooled sCO<sub>2</sub> in tiny channels can be further used for the validation of the basic heat transfer correlations in ATHLET. If larger deviations of the simulations from the experimental data occur, it can be assessed whether the newly developed correlation can be implemented for the valid parameter range. Direct use of the results for a proposition of a design strategy or channel geometry cannot be made due to the complexity of the fin structure in the DUHS.

The experimental results of the heat exchanger prototypes provide the first results of the heat transfer performance for the investigated fin designs. This is particularly interesting as these fin designs are available and can be used by FIVES. A direct comparison of the heat transfer in the two-phase region has shown that for the two selected geometries the heat exchanger with the serrated fins has an almost twice higher  $h_{\text{tc}}$ . Another important result is that the calculation methods of FIVES using the Fanning factor and the Colburn factor can predict the heat transfer and the pressure drop very precisely within an error band of  $\pm 20 \%$ . Thus,



the experimental results of the sCO<sub>2</sub>-Flex project can be seen as a verification of the prediction methods for CO<sub>2</sub> near the critical point (both in the single-phase and two-phase region).

With this information, it is possible to make a direct comparison of the different fin designs and geometries using theoretical methods. As already described in chapter 5.3.1, a dimensionless approach with the Colburn factor to the Fanning factor as a function of the Reynolds number is suitable for this. This approach makes it possible to look at the overall thermo-hydraulic performance in terms of heat transfer and pressure drop. This comparison of the overall thermo-hydraulic performance of the two investigated fin designs is shown in Figure 37 and Figure 38. Figure 37 shows the Colburn and Friction factors as a function of the Reynolds number. As in the study of Manglik and Bergles [17], all coefficients show an asymptotic behaviour. Starting with the Colburn factor, it can be seen that the heat transfer efficiency to the front area is higher with the serrated fin design, especially for low Reynolds numbers. This is mainly due to the continuous breaking of the thermal boundary layer by the design. This increase in turbulence also means that the pressure drop for the serrated fin design is higher, which is expressed in a higher fanning factor compared to the straight design. If only the heat transfer efficiency is considered, the serrated fin design is to be preferred, if only the low pressure drop is considered, the straight fin is to be preferred. To assess the overall thermodynamic performance, the area goodness factor can be used, which compares these two dimensionless parameters (Figure 38). Here it is clear that the overall thermo-hydraulic performance of the straight fins is better for the two investigated fin designs.

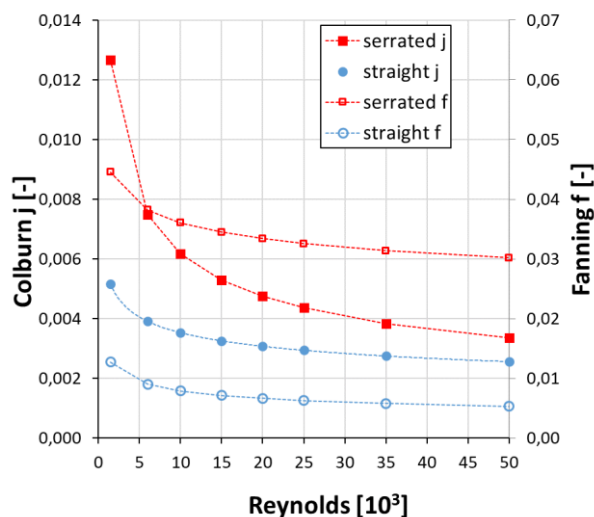


Figure 37: Colburn and Fanning factor for the investigated straight and serrated fin designs and geometries.

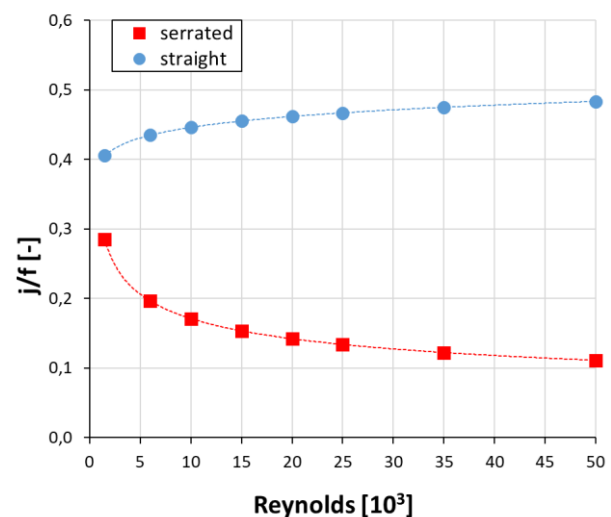


Figure 38: Thermo-hydraulic performance analysis of the investigated straight and serrated fin designs using the area goodness factor.

### 5.3.3 Main findings and proposition for the different channels and fin geometries

In the first part of this chapter (chapter 5.3.1), the different fin types and fin geometries were introduced. The Colburn factor  $j$  and the Fanning factor  $f$  were introduced which allow the comparison of the heat transfer and the pressure drop of different channel geometries. Using the area goodness factor  $j/f$ , these two factors can be correlated to compare the thermal-hydraulic performance of the design. The results of the literature study show that the serrated fins often provide the best thermal-hydraulic performance. Despite their good performance, the vortex generator fins are not suitable for use in the DUHS because the pressure stability of the heat exchanger is difficult to realise with this geometry.

In a second part (chapter 5.3.2), the most important experimental results of the sCO<sub>2</sub>-Flex project were presented, first for tiny channels and then for plate and fin heat exchanger prototypes. It was found that a direct transfer of the single-channel investigations to the DUHS is not possible, but the results can be used to validate basic correlations in e.g. ATHLET. The investigation of the two heat exchanger prototypes enabled a direct comparison of a straight fin and the serrated fin design. The experimental heat transfer performance at subcritical pressures ( $p_{CO_2,in} = 70 \text{ bar}, 72 \text{ bar}$ ) showed that the  $htc$  of the serrated fins is higher by a factor of two. Furthermore, a theoretical comparison of the thermal-hydraulic performance was carried out using the Colburn and Fanning factors. This comparison shows that the serrated fin design performs better in terms of heat transfer efficiency and the straight fin design performs better in terms of pressure drop. In the overall consideration using the area goodness factor, the straight fin design shows better results.

Overall, it can be concluded that the serrated fins can also be a good alternative for the DUHS if heat transfer efficiency is a priority. However, these results should be considered as a first proposition and do not replace the overall design of the heat exchanger. In the overall design, the additional consideration of costs, pressure stability and licensing may lead to different results.

## 5.4 Design strategy for the flow distribution of the sCO<sub>2</sub> side

The flow distribution in the inlet area of the channels depends on the manifold substantially. According to the project proposal, flow distribution strategies for the sCO<sub>2</sub> side are investigated and evaluated. To gain an overview of possible manifold geometries a literature study is conducted accordingly in various fields of application. Based on multiple boundary conditions of the DUHS and applicability, suitable designs are selected. In the next step, numerical simulations are carried out for the initial geometry proposed by FIVES and for the selected geometries based on the literature study. Finally, the comparison of the simulation results allows a proposal of the best manifold geometry regarding uniform flow distribution in the investigated parameter range.

### 5.4.1 Literature study on different inlet plenum designs

The flow maldistribution and pressure drop within the channels of the DUHS remarkably affect the overall performance of the heat sink heat exchanger. Since microchannel heat exchangers are used in a wide range of applications, the optimization of the heat transfer has been investigated by many authors recently. However, in many cases, the channel geometry is investigated rather than the inlet manifold [31–36]. In the following, some possibilities to enhance flow distribution and thereby increase the heat transfer efficiency are presented and evaluated concerning the application to the DUHS.

Ahmad et al. [37] investigated the flow distribution and pressure drop of the inlet plenum of a pebble-bed modular reactor with the commercial code ANSYS CFX. In particular, two different shapes of the inlet plenum, namely rectangular and oval shapes were analyzed. The working fluid was Helium. The numerical results for both manifold shapes clearly showed that the oval plenum type leads to improved flow distribution.

Since the manifold of the DUHS core from FIVES Cryo is already semi-circular shaped, there is no need for optimisation in this aspect.

Furthermore, Kim et al. [38] carried out a numerical parametric study on the effects of the manifold shape on the flow distribution. The working fluid was water. While multiple configurations for the manifold geometries were tested, the flow uniformity increases with decreasing manifold width or with increasing manifold length.

Sang-Moon et al. [39] analyzed a manifold in a PCHE carrying out a parametric study with the commercial CFD code ANSYS CFX. The working fluid was sCO<sub>2</sub>. Three geometric parameters were changed as part of the parametric study, the angle of the manifold wall, the radius of the manifold wall and the width of the inlet pipes. While the angle of the inlet plenum wall varied between 25° and 75°, the best results regarding the flow uniformity were reached at an angle of 30°. The radius of the manifold wall ranged from 40 mm to 120 mm, whereas higher radii caused improved flow uniformity but also a higher pressure drop in the inlet plenum. The width of the inlet pipes varied between 2.2 mm and 2.7 mm. The width of 2.6 mm was found to be optimal regarding flow uniformity and friction. Conclusively, it was found that the flow uniformity was most dependent on the radius of the manifold.

FIVES designed the manifolds according to piping standards and the thickness results from the pressure load in this circuit. Therefore, altering the thickness of the half-cylinder is not a suitable option in the case of the DUHS. However, the width of the manifold and thus the radius of the header could be adjusted.

Furthermore, Ke et al. [40] investigated different manifold designs for PCHE using the numerical CFD software ANSYS FLUENT. The working fluid was water. The initial geometry is given by a single rectangular manifold. As expected, the results show the flow distribution to be very inhomogeneous in the various channels of the PCHE. Thus, spreader plates were used to reduce flow separation and improve uniform flow distribution. Therefore, three cases with different spreader plate radii were analyzed. In one of these cases, each radius was four times the width between spreader plates ( $r = 4b$ ). This case caused the best results regarding the flow separation in this radius study of the spreader plates. Moreover, the number of spreader plates was investigated for a constant radius. While the uniformity of the flow distribution increased with growing spreader plates, there is also more friction, which leads to an increased pressure drop. Therefore, nine spreader plates were found to be optimal in the investigated cases.

As part of the publication by Ke et al. [40], the inlet velocity of the manifold was varied also. However, in the case of the DUHS the inlet velocity results from the mass flow rate, which is adjusted by the shaft speed control of the turbine according to the decay heat. Thereby the inlet velocity cannot be adjusted under design conditions.

Baek et al. [41] investigated four different manifold configurations of microchannel heat exchangers by varying mass flow rate weighting concerning flow maldistribution. Thereby, numerical simulations were carried out and validated with experimental results. The direction of the inlet pipes was set horizontally and vertically concerning the square manifold. For both inlet directions, four different cases of different weighted mass flow rates were investigated. The simulation results of the mass flow weighting study for both inlet directions indicate that the flow distribution is more uniform for the centre-weighted mass flow rate than for the linear weighted mass flow rate concerning the manifold.

While the comparison of the pressure drop for the different manifolds is comparatively simple, the evaluation of the flow distribution requires auxiliary variables. Thus, two parameters are defined analogously to Ke et al. [40]. The dimensionless number  $E_i$  displays the relative deviation of the mass flow rate through a channel  $i$  and enables the comparison of the flow distribution between different channels. The number is defined as a ratio of the delta between the mass flow through a channel  $m_i$  and the average value  $\bar{m}$  to the total mass flow  $m_{\text{tot}}$  (( 5-4 )).

$$E_i = \frac{m_i - \bar{m}}{m_{\text{tot}}} = \frac{m_i - \frac{\sum_{k=1}^n m_k}{n}}{\sum_{k=1}^n m_k} \quad (5-4)$$

The dimensionless number  $S$  enables the characterization of the total flow distribution at the beginning of the channels and therefore the comparison of different manifold designs. The factor  $S$  is defined in equation ( 5-5 )

and describes the ratio between the standard deviation and the mean value  $\bar{m}$ . Therefore, the factor  $S$  evaluates the dispersion of the mass flow rates in the different channels [40].

$$S = \sqrt{\frac{1}{n-1} \sum_{k=1}^n \left( \frac{m_k}{\bar{m}} - 1 \right)^2} = \frac{1}{\bar{m}} \underbrace{\sqrt{\frac{1}{n-1} \sum_{k=1}^n (m_k - \bar{m})^2}}_{\text{standard deviation of the sample}} \quad (5-5)$$

The value  $S$  is equal to the coefficient of variation (CoV) which is often used to quantify dispersions and assess values also regarding flow distribution [41; 42]. These two parameters  $E_i$  and  $S$  can be used for the comparison of different geometries.

#### 5.4.2 Results of CFD simulation

The main goal of this section is the investigation and improvement of the flow uniformity in the inlet manifold of the DUHS. As mentioned above, the flow uniformity is mainly dependent on the manifold geometry. To gain a first impression of the flow distribution in the current manifold by FIVES, a simulation of the initial geometry is carried out, followed by the numerical investigation of optimized geometries. Furthermore, the pressure drop of the manifold is not considered since its influence on the total pressure drop of the core is negligible compared to the pressure drop in the channels.

The initial manifold geometry is designed with SOLIDWORKS according to the data provided by FIVES [3], see Figure 39. The outer diameter of the half-cylinder is 223 mm and the wall thickness is 17.5 mm. The inner diameter of the inlet pipes is 38.14 mm and the wall thickness is 5.08 mm. The channels are 94.67 mm, which corresponds to approximately one-sixth of the whole height of the heat exchanger core [3]. The length of the manifold is 987 mm [3].

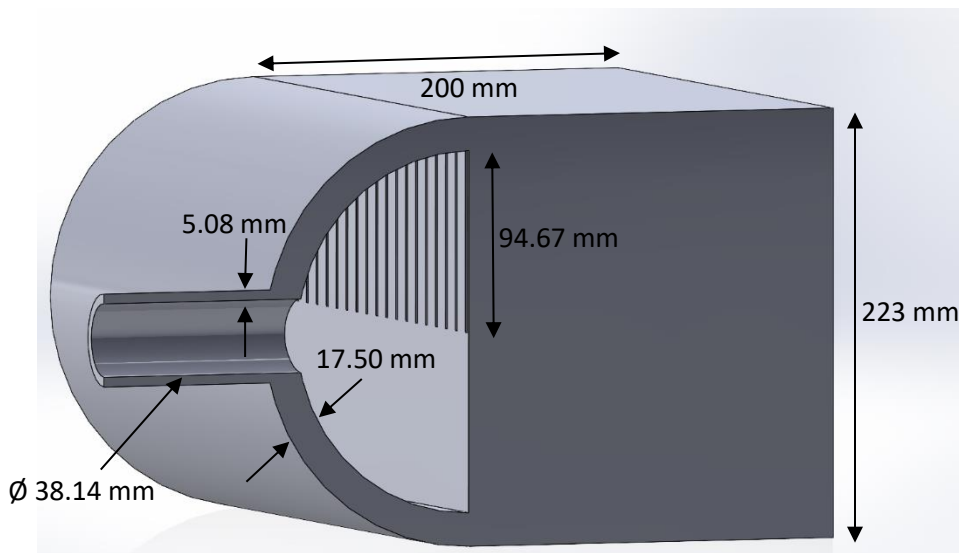


Figure 39: Initial 3D design of the manifold.

To allow the flow to fully develop in the channels, the depth of the channels is set to 200 mm. This section focuses on the optimisation of the manifold geometry from a hydrodynamic point of view and therefore no heat transfer is considered in the channels. The detailed core of the DUHS including the fin geometry is not considered in the simulations. However, the fins reduce the effective free flow area in the channels. Thus, the original channel high of 4 mm is reduced to 2.73 mm of the free-flow area according to calculations for the cross-section area of the fins (3.45 mm<sup>2</sup> per channel).

Fairzu et al. [43] investigated and compared the real gas behaviour of sCO<sub>2</sub> for two points, once near and once far away from the critical point, with isothermal numerical simulations against experimental data. According to the results of this paper, the ideal gas model approximates the behaviour of sCO<sub>2</sub> sufficiently accurate in comparison to experimental data for conditions far away from the critical point. As mentioned in section 5.1, the flow parameters of the DUHS are set to 12.7 MPa and 243.19 °C, thereby these conditions exceed the critical point of 7.38 MPa and 31.1 °C significantly. Thus, the sCO<sub>2</sub> in the isothermal manifold is modelled with the ideal gas. Furthermore, a mass flow rate of 3.875 g/s and a free flow area of 261.29 mm<sup>2</sup> results in a Mach number of approximately 0.0003 per channel. Since the Mach number is below the threshold of 0.3 for compressibility, the flow in the simulation geometry is assumed to be incompressible whereby an ideal gas behaviour can be assumed.

Chen et al. [44] examined the three turbulence models: standard k- $\epsilon$ , renormalized group k- $\epsilon$  (RNG), and realizable k- $\epsilon$  (REAL) for the flow in a manifold of industrial processing equipment. The results with the REAL turbulence model were found to fit the experimental data best among the investigated turbulence models. Because of this, the REAL turbulence model is chosen for the simulation of the manifold of the DUHS.

To finish the set-up of the simulations, Table 9 summarises the flow parameter and boundary conditions of the simulation, based on the latest results of the project and the literature review (chapters 5.1 and 5.4.1). Since the mass flow rate is based on the entire heat removal system, it must be divided by 120 for the simulation of one core.

**Table 9: Flow parameters and boundary conditions for the simulations.**

Flow Parameter and Boundary Conditions	Type	Value
Pressure	-	12.7 MPa
Temperature	-	243.19 °C
Mass flow rate per core	-	0.284 kg/s; 0.113 kg/s
Inlet	Velocity inlet	
Outlet	Pressure outlet	-
Wall	No-slip	-

Figure 40 to Figure 42 show the results of the simulation with the initial geometry of the manifold at the design point. Starting with Figure 40, the velocity profiles for different channel cross-sections with a scale of 0 to 0.15 m/s are shown. It can be seen that the different channel cross-sections have different velocity distributions. The channels near the inlet pipes have higher velocities while the velocities at the side and intermediate channels are lower. Furthermore, it can be seen in the channel cross-sections of channels 21 and 43 that inflow jets are formed, half of them flowing into the channels and half against the heat exchanger core. This leads to the formation of zones with low flow velocities. In the flow cross-sections of channels 1, 21 and 43, flow separation from the lower channel wall can be seen, which leads to an inhomogeneous velocity distribution in the channels. The selected channel length of 200 mm is not sufficiently long to achieve a hydrodynamically fully developed flow. It should be noted that this is a simplified rectangular geometry of the channels without fins, as this Chapter is focused on the investigation of the flow distribution area. In the real Model of the DUHS, the fins can have a significant influence on the velocity distribution inside the channels.

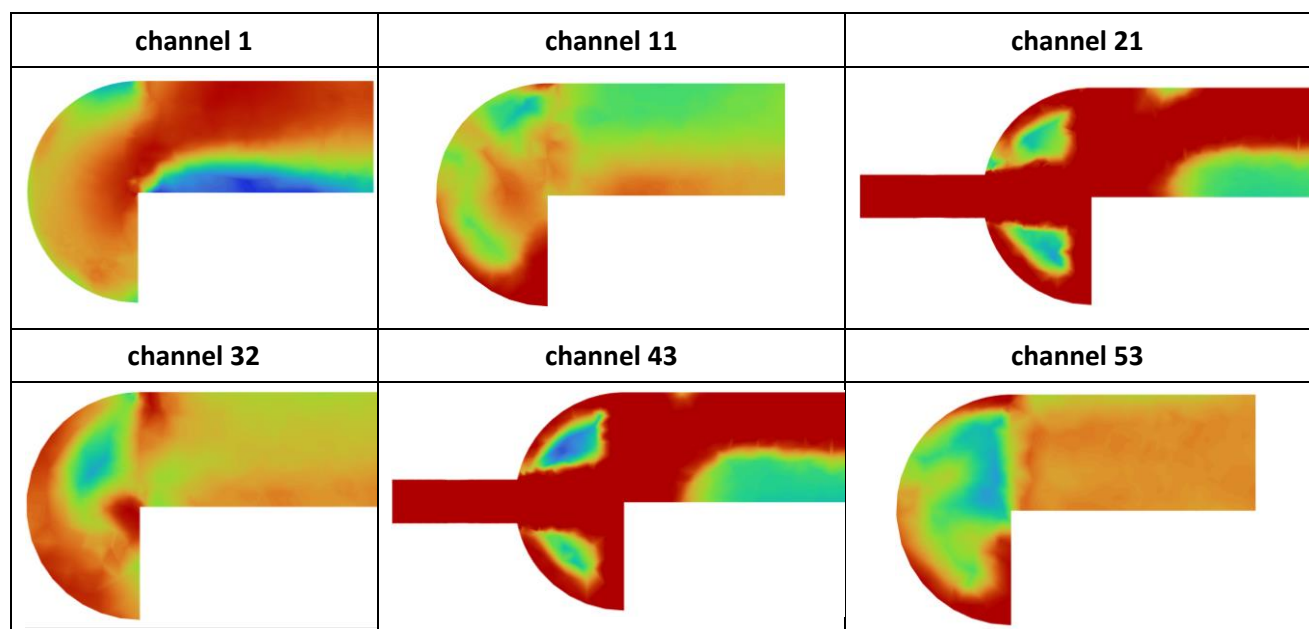
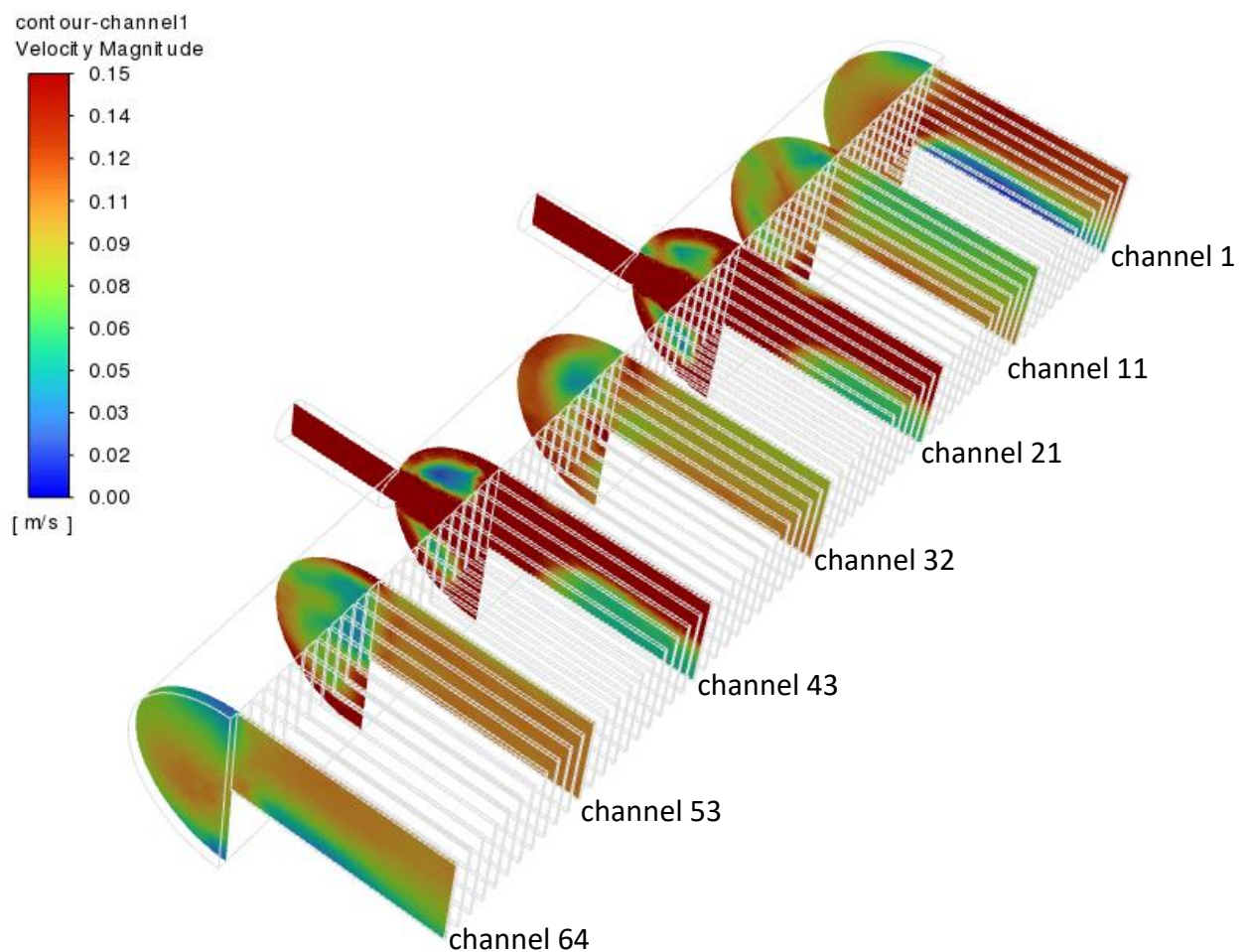


Figure 40: Simulation results of the manifold – velocity profile in the channel cross-sections for the initial geometry at the design point.

Figure 41 shows the inflow characteristics of sCO<sub>2</sub> from the inlet pipes for the channel cross-sections of the channels 43 to 45 on a scale of 0 to 0.3 m/s. As can be seen, the impact of the impinging inlet jet on the heat exchanger core results in flow recirculation along the radius of the manifold and flow-calming zones above



and below the jet. It can also be seen that there is a separation of the flow from the bottom channel wall within the channels. Again, it should be noted that this model is simplified without fins in the channels.

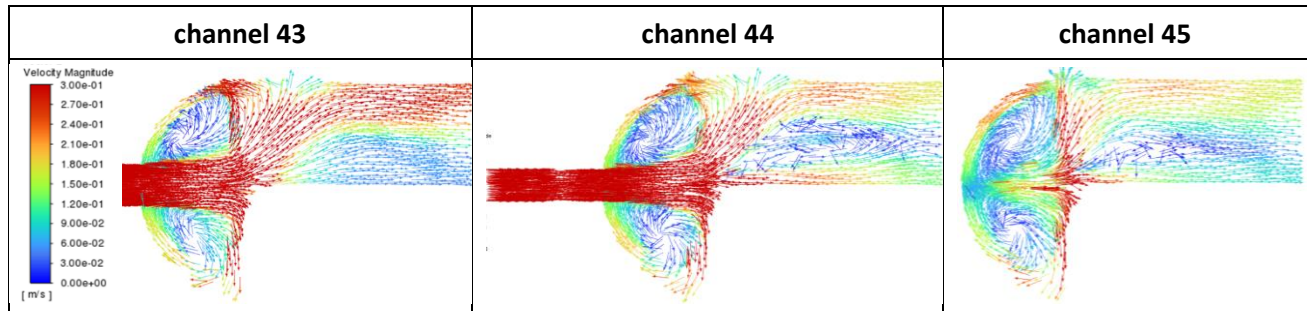


Figure 41: Simulation results of the manifold – velocity vectors for the initial geometry at the design point.

Figure 42 shows the velocity pathlines for the first simulation with the initial geometry of the manifold. The upper part of Figure 42 (A) is for a velocity scale of 0 to 0.3 m/s and the lower part of Figure 42 (B) for 0 to 1 m/s. As can be seen, the sCO<sub>2</sub> flows with a high velocity of about 0.7 m/s through the inlet pipes into the distribution area where the velocity decreases due to the increase in flow cross-section. In Figure 42 (B), it can be seen that large-scale vortex structures are formed on the sides of the manifold distribution area perpendicular to the heat exchanger channels, while the vortices near the inlet pipes are smaller and parallel to the heat exchanger channels. Figure 42 (A) also shows that the flow velocity in the heat exchanger channels close to the inlet pipes is higher.

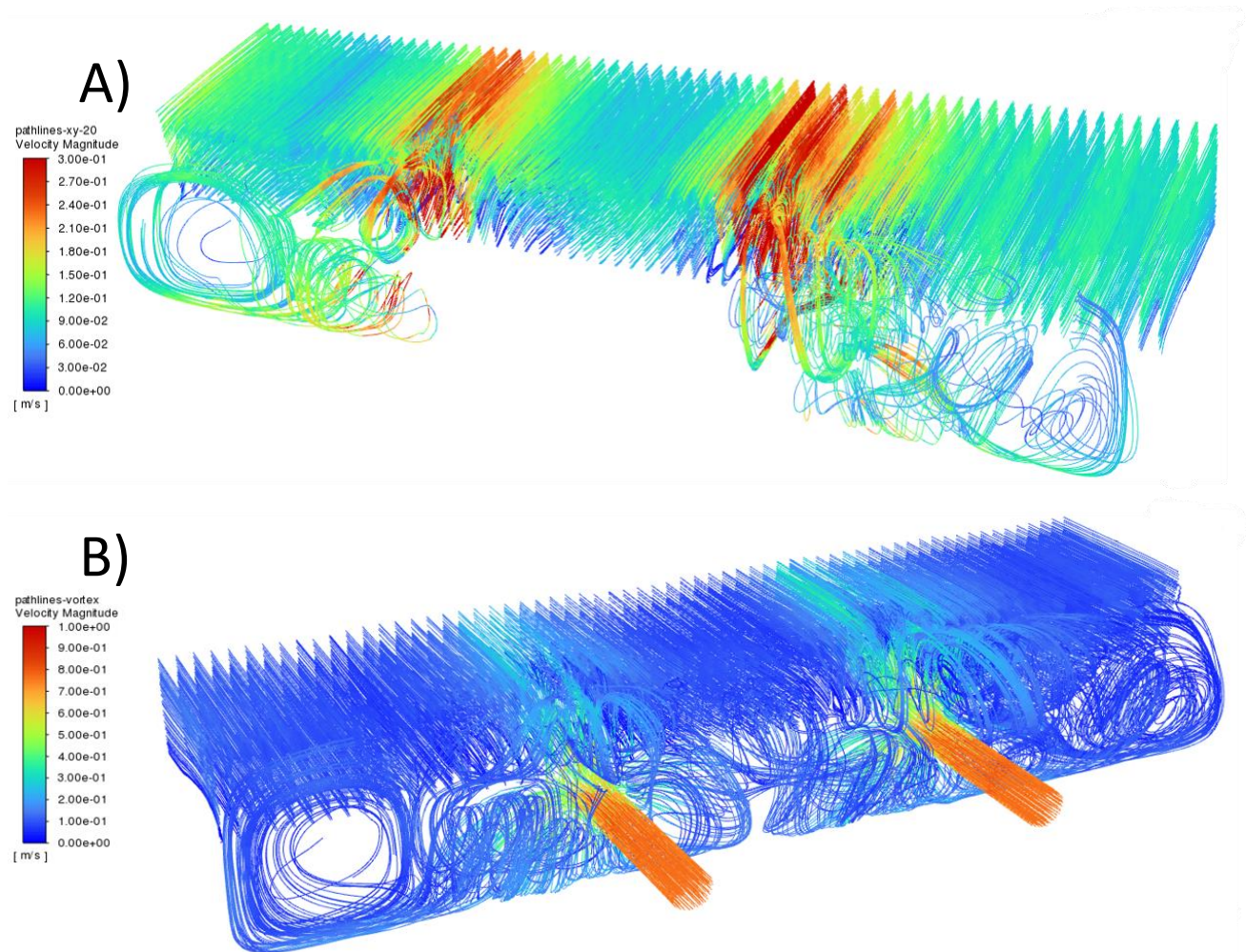
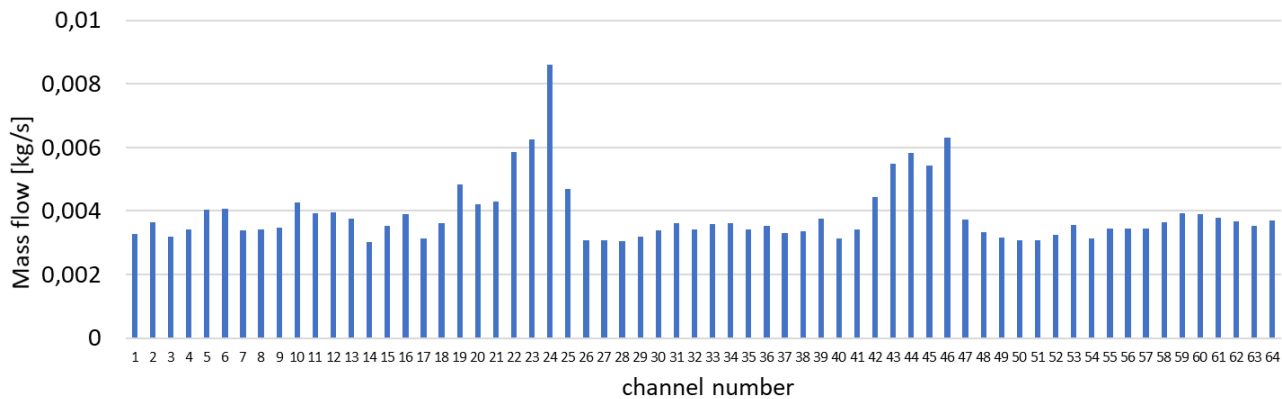


Figure 42: Simulation results of the manifold – velocity pathlines for the initial geometry at the design point.

Since the aim of the investigation was not the velocity distribution but the uniform flow distribution regarding the mass flow, the mass flow per channel was plotted in Figure 43 for the design point of the initial manifold design. As can be seen, the mass flow in the channels close to the inlet pipes is 1.5 to 2 times higher than the mass flow in the other channels.



**Figure 43: Mass flow distribution for the initial geometry at the design point.**

According to the results of the literature study in chapter 5.4.1, two variations of the manifold design are selected for further consideration. The first is an adjustment of the diameter of the distribution area, and the second is the use of additional inlet pipes. Based on this, the following two design options were considered for further simulations. For the first design option of the manifold in Figure 44, the inner diameter of the distribution area was reduced to the height of the channels, which is 94.67 mm. All other dimensions are the same as in Figure 39. In the second design option in Figure 44, the construction of the distribution area is kept constant and the number of inlet pipes is doubled. Doubling the number of inlet pipes makes sense for construction reasons, as the previous two inlet pipes can easily be extended to four inlet pipes by installing two T-junctions. The distance between the inlet pipes to the sides of the heat exchanger core and each other is 198.5 mm. The other dimensions are the same as in Figure 39.

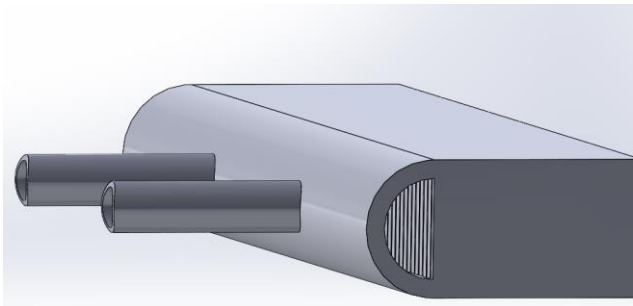


**Figure 44: Manifold design variation – smaller radius.**

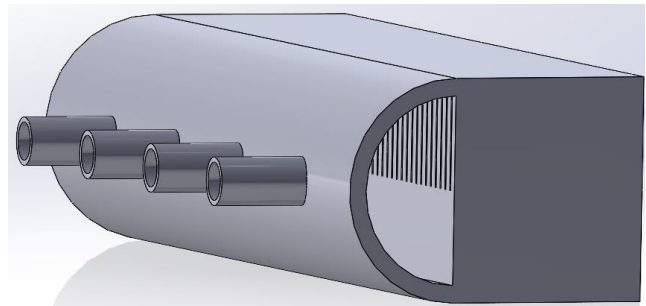


**Figure 45: Manifold design variation – four inlet pipes.**

Figure 46 shows the velocity pathlines for the simulation with the smaller radius geometry at the design point. The velocity scales are the same as in Figure 42. Compared to Figure 42 (B), the flow velocities in the flow distribution area of the manifold in Figure 46 (B) are significantly higher due to the smaller volume. Due to the geometric limitation, the vortex size is smaller and almost all vortices are parallel to the channels. The higher velocities in the flow distribution area are also present at a sufficient distance from the inlet pipes. The velocities in the upper and bottom walls of the channels near the inlet pipes in Figure 46 (A) are very high and less in the middle area. In contrast, in Figure 42 (A) the velocity of the channels near the inlet pipes is very high over the entire channel height.



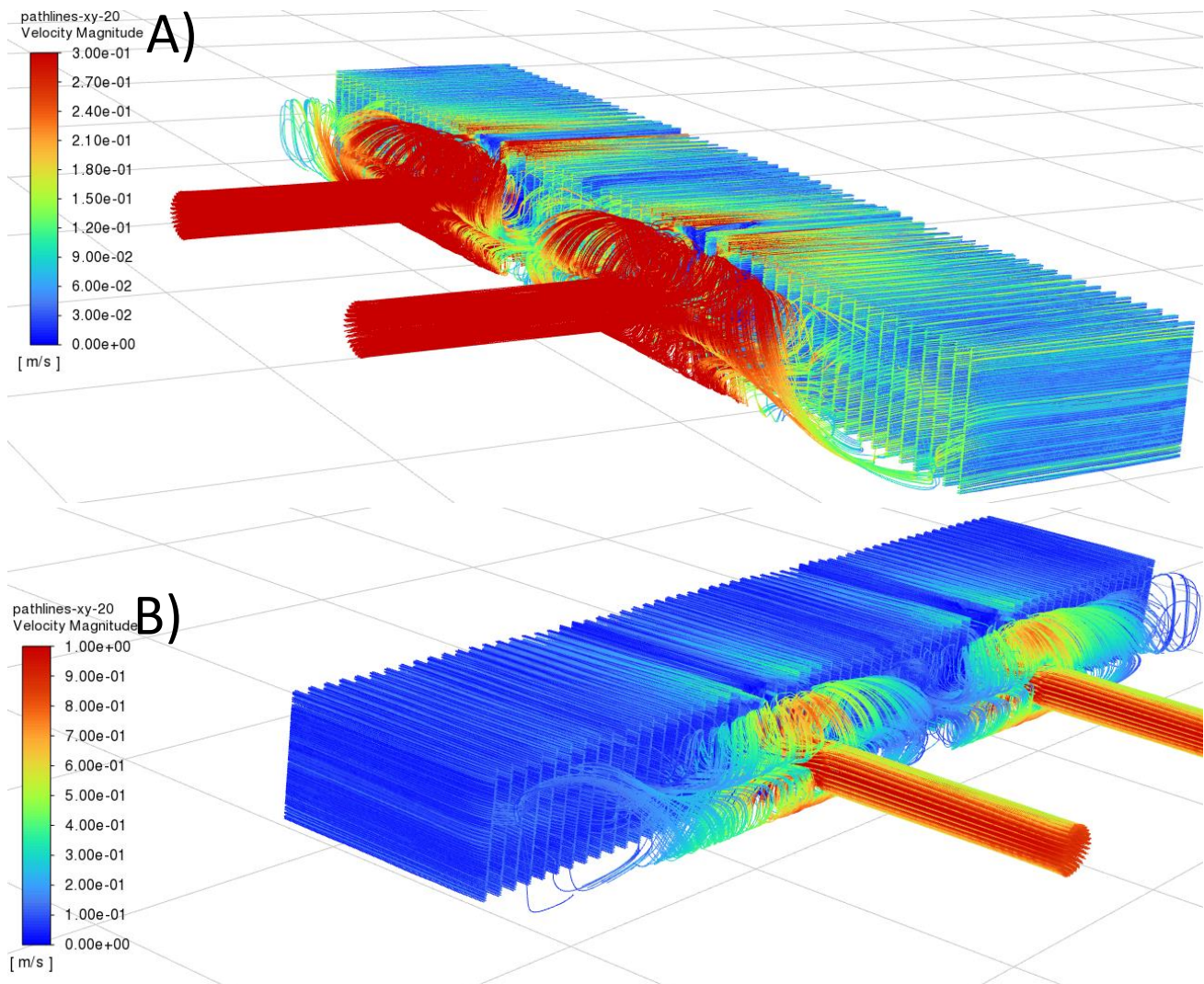


**Figure 46: Simulation results of the manifold – velocity pathlines for the smaller radius geometry at the design point.**

The results for the simulation of the four inlet pipes design at design point parameters are shown in Figure 47 on a velocity scale of 0 to 0.3 m/s. As can be seen, higher velocities are only reached at the bottom of the channels near the inlet pipes, whereas these channels have lower velocities at the top.

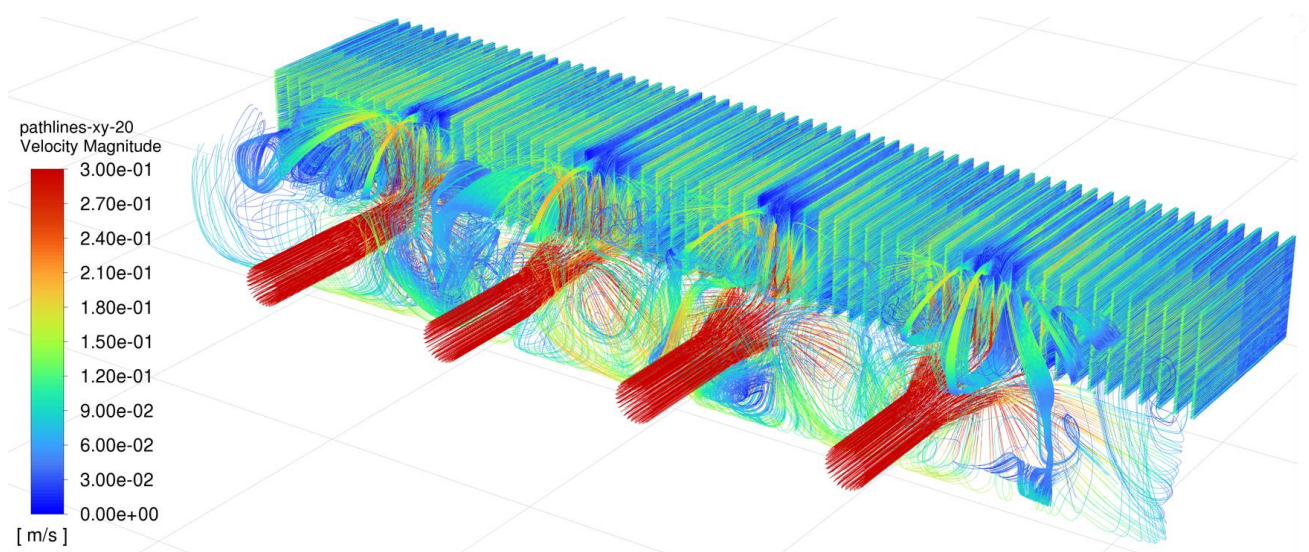


**Figure 47: Simulation results of the manifold – velocity pathlines for the four inlet pipes geometry at the design point.**

After the quantitative discussion of the simulation results at the design point conditions, the parameters  $E$  and  $S$  of the introduced equations in chapter 5.4.1 are used to evaluate the flow distribution quantitatively. Figure 48 shows the  $E$  parameters for each channel of all three geometries at design point conditions. The calculated values for  $S$  can be found in the diagram legend. As can be seen, the inlet pipes of the initial and the four inlet pipe geometries can be localised by a higher value of  $E$ . Both geometries have a similar  $S$  parameter, whereby the four inlet pipe geometry is with  $S=0.20$  somewhat lower. The smaller radius geometry shows the best results in terms of flow distribution, as can also be seen from the very low  $S$  parameter of 0.03. In this geometry, the flow velocities in the plenum are higher at design point conditions due to the smaller plenum volume. This enhances turbulence and thus improves turbulent mixing. Compared to the other two geometries, there are fewer flow-calming areas.

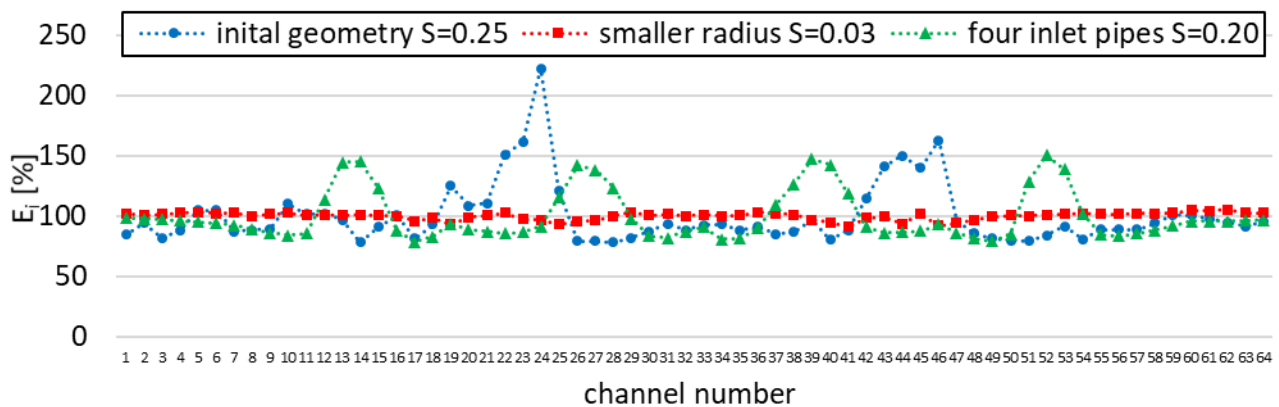


Figure 48: Relative deviation of the mass flow rate through a channel for all geometries at the design point.

In addition, the simulations of all three designs were repeated at another mass flow rate (Table 9) to consider a different operational state. The results can be seen in Figure 49. It can be seen that the  $E$  parameters for the initial geometry and the smaller radius geometry show high peaks in the area of the inlet pipes with an  $S$  parameter of 0.45 respectively 0.63. The four inlet pipe geometry also shows peaks of the  $E$  parameter, however, these are significantly lower with an  $S$  parameter of 0.15. While at the design point mass flow rate, the flow distribution is most uniform with the smaller radius geometry, this geometry shows the highest  $S$  value at the low mass flow rate at this operational state. It can be explained by the low flow velocities and thus the lower degree of mixing in the plenum. Considering the results for both mass flow rates, the four inlet pipe geometry can be seen as a good alternative to the initial geometry, because of the lower  $S$  parameter and less sensitivity to the mass flow rate.

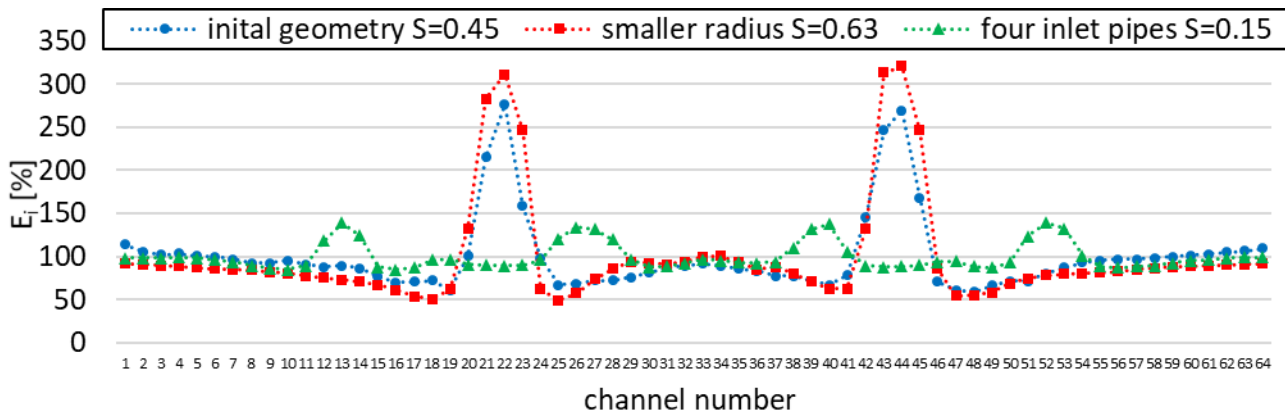


Figure 49: Relative deviation of the mass flow rate through a channel for all geometries at the transient point.

### 5.4.3 Main findings and proposition for the plenum design

At the beginning of the flow distribution investigation, a literature study was carried out to find out the geometrical parameters with the highest influence on the uniformity of the flow distribution. It was found that especially the radius and the number of inlet pipes of the manifold can have a significant potential to improve the flow distribution in the heat exchanger channels. Based on the literature study, two new geometries of manifolds were constructed. One with a reduced manifold radius and one with four inlet pipes.

To investigate the uniformity of the flow distribution, simulations of a simplified model of the manifold were carried out with ANSYS FLUENT. To determine the simulation parameters, previous results of the ATHLET simulations were analysed. It was shown that inlet temperature and inlet pressure in the DUHS is almost constant over the entire operating time, whereas the mass flow rate shows a transient characteristic. For this reason, the simulations were carried out once at design point conditions at a temperature of 243 °C, a pressure of 12.7 MPa and a mass flow rate of 0.284 kg/s and once at a transient point with a mass flow rate of 0.113 kg/s. To evaluate the uniformity of the flow, two dimensionless parameters E and S were introduced, whereby an S value of 0 stands for a 100 % uniform flow distribution.

The initial geometry at design point conditions has shown that higher mass flow rates occur in the heat exchanger channels near the inlet pipes of the manifold with an overall S value of 0.25. The most uniform flow distribution was found with the reduced diameter of the manifold with an S value of 0.03, which might be due to the higher turbulence caused by the smaller volume of the manifold. The design with four inlet pipes has an S value of 0.25 at design point conditions. With the reduced diameter, the initial geometry has an S value of 0.45 and the geometry with the reduced radius of the manifold is 0.63. Both geometries show significantly higher mass flow rates in the heat exchanger channels close to the inlet pipes of the manifold. The geometry with the four inlet pipes has an S value of 0.15 and thus the most uniform flow distribution for the reduced mass flow rate. For both mass flow rates, increasing the number of inlet pipes at the manifold from two to four leads to a more uniform flow distribution. Considering that due to the lower flow velocities in the four inlet pipe geometry probably lower pressure drop occurs and that the reduced mass flow rate is representative of a longer period of operation of the DUHS, this geometry can be proposed for the plenum design.

## 6 Final design and model of the heat sink HX

### 6.1 Improvements to the preliminary conceptual design & estimated performances

The design propositions made by USTUTT and CVR constituted the major starting point for the optimization of the DUHS design initially proposed by Fives.

The data for the Colburn and Fanning factors obtained from the small-scale experiments by USTUTT and CVR have been implemented in the "Fives fins bank" and allow new simulations with the optimised designs. However, it should be mentioned that for the development towards TRL-9, experiments with special mockups with fins have been required.

In addition, the "optimal fins" determined in the chapters above of this deliverable are not standard. For instance, if we take the fins characteristics in Table 10 case 2, even if the stamping machines available at Fives Cryo's workshop can produce straight fins out of stainless steel sheets of 0.3 mm thickness, they are not strong enough to produce serrated ones because it means that it must rip the metal sheets between each serration. For all these reasons, an interesting alternative was to make simplified simulations. These simulations are based on comparisons between:

- the first preliminary case, fitting to the required performances specifications,
- and the new cases, taking into account the optimal design propositions based on the ratios of the calculated heat exchange areas over the required heat exchange areas according to the cycle's requirements (to which we will refer to in the following as A Ratio), and the estimated pressure drops,

in order to give the opportunity of evaluating the best choice for the final design of the equipment.

This ratio was willingly set to 1.35 for the preliminary simulations to add a safety measure to the performance of the heat sink exchanger since the airflow is directly supplied by fans, without specific devices such as the classically used headers, to direct 100 % of the required flow into the air layers of the DUHS.

This optimization work aims to try not to deviate too much from this "ideal" ratio value to make sure that the thermal performances required for the cycle are reached.

### 6.2 On the Air side, simulations based on the best channels design

The geometry selected by CVR for channel design is presented below in Table 10. New design simulations were run taking these new parameters into account.

**Table 10: Fins geometrical characteristics proposed for Air side optimization**

Air side fins parameters	Height [mm]	Thickness [mm]	Fins Per Meter [FPM]	Serration [mm]
<b>Case 1: Preliminary design</b>	4	0.15	393.7	0
<b>Case 2: Proposed fins on Air side</b>	5	0.3	312.5	0

Despite the slight improvement of the pressure drops (Table 11), which is expectable due to the important pitch of the proposed fins and their increased height, we can notice that the A ratio is too low.

This means that the area provided by the new fins is quite inferior to the area required to achieve the targeted thermal performances, contrarily to the predictions of the 1D model developed by CVR.



Another fact is that the increased height is not favourable regarding the mechanical resistance to the pressure on sCO<sub>2</sub> side. The fins in the circuit with the lowest pressure should withstand the pressure effort of the adjacent circuit, the sCO<sub>2</sub> one, which is at 120 bar.

**Table 11: Results of the simulations “preliminary case” and “proposed fins on Air side case”**

For 1 unit of 20 cores	A Ratio	Pressure drops in exchange zone for Air side [mbar]	Total pressure drops in the Air side [mbar]
<b>Case 1: Preliminary design</b>	1.350	2.77	3.4
<b>Case 2: Proposed fins on Air side</b>	0.970	1.62	2.3

A mechanical study shows that for this pressure level, the height of the fins should be kept equal or inferior to 4 mm, beyond this value the risk of creep increases. The alternative would have been to increase the thickness of the parting sheets between the low and high pressures layers, but this could be conceivable for high thermal conductive materials, unfortunately, stainless steel is not, and increasing the thickness of the parting sheets would not be in favour of reducing the DUHS volume.

### 6.3 On the sCO<sub>2</sub> side, simulations based on the best channels design and flow distribution area

First, the selected fins geometry according to this optimization work is the serrated fins. These fins are well known for the increased thermal performances they provide in comparison with the straight plain fins.

We simulated a new case, taking into account the serrated fins on the sCO<sub>2</sub> side. Table 12 shows the differences between the fins characteristics in the preliminary design and the design taking into account USTUTT’s conclusions.

**Table 12: Fins geometrical characteristics proposed for the sCO<sub>2</sub> side optimization**

CO <sub>2</sub> side fins parameters	Height [mm]	Thickness [mm]	Fins Per Meter [FPM]	Serration [mm]
<b>Case 1: Preliminary design</b>	4	0.3	787.4	0
<b>Case 2: Serrated fins on CO<sub>2</sub> side</b>	4	0.3	787.4	3.175

The results of this simulation showed the A Ratio is higher for case 2 (see Table 13), which means that using the serrated fins on the sCO<sub>2</sub> side provides a slightly increased calculated heat exchange area thanks to their increased efficiency, but this increase is not that important if we make the comparison on the other hand with the generated pressure drops which is the counterpart of increasing the thermal efficiency with serrated fins. The pressure drops on the sCO<sub>2</sub> side are 7 times higher than in the preliminary design, which might be a major inconvenience for turbomachinery to compensate for almost 1 bar of pressure drop.

**Table 13: Results of the simulations “preliminary case” and “serrated fins on the sCO<sub>2</sub> side case”**

For 1 unit of 20 cores	A Ratio	Pressure drops in the exchange zone for the sCO <sub>2</sub> side [mbar]	Total pressure drops on the sCO <sub>2</sub> side [mbar]
<b>Case 1: Preliminary design</b>	1.350	112.07	134
<b>Case 2: Serrated fins on the sCO<sub>2</sub> side</b>	1.392	947.29	971.7

From a heat exchanger manufacturer's point of view, regarding these results, we consider the gain in volume of heat exchangers (roughly 3 % of the overall volume) not interesting enough in comparison with the generated pressure drop, which can compromise the efficiency of the other cycle's components.

Regarding flow distribution area, 2 options were provided by USTUTT, either reducing the size of the headers to match the size of the specific openings for inlet and outlet distribution zones, or doubling the number of nozzles.

As a first step, a closer look at the cost reduction aspects: the choice made for the preliminary design on headers diameter took into account the standard diameters of seamless stainless steel tubes that could be found in the market, matching the necessary thickness to answer the regulatory requirements in terms of mechanical resistance to pressure at high temperature. Unfortunately, the corresponding diameter is quite important in comparison to the inlets/outlets of sCO<sub>2</sub>.

Taking into account the reduction of diameter while keeping the selected thickness of the walls means that it will be necessary to order specific stainless steel tubes for this specific use from the suppliers, who may charge up to 5 times the regular price. Regarding the current economic inflation and the significant rise in materials costs, this might not be in favour of targeting an optimized cost of the DUHS solution.

For all these reasons, the second option, by doubling the number of nozzles, stands out. A new simulation taking into account this option was achieved.

**Table 14: Comparison between simulations of DUHS with 2 and 4 nozzles on the sCO<sub>2</sub> side**

For 1 unit of 20 cores	Inlet velocity in the nozzles [m/s]	Outlet velocity in the nozzles [m/s]	Pressure drops between nozzles and headers – inlet-[mbar]	Pressure drops between nozzles and headers – outlet- [mbar]	Total pressure drops between nozzles and headers [mbar]
<b>Case 1: Preliminary design (2 nozzles)</b>	5.38	1.43	19.44	3.62	23.06
<b>Case 2: 4 nozzles for CO<sub>2</sub> circuit design</b>	2.69	0.71	4.86	0.90	5.76

The new design with 4 nozzles is completely favourable in terms of fluid velocities and pressure drops. Table 14 shows a decrease in inlet and outlet velocities in the nozzles for the 4 nozzles case, and consequently in pressure drops between the nozzles and the headers. The final design is consequently modified to match this new design.

## 6.4 Drawings

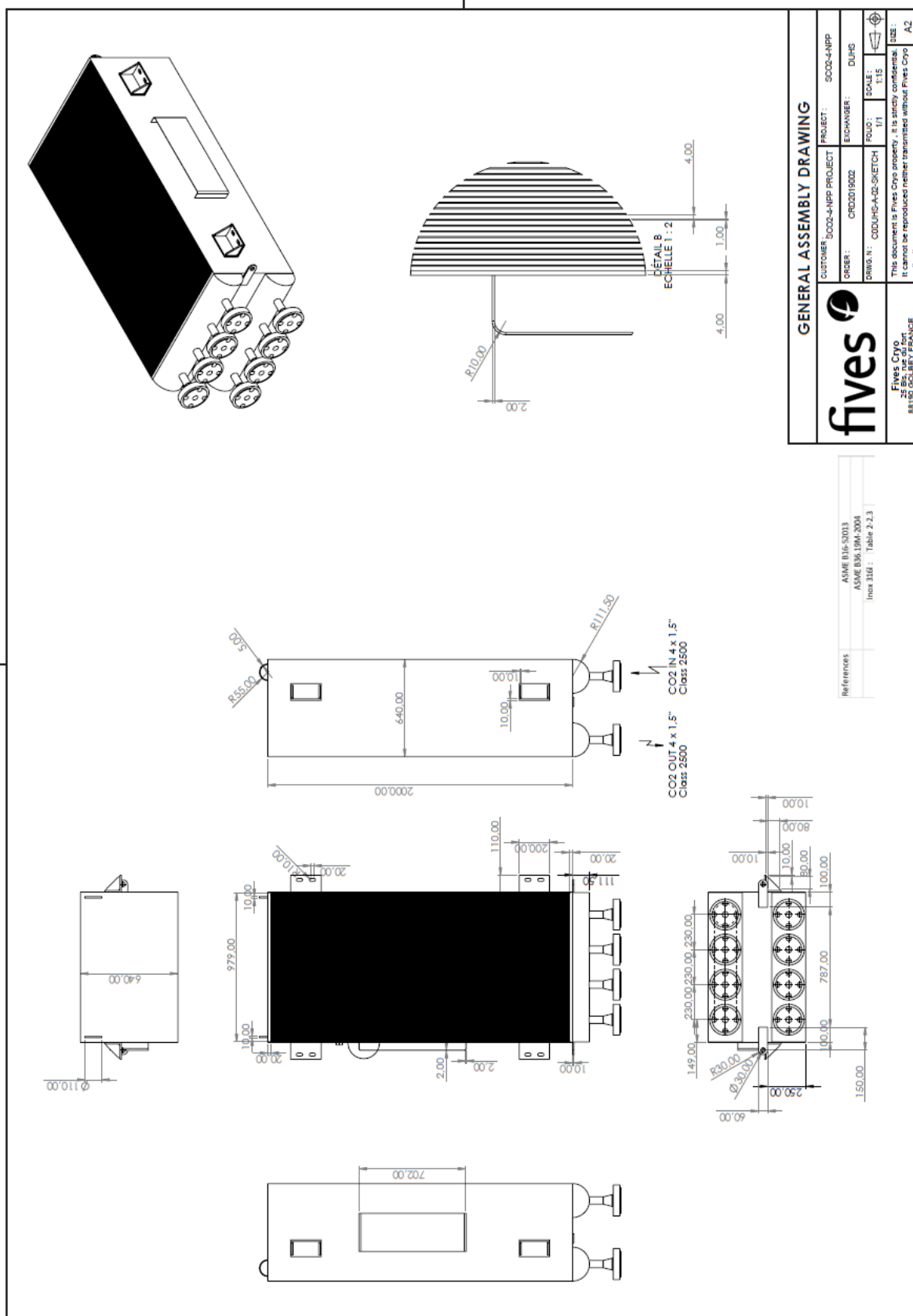
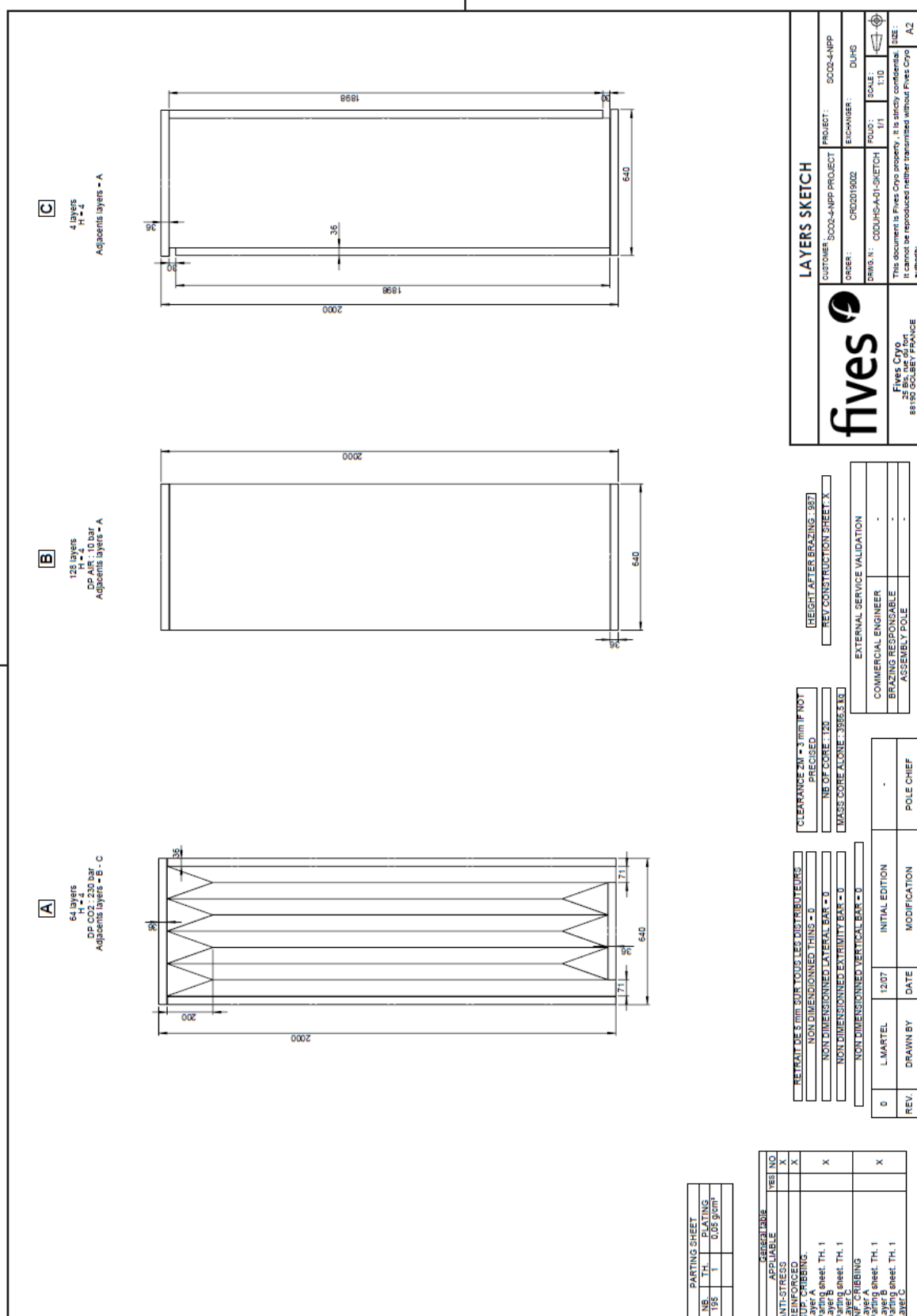


Figure 50: General assembly drawing of 1 core of the DUHS



**Figure 51: Layers sketch of 1 core of the DUHS**



## 6.5 Cost Estimation

According to the drawings in section 6.4, the DUHS component is composed of 120 cores. Each core has the following dimensions: 1200 mmx987 mmx640 mm (WxHxL), for a core volume of 0.76 m<sup>3</sup>. The total volume of the DUHS is 91.2 m<sup>3</sup>. The corresponding estimated costs are detailed in Table 15.

**Table 15: DUHS costs details**

<b>TOTAL Costs of Material</b>	€	<b>95845.1</b>
<b>Manufacturing workforce</b>		
Fins manufacturing	€	3000
Parts preparation & Stacking	h	450
	€	30600
Brazing alloy application	h	225
	€	15300
Headers welding	€	8740.8
<b>TOTAL Manufacturing Workforce</b>		<b>57640.8</b>
<b>Subcontracting</b>		
Sheets cutting	€	8500
Other parts cutting	€	4000
Brazing in vacuum furnace	€/unit	4000
<b>TOTAL Subcontracting</b>		<b>16500</b>
<b>External purchase</b>		
Compression device	€	42000
<b>TOTAL External purchase</b>	€	<b>42000</b>
TRANSPORT	€	1000
<b>Design office / QC NPP regulation</b>		
Design office	h	8
	€	464
Internal examination	€	17000
External examination	€	2500
<b>TOTAL Design office / QC</b>	€	<b>19964</b>
<b>TOTAL for a single core</b>	€	<b>190950</b>
<b>TOTAL number of cores</b>		<b>120</b>
<b>TOTAL DUHS costs</b>	<b>M€</b>	<b>42.391</b>

## 7 Conclusion

---

Based on the preliminary design of the DUHS and the simulations of the heat removal system in ATHLET, this deliverable presents the optimisation processes for the air and sCO<sub>2</sub> side of DUHS and the final design.

The DUHS thermal-hydraulic design was experimentally and numerically verified by testing a small mockup unit. The experimental data were used to determine the heat transfer and Fanning friction factor correlations. These correlations were utilized to find an optimal channel geometry with a balance between the heat transfer and the pressure drop on the air side. The optimal air side channel geometries were proposed based on the average channel flow velocities alongside their energy requirements for given boundary conditions.

On the sCO<sub>2</sub> side, both the channel geometry and the inlet manifold design were investigated. For the channel geometry, two fin geometries from the sCO<sub>2</sub>-Flex project were analysed, whereby the straight fins have a higher area goodness factor. The investigation of the manifold design showed that an increase in the number of inlet pipes from two to four leads to a more uniform flow distribution into the channels.

The final design of the DUHS was established regarding the results of the optimization work on both the sCO<sub>2</sub> and the air side. A compromise needed to be achieved to take into account not only the thermal and hydraulic optimization part but also the mechanical resistance of the device according to what is expected by the regulation, the manufacturability and the cost reduction optics. The corresponding drawings and the estimated costs are included.

## 8 References

---

- [1] SCO<sub>2</sub>-HERO. <http://www.sco2-hero.eu/>. (28.6.2020).
- [2] Hacks, A. J.; Freutel, T.; Strätz, M.; Vojacek, A.; Hecker, F.; Starflinger, J.; Brillert, D. (September 19-20, 2019). OPERATIONAL EXPERIENCES AND DESIGN OF THE SCO<sub>2</sub>-HERO LOOP [Paper presentation]. *3rd European supercritical CO<sub>2</sub> Conference*. Paris, France. (10.17185/dupublico/48871).
- [3] Tioual-Demange, S.; Voirin, V. (28.02.2021). DELIVERABLE D4.4 PRELIMINARY DESIGN AND MODELS OF THE SCO<sub>2</sub>-4-NPP [Paper presentation]. *sCO<sub>2</sub>-4-NPP*.
- [4] V.Voirin. (16.09.2021). DATASHEET-DUHS-REVC, [PROJECT DOCUMENT]. *sCO<sub>2</sub>-4-NPP*.
- [5] V.Voirin. (25.06.2021). FC-FS-DUHS MOCKUP-REVA, [PROJECT DOCUMENT]. <https://projectsworkspace.eu/sites/sCO2-4-NPP/SitePages/Project-Documents.aspx>. (*sCO<sub>2</sub>-4-NPP*).
- [6] A. Vojaček. (01.09.2017). SCO<sub>2</sub> EXPERIMENTAL LOOP AND CVR R&D ACTIVITIES [PROJECT PRESENTATION]. [http://www.sco2-hero.eu/wp-content/uploads/2017/09/03\\_Vojacek\\_CVR\\_sCO2-experimental-loop-and-CVR-RD-activities.pdf](http://www.sco2-hero.eu/wp-content/uploads/2017/09/03_Vojacek_CVR_sCO2-experimental-loop-and-CVR-RD-activities.pdf). (SCO<sub>2</sub>-HeRo.).
- [7] Fernández-Seara, J.; Uhía, F. J.; Sieres, J.; Campo, A. (2007). A GENERAL REVIEW OF THE WILSON PLOT METHOD AND ITS MODIFICATIONS TO DETERMINE CONVECTION COEFFICIENTS IN HEAT EXCHANGE DEVICES. *Applied Thermal Engineering*, 17-18, pp. 2745–2757. (10.1016/j.applthermaleng.2007.04.004).
- [8] Gnielinski, V. (2013). ON HEAT TRANSFER IN TUBES. *Journal of Heat Transfer*, 63, pp. 134–140. (10.1016/j.ijheatmasstransfer.2013.04.015).
- [9] Gnielinski, V. (2015). CORRIGENDUM TO “ON HEAT TRANSFER IN TUBES” [INTERNATIONAL JOURNAL OF HEAT AND MASS TRANSFER 63 (2013) 134–140]. *Journal of Heat Transfer*, 81, pp. 638. (10.1016/j.ijheatmasstransfer.2014.10.063).
- [10] W. M. Rohsenow, J. P. Hartnett and Y. I. Cho. (1993). HEAT EXCHANGERS. Handbook of heat transfer, pp. 1277–1308.
- [11] Kays, W. M. and London, A. L. (1984). COMPACT HEAT EXCHANGERS. McGraw-Hill, New York, NY.
- [12] Lemmon, E. W.; Huber, M. L.; McLinden, M. O. (2010). (9.0). REFPROP. Reference Fluid Thermodynamic and Transport Properties - REFPROP. NIST Standard Reference Database 23.
- [13] HEAT EXCHANGER SPECIFICATION SHEET N° SCO<sub>2</sub>-4-NPP - REVISION C. (2021).
- [14] Hofer, M.; Buck, M.; Prusek, T.; Sobiecki, N.; Vlček, P.; Kriz, D. (31.05.2021). DELIVERABLE 2.2 ANALYSIS OF THE PERFORMANCE OF THE SCO<sub>2</sub>-4-NPP SYSTEM UNDER ACCIDENT SCENARIOS BASED ON SCALED-UP COMPONENTS DATA [Paper presentation]. *sCO<sub>2</sub>-4-NPP*.
- [15] Frýbort, O.; Kříž, D.; MELICHAR, T.; VLČEK, P.; HAKL, V.; VYSKOČIL, L.; Hofer, M. (31.08.2021). DELIVERABLE 5.4 THERMODYNAMIC PERFORMANCE ON THE HEAT RECOVERY SYSTEM INTEGRATED INTO THE PLANT [Paper presentation]. *sCO<sub>2</sub>-4-NPP*.
- [16] FUNDAMENTALS OF HEAT EXCHANGER DESIGN. Hoboken, NJ, USA. *John Wiley & Sons, Inc.* (2003).
- [17] Manglik, R. M. and Bergles, A. E. (1995). HEAT TRANSFER AND PRESSURE DROP CORRELATIONS FOR THE RECTANGULAR OFFSET STRIP FIN COMPACT HEAT EXCHANGER. *Experimental Thermal and Fluid Science*, 2, pp. 171–180. (10.1016/0894-1777(94)00096-Q).
- [18] Khoshvaght-Aliabadi, M.; Khoshvaght, M.; Rahnama, P. (2016). THERMAL-HYDRAULIC CHARACTERISTICS OF PLATE-FIN HEAT EXCHANGERS WITH CORRUGATED/VORTEX-GENERATOR

- PLATE-FIN (CVGPF). *Applied Thermal Engineering*, pp. 690–701. (10.1016/j.applthermaleng.2015.12.135).
- [19] Peng, H.; Ling, X.; Li, J. (2014). PERFORMANCE INVESTIGATION OF AN INNOVATIVE OFFSET STRIP FIN ARRAYS IN COMPACT HEAT EXCHANGERS. *Energy Conversion and Management*, pp. 287–297. (10.1016/j.enconman.2014.01.050).
- [20] Chen, T.; Wang, J.; Peng, W. (2017). FLOW AND HEAT TRANSFER ANALYSES OF A PLATE-FIN HEAT EXCHANGER IN AN HTGR. *Annals of Nuclear Energy*, pp. 316–328. (10.1016/j.anucene.2017.05.008).
- [21] Ganzarolli, M. M. and Altemani, C. A. C. (2010). OPTIMUM FINS SPACING AND THICKNESS OF A FINNED HEAT EXCHANGER PLATE. *Heat Transfer Engineering*, 1, pp. 25–32. (10.1080/01457630903263291).
- [22] Li, W. and Wang, X. (2010). HEAT TRANSFER AND PRESSURE DROP CORRELATIONS FOR COMPACT HEAT EXCHANGERS WITH MULTI-REGION LOUVER FINS. *International Journal of Heat and Mass Transfer*, 15-16, pp. 2955–2962. (10.1016/j.ijheatmasstransfer.2010.04.002).
- [23] Najafi, H.; Najafi, B.; Hoseinpoori, P. (2011). ENERGY AND COST OPTIMIZATION OF A PLATE AND FIN HEAT EXCHANGER USING GENETIC ALGORITHM. *Applied Thermal Engineering*, 10, pp. 1839–1847. (10.1016/j.applthermaleng.2011.02.031).
- [24] Wahl, A. (June 2021). DELIVERABLE 4.8: REPORT OF PSEUDO CRITICAL TEST DATA.
- [25] Liao, S. M. and Zhao, T. S. (2002). AN EXPERIMENTAL INVESTIGATION OF CONVECTION HEAT TRANSFER TO SUPERCRITICAL CARBON DIOXIDE IN MINIATURE TUBES. *International Journal of Heat and Mass Transfer*, 25, pp. 5025–5034. (10.1016/S0017-9310(02)00206-5).
- [26] Dang, C. and Hihara, E. (2004). IN-TUBE COOLING HEAT TRANSFER OF SUPERCRITICAL CARBON DIOXIDE. PART 1. EXPERIMENTAL MEASUREMENT. *International Journal of Refrigeration*, 7, pp. 736–747. (10.1016/j.ijrefrig.2004.04.018).
- [27] Wahl, A.; Mertz, R.; Laurien, E.; Starflinger, J. (September 19-20, 2019). EXPERIMENTAL INVESTIGATION OF HEAT TRANSFER AND PRESSURE DROP IN TUBES TO COOL CO<sub>2</sub> NEAR THE CRITICAL POINT [Paper presentation]. *3rd European Conference on Supercritical CO<sub>2</sub> (sCO<sub>2</sub>) Power System*. Paris, France. (10.17185/DUEPUBLICO/48882).
- [28] Wahl, A.; Mertz, R.; Laurien, E.; Starflinger, J. (2021). HEAT TRANSFER CORRELATION FOR SCO<sub>2</sub> COOLING IN A 2 MM TUBE. *The Journal of Supercritical Fluids*, 173, pp. 105221. (10.1016/j.supflu.2021.105221).
- [29] Wahl, A.; Mertz, R.; Laurien, E.; Starflinger, J. (March 23-24, 2021). EVALUATION OF DETERIORATION IN VERTICAL SCO<sub>2</sub> COOLING HEAT TRANSFER IN 3 MM TUBE [Paper presentation]. *The 4th European sCO<sub>2</sub> Conference for Energy Systems*. Online Conference.
- [30] Wahl, A.; Mertz, R.; Laurien, E.; Starflinger, J. (2022). HEAT TRANSFER DETERIORATION IN VERTICAL SCO<sub>2</sub> COOLING IN 3 MM TUBE. *Energy*, pp. 124240. (10.1016/j.energy.2022.124240).
- [31] Hasan, M. I.; Rageb, A. A.; Yaghoubi, M.; Homayoni, H. (2009). INFLUENCE OF CHANNEL GEOMETRY ON THE PERFORMANCE OF A COUNTER FLOW MICROCHANNEL HEAT EXCHANGER. *International Journal of Thermal Sciences*, 8, pp. 1607–1618. (10.1016/j.ijthermalsci.2009.01.004).
- [32] Baik, S.; Kim, S. G.; Lee, J.; Lee, J. I. (2017). STUDY ON CO<sub>2</sub> – WATER PRINTED CIRCUIT HEAT EXCHANGER PERFORMANCE OPERATING UNDER VARIOUS CO<sub>2</sub> PHASES FOR S-CO<sub>2</sub> POWER CYCLE APPLICATION. *Applied Thermal Engineering*, pp. 1536–1546. (10.1016/j.applthermaleng.2016.11.132).
- [33] Jeon, S.; Baik, Y.-J.; Byon, C.; Kim, W. (2016). THERMAL PERFORMANCE OF HETEROGENEOUS PCHE FOR SUPERCRITICAL CO<sub>2</sub> ENERGY CYCLE. *International Journal of Heat and Mass Transfer*, 102, pp. 867–876. (10.1016/j.ijheatmasstransfer.2016.06.091).

- [34] Kim, T. H.; Kwon, J. G.; Yoon, S. H.; Park, H. S.; Kim, M. H.; Cha, J. E. (2015). NUMERICAL ANALYSIS OF AIR-FOIL SHAPED FIN PERFORMANCE IN PRINTED CIRCUIT HEAT EXCHANGER IN A SUPERCRITICAL CARBON DIOXIDE POWER CYCLE. *Nuclear Engineering and Design*, pp. 110–118. (10.1016/j.nucengdes.2015.03.013).
- [35] García-Hernando, N.; Acosta-Iborra, A.; Ruiz-Rivas, U.; Izquierdo, M. (2009). EXPERIMENTAL INVESTIGATION OF FLUID FLOW AND HEAT TRANSFER IN A SINGLE-PHASE LIQUID FLOW MICRO-HEAT EXCHANGER. *International Journal of Heat and Mass Transfer*, 23-24, pp. 5433–5446. (10.1016/j.ijheatmasstransfer.2009.06.034).
- [36] Commenge, J. M.; Falk, L.; Corriou, J. P.; Matlosz, M. (2002). OPTIMAL DESIGN FOR FLOW UNIFORMITY IN MICROCHANNEL REACTORS. *AIChE Journal*, 2, pp. 345–358. (10.1002/aic.690480218).
- [37] Ahmad, I.; Kim, K.-Y.; Lee, W.-J.; Park, G.-C. (2007). NUMERICAL STUDY ON FLOW FIELD IN INLET PLENUM OF A PEBBLE-BED MODULAR REACTOR. *Nuclear Engineering and Design*, 6, pp. 565–574. (10.1016/j.nucengdes.2006.07.010).
- [38] Kim, D.; Yu, C.-H.; Yoon, S. H.; Choi, J. S. (2011). EFFECTS OF MANIFOLD GEOMETRIES ON FLOW DISTRIBUTION TO PARALLEL MICROCHANNELS. *Journal of Mechanical Science and Technology*, 12, pp. 3069–3074. (10.1007/s12206-011-1220-3).
- [39] Lee, S.-M.; Koo, G.-W.; Kim, K.-Y. (2013). PARAMETRIC STUDY ON HYDRAULIC PERFORMANCE OF AN INLET PLENUM IN A PRINTED-CIRCUIT HEAT EXCHANGER. *Science China Technological Sciences*, 9, pp. 2137–2142. (10.1007/s11431-013-5294-2).
- [40] Ke, H.; Lin, Y.; Ke, Z.; Xiao, Q.; Wei, Z.; Chen, K.; Xu, H. (2020). ANALYSIS EXPLORING THE UNIFORMITY OF FLOW DISTRIBUTION IN MULTI-CHANNELS FOR THE APPLICATION OF PRINTED CIRCUIT HEAT EXCHANGERS. *Symmetry*, 12 (2), pp. 314. (10.3390/sym12020314).
- [41] Baek, S.; Lee, C.; Jeong, S. (2014). EFFECT OF FLOW MALDISTRIBUTION AND AXIAL CONDUCTION ON COMPACT MICROCHANNEL HEAT EXCHANGER. *Cryogenics*, 60, pp. 49–61. (10.1016/J.CRYOGENICS.2014.01.003).
- [42] Lance, B. and Carlson, M. D. ). PRINTED CIRCUIT HEAT EXCHANGER FLOW DISTRIBUTION MEASUREMENTS, *SAND2017-6667C*. (10.1115/GT2017-64560UR).
- [43] Fairuz, Z. M. and Jahn, I. (2016). THE INFLUENCE OF REAL GAS EFFECTS ON THE PERFORMANCE OF SUPERCRITICAL CO<sub>2</sub> DRY GAS SEALS. *Tribology International*, pp. 333–347. (10.1016/j.triboint.2016.05.038).
- [44] Chen, A. and Sparrow, E. M. (2009). TURBULENCE MODELING FOR FLOW IN A DISTRIBUTION MANIFOLD. *Journal of Heat Transfer*, 5-6, pp. 1573–1581. (10.1016/j.ijheatmasstransfer.2008.08.006).